NITROGEN DOPED SINGLE WALLED CARBON NANOHORNS FOR ENERGY STORAGE APPLICATIONS

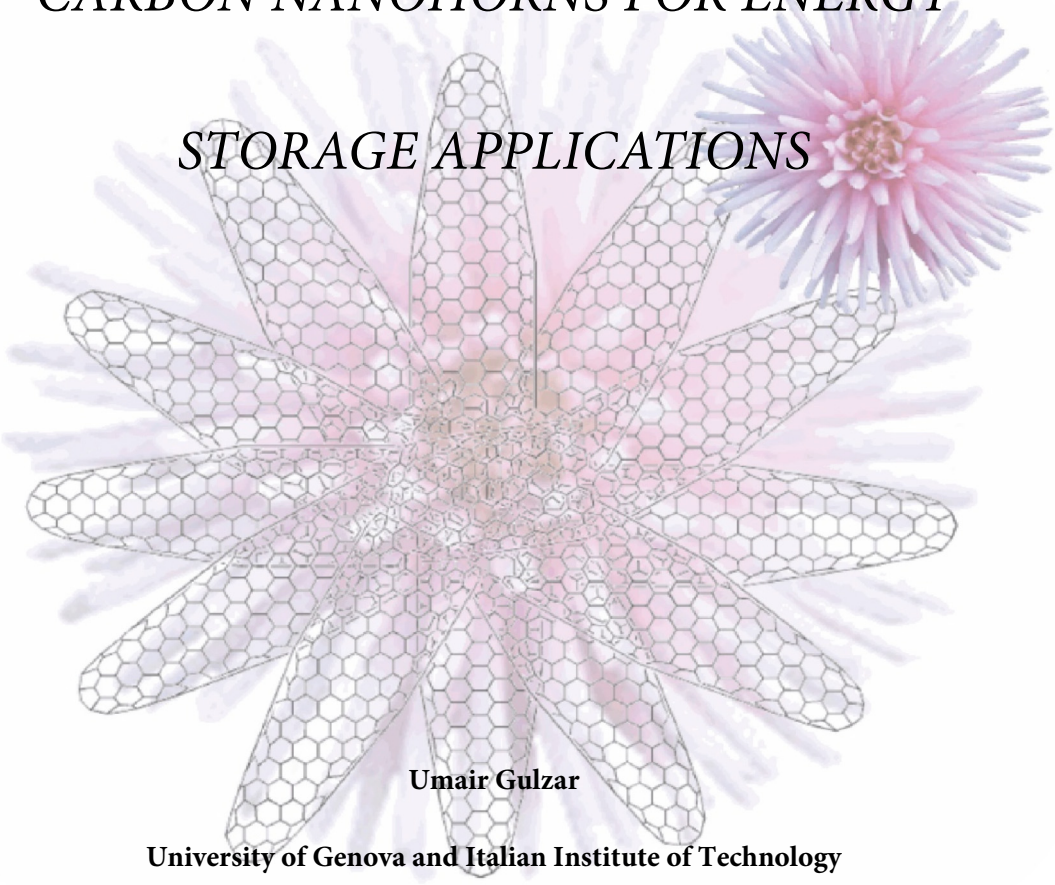

Umair Gulzar

University of Genova and Italian Institute of Technology

This dissertation is submitted for the degree of Doctor of Philosophy

January 2018

UNIVERSITÀ DI GENOVA

ISTITUTO ITALIANO DI TECNOLOGIA

DEDICATION

I would like to dedicate my doctoral thesis to my family and the child labors working in the cobalt mines of Democratic Republic of Congo

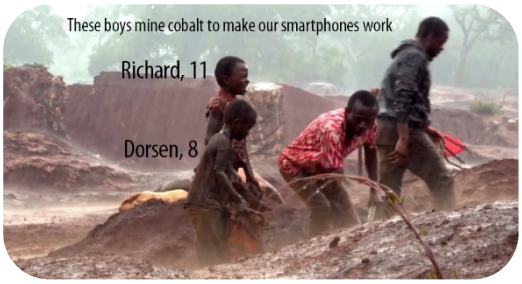

A picture taken at Katanga mines in the Democratic Republic of Congo, this barefooted 8-year-old boy was spotted standing under a heavy downpour, on the muddy soil. A man lifted a huge sack of cobalt onto his head to be transported away. He even threatened to beat the exhausted boy if he dropped the contents. The children are paid a miserable wage of 8 pence (about USD 0.10) a day, to check and sieve cobalt out of the rocks in muddy streams, using their bare hands, before loading them into sacks. Dorsen and Richard (in picture) work 12 hours a day to earn barely enough for their daily bread. Sometimes they sleep without food. More than half the world's supply of cobalt comes from the DRC. In 2012, Unicef estimated that there were 40,000 children working in all the mines across the south, many involved in mining cobalt. The human rights groups say they traced the supply chain from these mining sites to Congo Dongfang Mining (CDM), however, there are at least twenty-five international mining companies active in the D.R. Congo.

DECLARATION

This dissertation is the result of my own work and includes nothing, which is the outcome of work done in collaboration except where specifically indicated in the text. It has not been previously submitted, in part or whole, to any university of institution for any degree, diploma, or other qualification.

Signed: 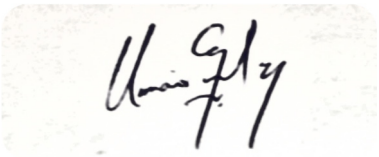

Date:20th of December 2017

Umair Gulzar

Italian Institute of Technology

ABSTRACT (ENGLISH)

Single-Walled Carbon Nanohorns (SWCNHs) are a kind of carbon material characterized by horn shaped graphitic tubules (2-5 nm diameter and 40-50 nm tube length) which, upon aggregation, form dahlia-like, bud-like and seed-like structures. Moreover, they can be mass produced (tons/year) using a novel proprietary process technology making them attractive for various industrial applications. Due to their high surface area, good conductivity and unique geometrical structure, SWCNHs have found applications in gas storage and catalysis. However, the potential of SWCNHs for energy storage, especially in lithium ion batteries, have not been explored.

Inspired by their unique porous structure, I used nitrogen doped Single walled Carbon Nanohorns (N-SWCNHs) as a conductive substrate for various cathode (Sulfur) and anode (Ge, Sn) active materials for lithium ion batteries. The choice of nitrogen doping is motivated by the quest for improved interaction between SWCNHs and the surrounding active material. In particular, N-SWCNHs were used as porous conductive host for encapsulating sulfur using a simple melt diffusion method. Electrochemical result obtained from N-SWCNHs-Sulfur composite showed high gravimetric capacities of 1650 mAh/g with high sulfur content of 80% by weight. Later, pentagon and heptagon sites of N-SWCNHs were exploited by growing 5-10 nm germanium nanocrystal around the cones of N-SWCNHs. The Ge@N-SWCNHs composite, when used as anode material, provided extremely stable and high gravimetric capacities of 1285 mAh/g at 0.1C after 100 cycles. Similar, results were obtained for Sn@N-SWCNHs composites, where a strong reducing agent (Lithium

Naphthalenide) was used to decorate Sn nanocrystal on the surface of N-SWCNHs. Capacities as higher as 735 mAh/g were achieved at 0.1C even after 140 cycles Finally, a fundamental study was performed to explore the mode of destruction in Sn electrode while sodiation/de-sodiation for sodium ion batteries Our ex-situ SEM analysis confirmed the formation of pores during sodiation while cracks started to appear during the process of de-sodiation.

Abstract (Italiano)

Single-Walled Carbon Nanohorns (SWCNHs) sono un tipo di materiale a base carbonio caratterizzati da una forma tubulare conica (diametro tra i 2-5 nm e lunghezza 40-50 nm) che in seguito ad una mutua aggregazione assumono forme note come dahlia, bud e seed, ciascuna con specifiche caratteristiche geometriche. SWCNHs possono essere prodotti attraverso metodologie a livello industriale (diverse tonnellate/anno) che li rende quindi molto appetibili anche per applicazioni su scala industriale. Grazie alla loro elevata area superficiale, buona conduttività e peculiare struttura geometrica, SWCNHs hanno trovato applicazione in diversi settori quali immagazzinamento di gas e catalisi. Altre applicazioni, come quelle riguardanti l'immagazzinamento di energia, vedi batterie agli ioni di litio, non sono ancora state esplorate. Partendo dalla specifica struttura porosa dei SWCNHs, ho utilizzato una combinazione di azoto e SWCNHs (N-SWCNHs) come materiale conduttivo per vari tipi di catodi (base zolfo) e anodi (Ge, Sn) per batterie agli ioni di litio. La scelta di un drogaggio con azoto è stata dettata dalla necessità di massimizzare l'interazione tra i SWCNHs ed il materiale attivo circostante. Infatti, N-SWCNHs sono stati usati come materiale incapsulante, ovvero atto a caturare materiale attivo al proprio interno attraverso un semplice metdo di "fusione". I risultati elettrochimici ottenuti analizzando le strutture formate da N-SWCNHs-zolfo hanno mostrato una capacità gravimetrica di 1650 mAh/g con un contenuto di zolfo fino all'80% in peso. Come passo successivo, struttre pentagonali ed ettagonali di N-SWCNHs sono state utilizzate per la crescita di nano cristalli di germanio di dimensioni 5-10 nm. Il composto Ge@N-

SWCNHs così ottenuto, quando utilizzato come anodo per batterie agli ioni di litio, ha dimostrato di essere estremamente stabile quando ciclato con una capacità gravimetrica di 1285 mAh/g a 0.1C dopo 100 cicli. risultati simili sono stati ottenuti con materiali diversi dal Ge, come Sn@N-SWCNHs. In questo caso la capacità raggiunta è stata di 735 mAh/g a 0.1C dopo 140 cicli. Infine, una analisi meccanicistica è stata affrontata con lo scopo di capire cosa accada agli anodi di Sn quando utilizzati per batterie agli ioni di sodio, ovvero cosa induca il oro danneggiamento durante la ciclazione.

ABSTRACT (IN URDU)

سنگل وال کاربن نانو ہارن، کاربن کی وہ قسم ہے جس میں ہارن نما گرافیٹک ٹیوبیں (قطر: 3-2 نانو میٹر اور لمبای: 50-40 نانو میٹر) مل کر پھول نما، شگوفہ نما یا بیج نما ڈھانچے تشکیل دیتی ہیں۔ اس کاربنی مواد کو بڑے پیمانے پر ایک ملکیتی ٹیکنالوجی سے پیدا کیا جا سکتا ہے۔ زیادہ سرفیس ایریا اور بہتر برقی خصوصیات کی بنیاد پر ان کا استعمال گیس اسٹوریج اور کیٹالیسس جیسے شعبوں میں کیا جاتا ہے۔

اسی بناہ پر ہم نے نائٹروجن ڈوپڈ سنگل وال کاربن نانو ہارن کے مختلف کمپوزٹ تیار کیے ہیں، جن کو لیتھیم آین بیٹری میں بطور کیتھوڈ (سلفر) اور اینوڈ (جرمینیم، ٹن) استعمال کیا گیا ہے۔ بطور کیتھوڈ، نائٹروجن ڈوپڈ سنگل وال کاربن نانو ہارن اور سلفر کے کمپوزٹ کو ایک آسان طریقے سے تیار کیا گیا، جس کی کیپیسیٹی 1650 میلی ایمپیر گھنٹا فی گرام حاصل ہوئ۔ اس کے علاوہ، جرمینیم کمپوزٹ (10-5 نانو میٹر) اور ٹن کمپوزٹ (30-10 نانو میٹر) کو نہایت آسان طریقوں سے تیار کیا گیا جنھوں نے اعلی کارکردگی کا مظاہرہ کرتے ہوے 1400 میلی ایمپیر گھنٹا فی گرام اور 795 میلی ایمپیر گھنٹا فی گرام کی کیپیسٹی فراھم کی۔ آخر میں، سوڈیم آین بیٹری کا رخ کرتے ہوے ٹن الیکٹروڈ کی تباہی کے پیچھے کارفرماں عوامل پر تحقیق کی گی ہے۔ ہمارے نتائج کے مطابق ٹن کی تباہی دوران ڈی۔سوڈیشن واقع ہوئ۔

ACKNOWLEDGEMENTS

First of All, I would like to acknowledge my supervisors Dr. Remo Proietti Zaccaria and Dr. Claudio Capiglia for their invaluable guidance, suggestions and most affectionate encouragement. Their mentoring motivated me to excel in the field of battery science and develop my carrier as a researcher. Besides, I pay tribute to all my teachers who taught me several courses and inculcated in me the seeds of grace, honor and dignity. I would also like to thanks Prof. Liberato Manna for allowing me to use his lab facilities with outmost freedom.

I am also very thankful to all my colleagues including Mr. Guilherme Almeida, Mr. Anatolii Polovitsyn, Mr. Quinten Akkerman, Mr. Tao Li, Miss, Xue Bai, Dr. Subrahmanyam Goriparti and Dr. Ahmed Abdelhady. I am very thankful to all the technical and non-technical staff members of the institute, who helped me in many ways for the completion of my research study.

Finally, profound gratitude to my beloved and devoted parents, and my sisters, Miss Sumera Gulzar and Mrs. Waseem Abbas for their love, care and prayers for my success in every stage of my life.

CONTENTS

1 BATTERIES: RECHARGING OUR FUTURE.....3

1.1 INTRODUCTION..... 3

1.2 BATTERIES: PAST, PRESENT AND FUTURE..... 5

1.3 FUNDAMENTALS OF ELECTROCHEMICAL CELLS..... 11

1.3.1 Thermodynamics and Kinetics11

1.4 ELECTROCHEMICAL CHARACTERIZATION TECHNIQUES..... 15

1.4.1 Cyclic Voltammetry 15

1.4.2 Chronopotentiometry 16

1.4.3 Impedance Spectroscopy 17

1.5 LITHIUM ION BATTERIES 22

1.6 SINGLE WALL CARBON NANOHORNS: SYNTHESIS, PROPERTIES AND APPLICATIONS..... 25

1.6.1 Carbon Nanohorns Synthesis 27

1.6.2 Properties and applications 28

1.7 CONCLUSION..... 31

1.8 REFERENCES..... 32

2 ACHIEVING HIGHER CAPACITIES USING NITROGEN DOPED SWCNHS BASED COMPOSITES FOR LITHIUM SULFUR BATTERIES.....37

2.1 INTRODUCTION..... 38

2.2 EXPERIMENTAL..... 40

2.2.1 Preparation of N-SWCNHs-sulfur composites 40

2.2.2 Material characterizations 41

2.3 ELECTROCHEMICAL CHARACTERIZATION 42

2.4 RESULT AND DISCUSSION 43

2.4.1 Material Synthesis and Characterization 43

2.4.2 Electrochemical characterization 50

2.4.3 Impedance Spectroscopy 52

2.5 CONCLUSIONS 56

2.6 REFERENCES 58

3 PREFERENTIAL GROWTH OF GERMANIUM NANOCRYSTALS ON THE TIPS OF NITROGEN DOPED SINGLE WALL CARBON NANOHORNS AND THEIR ELECTROCHEMICAL PERFORMANCE AS ANODE MATERIAL FOR LITHIUM ION BATTERY 63

3.1 INTRODUCTION 64

3.2 EXPERIMENTAL 67

3.2.1 Synthesis of Ge@N-SWCNHs composites 67

3.2.2 Material Characterization 68

3.2.3 Electrochemical Characterization 69

3.3 RESULT AND DISCUSSION 70

3.3.1 Synthesis and Characterization of Ge@N-SWCNHs 70

3.3.2 Electrochemical Performance of Ge@N-SWCNHs 74

3.4 CONCLUSION 81

3.5 REFERENCES 83

4 FACILE SYNTHESIS OF NITROGEN DOPED SINGLE WALL CARBON NANOHORNS BASED TIN COMPOSITE AS ANODE MATERIAL FOR LITHIUM ION BATTERY 88

4.1 INTRODUCTION 89

4.2 EXPERIMENTAL 91

4.2.1 Synthesis of Sn@N-SWCNHs composites 91

4.2.2 Material Characterization 91

4.2.3 Electrochemical Characterization 92

4.3 RESULT AND DISCUSSION 92

4.3.1 Synthesis and Characterization of Ge@N-SWCNHs 92

4.3.2 Electrochemical Performance of Sn@N-SWCNHs 95

4.4 CONCLUSION 100

4.5 REFERENCES 101

5 INSIGHT ON SODIATION/DE-SODIATION MODE OF DAMAGE OF SN FILMS. AN ELECTROCHEMICAL AND MORPHOLOGICAL STUDY 104

5.1 INTRODUCTION 105

5.2 EXPERIMENTAL 107

5.2.1 Materials Preparation 107

5.2.2 Electrochemical Cycling 107

5.2.3 Characterization 108

5.3 RESULT AND DISCUSSION 109

5.3.1 Electrode fabrication and characterization 109

5.3.2 Electrochemical Characterization 110

5.4 MORPHOLOGICAL CHARACTERIZATION 112
5.5 ELECTROCHEMICAL IMPEDANCE SPECTROSCOPY 117
5.6 CONCLUSIONS 120
5.7 REFERENCES 122
6 PROSPECTS OF N-DOPED SINGLE WALLED CARBON NANOHORNS AS ENERGY STORAGE MATERIAL 125

LIST OF TABLES

Table 1-1: Different Primary and secondary batteries with cell components, voltage and theoretical specific energy 10

Table 1-2: Different procedures of synthesizing SWCNHs 29

Table 2-1: Pore-structure parameters of N-SWCNHs. Here a_t, a_{ext}, and V_t stand for total surface area, area excluding the contributions from micro-pores and total volume, respectively. 49

Table 3.1: Comparison of the performance metrics between Ge @N-SWCNHs and other carbon based Ge composites 80

LIST OF FIGURES

Figure 1.1: (pumped hydro systems (PHS), compressed-air energy system (CAES), flywheel energy system (FES), electrical (capacitors and superconducting magnetic coil energy system (SMES), chemical (electrolyser, fuel cells), electrochemical (batteries) and thermal energy systems. 5

Figure 1.2: Discharged profile of an arbitrary electrochemical cell showing all contribution of polarization losses.14

Figure 1.3: Most common equivalent circuits and their respective Nyquist plot used to model the electrode processes of a cell. C and R are capacitance and resistance respectively while CPE and W are constant phase element and Warburg element. 19

Figure 1.4: Charge discharge process of lithium ion battery 24

Figure 1.5: HRTEM images of (a) carbon nanohorns "dahlia" aggregate (scale bar 10 nm), and (b) an individual carbon nanohorns (scale bar 2 nm). (Reprinted from reference[54] with permission from ACS). (c) Schematic showing locations of typical pentagons (blue) and heptagons (pink). (d) Cartoon of nanohorns aggregates. (f) TEM image of dahlia-type, bud-type and seed-type aggregates 26

Figure 2.1: Schematic illustration describing the sulfur encapsulation of N-SWCNHs. The red and orange dots represent the N and S doping, respectively. 43

Figure 2.2: a) TEM images of N-SWCNHs with dahlia- and bud-like aggregates. Scale bar 50 nm. b) TEM image of N-SWCNHs-S composites. Scale bar 100 nm. c) SEM image of N-SWCNHs-S composite electrode. Inset: EDS mapping of sulfur distribution (green represents sulfur, black is carbon). 44

Figure 2.3: a) Raman spectra of N-SWCNHs and sulfur composite. b) XRD patterns of N-SWCNHs, N-SWCNHs-S and pure sulfur taken as reference. 45

Figure 2.4: a) XPS spectra of N-SWCNHs; b) N-SWCNHs-S composite mixed with carbon black and PVDF; c) and d) High resolution spectra of C1s and N1s peaks; e) High resolution spectrum of S2p peak in the range of 162-174 eV. 47

Figure 2.5: a) N_2 adsorption/desorption isotherms of N-SWCNHs and N-SWCNHs-S measured at standard temperature and pressure (STP). Inset: Pore width of N-SWCNHs, where V is the volume adsorbed in cc and w is the pore width in nm. The data are normalized vs. the weight. (b) TGA analysis of N-SWCNHs-S composites. 50

Figure 3.1: Schematics of the synthetic protocol of Ge@N-SWCNHs composite 71

Figure 3.2 HRTEM images of Ge@N-SWCNHs showing two kinds of particles including cubic germanium and hexagonal GeO_2. 72

Figure 3.3. XPS analysis of N-SWCNHs with a magnified regions of N1s and C1s 73

Figure 3.4 Cyclic voltammograms of a) N-SWCNHs with 10% VC, b) Ge NCs without additives, c)Ge@N-SWCNHs without additives, d) Ge@N-SWCNHs with 10% FEC, e) Ge@N-SWCNHs with 10% VC and e) Discharge profiles of Ge NCs and Ge@N-SWCNHs with different additives. ‡ represents SEI peaks related to additives (VC or FEC),† represents SEI peaks related to electrolyte decomposition, # represent peaks related to adsorption/intercalation of lithium inside N-SWCNHs while ¥ represents the region of various peaks related to lithium intercalation inside Germanium. 76

Figure 3.5. a) Comparison for the 5^{th} cycle charge discharge curves of Ge NC and Ge@N-SWCNHs . b) Charge discharge profiles of the 5^{th} and 100^{th} cycles for Ge@N-SWCNHs composite. Cycling performance of c) Ge NCs and d) Ge@N-SWCNHs composite with and without VC at 0.1C. Rate performance of e) Ge NCs and f) Ge@N-SWCNHs 79

Figure 4.1: Schematics of the synthetic protocol of Ge@N-SWCNHs composite 94

Figure 4.2: a) Cycling voltammogram of Sn@N-SWCNHs using 10% FEC as an electrolyte additive. b) Differential capacity plot of Sn@N-SWCNHs showing decrease in activation potential after multiple cycling. Comparison of 2^{nd} and 10^{th} discharge profile of c) Sn NCs without FEC d) Sn NCs with FEC and e) Sn@N-SWCNHs with FEC. 96

Figure 4.3. Cycling performance of Sn NCs a) without FEC b) with FEC c) Sn@N-SWCNHs composite with FEC. d) Rate performance of Sn@N-SWCNHs using 10% FEC. e) Long term cycling of Sn@N-SWCNHs composite at different lithiation voltages. 99

Figure 5.1: SEM images of the surface morphology of a) copper substrate b) Sn film on the surface of substrate and (c) the cross section of the as-prepared Sn thin film by PVD

method on Cu foil substrate. The thickness of Sn film is around 1 um, as shown in (c). (d) XRD pattern of the Sn thin film electrode before cycling. 109

Figure 5.2: a) Differential Capacity plot obtained from galvanostatic charge discharge profile showing distinct peaks of various phases formed during sodiation and de-sodiation. b) Galvanostatic charge discharge profile of as-prepared Sn film (mass loading: 0.9 mg/cm^2) cycled at 20 μA. Red dots show the electrochemical potentials at which SEM images were taken 111

Figure 5.3: a) differential capacity plot of Sn electrode in the range of 0.9-0.50V showing an additional peak at 0.41V. b) Charge-discharge profile of Sn electrodes showing obvious potential dips before the start of each bi-phasic reactions. c) First and second cycles of charge discharge profile. 112

Figure 5.4: Scanning electron microscopy images of Sn thin film a) before cycling b) after full sodiation at 0.005V. c and d) are the magnified images of (b) showing the porous structure of Sn film with nanoparticles on the surface. 114

Figure 5.5: Scanning electron microscopy images of Sn thin film a) before cycling b) after full sodiation at 0.005V. c and d) are the magnified images of (b) showing the porous structure of Sn film with nanoparticles on the surface. 116

Figure 5.6: SEM images of Sn electrode after two cycles of sodiation/de-sodiation showing no difference in the particles size. 117

Figure 5.7: Impedance spectra (Nyquist plots) obtained a different stage of sodiation a) at OCV b) fully sodiated at 0.005V and de-sodiation c) at 0.16V d) 0.28 and 2.0V. 118

Figure 6.1: Disaggregation of SWCNHs after the process of lithiation exposing more surface area for electrolyte decomposition 127

BATTERIES: RECHARGING OUR FUTURE

1 BATTERIES: RECHARGING OUR FUTURE

1.1 Introduction

Hundred years ago, the world of convenience and comfort was non-existent. Aircrafts, electronic gadgets and all other vitally important amenities were not even imagined as probable engineering accomplishments. Storage of energy was hardly an important concern since primary sources of electrical energy were scarce. The lead-acid cell, one of the important invention of 19^{th} century, might have lain dormant for even longer time, if Charles Kettering would not have invented electric starter. This old energy storage system is still the most inexpensive way of starting an internal combustion engine. However, with the changing lifestyles of an increasing number of inhabitants, our energy demand will be doubled from 14 TW (2010) to 28 TW (2050) which is equivalent to 10^{10} tons of oil per year[1]. Fulfilling this demand of energy without increasing CO_2 emission require advance and sustainable renewable energy technologies based on wind, solar, tidal, biomass and geothermal resources. Unfortunately, all these resources are inherently intermittent and dispersed relative to traditional large scale facilities currently satisfying the need of electrical energy. Therefore, effective utilization of these energy resources require large and small scale electrical energy storage systems (EES). These energy storage systems (EES) are classified into mechanical, electrical, thermal, chemical and electrochemical energy storage systems according to the form of the energy they use[2]. **(Figure 1-1)**

These technologies can be further categorized according to their functions where pumped hydro systems (PHS), compressed air energy system (CAES), thermal energy system (TES), flow batteries and fuel cells fall into the category of energy management, while capacitors/supercapacitors, superconducting magnetic coil energy system (SMES), flywheels and batteries are in the category of power quality and reliability[3]. Up to 2005, more than 200 pumped hydro systems were in use all over the world providing a total of more than 100GW of generation capacity[4].

However, effective utilization of intermittent energy sources (i.e. flywheels and solar) require alternative and mobile energy storage systems. In this regard, electrochemical storage systems (i.e. batteries) are among the most viable technology which, not only provides an energy storage system for intermittent energy sources, but increasingly used as a storage bank for mobile applications.

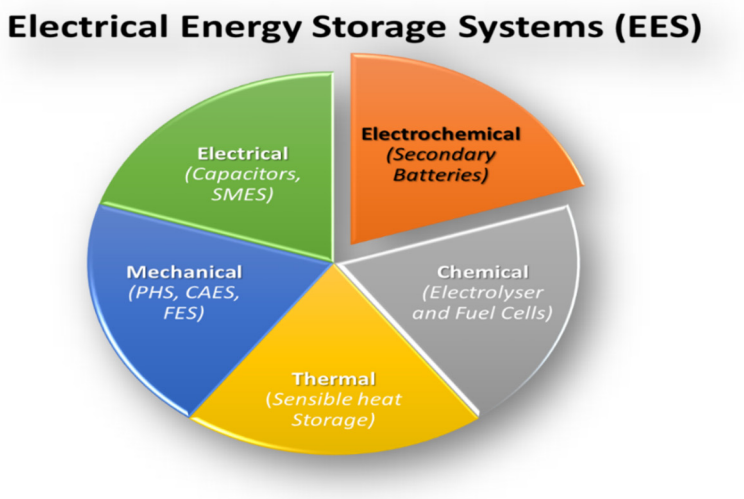

Figure 1.1: (pumped hydro systems (PHS), compressed-air energy system (CAES), flywheel energy system (FES), electrical (capacitors and superconducting magnetic coil energy system (SMES), chemical (electrolyser, fuel cells), electrochemical (batteries) and thermal energy systems.

1.2 Batteries: Past, Present and Future

The word “battery” originated from an old French word “batter” which means “to strike repeatedly”. The meaning shifted in the middle ages from “bombardment/strike” to a “unit of artillery”[5]. However, it was not until 1748 when Benjamin Franklin coined the term "battery" to describe an electrical device made of multiple Leyden jars (early electrical capacitors) as an analogy to a “battery of cannons”[6]. Today, the term “battery” is a combination of two or more electrochemical cells connected in series or parallel depending on its final application. However, in scientific community, a single electrochemical cell is also considered as a battery. Each individual component of a battery, an electrochemical

cell, is composed of two electrodes, the anode (Lower energy negative electrode), cathode (higher energy positive electrode), an electrically insulated separator and an electrolyte solution.

Based on these components, first practical battery (voltaic pile) made by Volta in 1800 had alternating discs of zinc (anode) and copper (cathode) separated by card boards soaked in brine solution (electrolyte)[7]. The cell has a higher internal resistance due to the formation of hydrogen gas at copper cathode. The technology evolved into a Daniel cell (1836) where brine solution was substituted by a different electrolyte containing $CuSO_4$ and $ZnSO_4$. The electrolyte suppressed the evolution of hydrogen and decreased the cell resistance[8]. This 1.1V cell provided a longer and more reliable current than a Voltaic cell. Later in 1866, Georges Leclanche replaced copper with a mixture of carbon and manganese dioxide (MnO_2) while using ammonium chloride (NH_4Cl) as an electrolyte salt[9]. Leclanche's "wet cell" (providing 1.4V) became the forerunner to the world's first widely used battery, the zinc carbon battery where the electrolyte was changed from aqueous NH_4Cl solution to Zinc chloride ($ZnCl_2$) paste. The same technology continued to develop until 1949 when first alkaline dry cell (providing 1.5V) with zinc anode, manganese oxide cathode and KOH based electrolyte was invented by Lewis Urry providing five to eight times longer life compare to zinc carbon cells. Most of these batteries are non-rechargeable (primary batteries), however, very recent report suggested the possibility of recharging alkaline zinc-MnO_2 battery[10].

On the other hand, rechargeable battery (secondary batteries) have evolved over the years from lead acid through nickel–cadmium and nickel–metal hydride to Li ion

batteries. Gaston Plante's lead acid cell (1859) was the first rechargeable cell consisted of a spiral roll of two lead sheets separated by a linen cloth, immersed in a glass jar of sulphuric acid solution[11]. Further improvements by Camille Alphonse Faure included lead grid lattice, into which a lead oxide paste was pressed making the design easier for mass production. The first competitor of lead acid battery came after 50 years, when Waldemar Jungner in 1899 used nickel oxide as cathode, metallic cadmium as anode and alkaline solution as its electrolyte. However, the current versions use nickel oxide hydroxide (NiOOH) as a cathode material. The Ni-Cd battery provided higher power than its lead acid counterpart but the materials used in the battery were expensive. Therefore, a cheaper version named NiMH battery was discovered in 1970 where costly and toxic metal of cadmium was replaced with hydrogen absorbing alloy of $LaNi_5$[12]. The battery provided two to three times higher capacities when compared with equivalent NiCd battery but lacked in power capabilities.

One of the revolutionary concept, derived from NiMH battery, came in 1970 when Stanley Whittingham showed that TiS_2 can be reversibility intercalated with lithium ions and made the first lithium ion battery consisted of Lithium metal as anode, TiS_2 as cathode and $LiClO_4$ as an electrolyte salt[13]. Although the battery was not viable in terms of cost and toxicity, it paved the foundation of lithium ion batteries for future developments. Within a decade, Rachid Yazami[14] and Goodenough[15] demonstrated the reversible electrochemical intercalation of lithium into graphite and lithium cobalt oxide ($LiCoO_2$) respectively. It was not until 1990 when SONY corporation commercialized the first C/$LiCoO_2$ cell **(Table 1-1).**

The attractiveness of Li-ion battery technology resides in its versatility as it covers a wide range of applications from portable electronics to electric vehicles. However, developing Li-ion batteries for society's increasing energy demands require new materials with superior performances. On the anode side, low cost Tin (Sn) and Silicon (Si) have been extensively studied as potential hosts for storing large amounts of lithium. In fact, SONY introduced its Sn-Co based Nexelion camcorder battery pack which increased the volumetric capacity by 50% over conventional batteries[16]. Researchers are constantly trying to achieve better performances using cobalt free intermetallic (Sn-Fe). Besides Sn and its alloys, silicon has received much more attention in the last five years than any other host metal for the anode. It is readily available, low cost, and reacts readily with lithium under ambient conditions. However, it needs to be nanosized to be effective and engineered in a way that allows huge volumetric expansion during lithiation. Recently, a joint venture of TESLA Motors and Panasonic introduced an improved version of lithium ion battery using traces of silicon in traditional graphite electrodes which according to Elon Musk is a "baby step" towards fully silicon based anodes. A few month ago, Samsung introduced a new kind of SiO_2/graphene balls composite increasing 29% of energy density.

On the cathode side, researchers have tried to replace/reduce the expensive cobalt based cathode with alternative cheap materials. In 1997, Goodenough disclosed another new cathode material with the formula $LiMPO_4$ (M= Fe, Mn, Ni, Co) which attracted a lot of interest due to its low cost and suitability for high power application like buses and e-bikes[17]. Later, the research group of Jeff Dahn tried different

elemental composition like $LiNi_{1/3}Mn_{1/3}Co_{1/3}O_2$ and $LiNi_{0.8}Co_{0.15}Al_{0.05}O_2$, commonly known as NMC and NCA, respectively[18,19] and improved the lithium intake up to 20% compared to $LiCoO_2$.

Beside these traditional transition metal oxide intercalation cathodes, conversion materials offer an opportunity to achieve much higher capacities. In conversion reactions, the structure is destroyed on reaction with lithium, and must be rebuilt on the recharge. Among various conversion cathode materials, room temperature lithium sulfur battery has been under development for more than a decade by Sion Power, Oxis Energy and GS-Yuasa. They have already exceeded the gravimetric energy storage capability of Li ion, but still lacking in volumetric storage capability. Besides, much effort will be required to increase the charging rate above the present specification of C/5 (5 h), and the volumetric capacity above the present 320 Wh/L. Another option towards more sustainable battery system is moving towards lithium air battery which has 10 times higher theoretical energy density compare to traditional batteries in the market today. The positive electrodes in such systems are generally composed of black carbon and manganese oxide catalysts; therefore, they are much cheaper than the cobalt-based positive electrodes currently used in Li-ion batteries[20]. However, there are severe stability issues which needs to addressed along with developing a stable electrolyte for all metal-air batteries.

Table 1-1: Different Primary and secondary batteries with cell components, voltage and theoretical specific energy

Battery	Anode/cathode/	Reaction Mechanism	Volts	Specific
Primary Cells				
Voltaic	Zn/Cu/H_2SO_4	$\mathbf{Zn_s + 2H^+ \rightarrow Zn^{2+} + H_2}$	0.7	557
Daniel	Zn/Cu/$ZnSO_4$:$CuSO_4$	$\mathbf{Zn_s + Cu^{2+} \rightarrow Zn^{2+} + Cu_s}$	1.1	458
Leclanche	Zn/MnO_2/NH_4Cl	$\mathbf{Zn_s + 2MnO_2 \rightarrow ZnO.Mn_2O_3}$	1.4	358
Alkaline	Zn/MnO_2/KOH	$\mathbf{Zn_s + 2MnO_2 \rightarrow ZnO + Mn_2O_3}$	1.4	358
Secondary Cells				
Lead	Pb/PbO_2/H_2SO_4	$\mathbf{Pb_s + PbO_2 + 2H_2SO_4 \rightarrow 2PbSO_4 + H_2O}$	2.1	252
Ni-Cd	Cd/NiO_2/KOH	$\mathbf{Cd_s + 2NiOOH + 2H_2O}$	1.35	244
Ni-Zinc	Zn/NiO_2/KOH	$\mathbf{Zn_s + 2NiOOH + 2H_2O}$	1.73	372
Ni-MH	Ni/MH/KOH	$\mathbf{MH_s + NiOOH \rightarrow M + Ni(OH)_2}$ (1.7% H_2)	1.35	240
Li-ion	C/$LiCoO_2$/$LiClO_3$	$\mathbf{Li_xC_6 + Li_{1-x}CoO_2 \rightarrow LiCoO_2 + C_6}$ (x=0.5)	4.1	410
Li-S	Li/S/LiTFSI	$\mathbf{2Li_s + S \rightarrow Li_2S}$	2.2	2500
Li-O_2	Li/air/$LiPF_6$	$\mathbf{2Li_s + O_2 \rightarrow Li_2O_2}$	2.91	3387

It has been predicted that future de-centralized storage systems will be based on flow batteries. Low-cost and sealed metal–oxygen or metal–sulfur will gain a significant market share. Intercalation-based batteries will retain a significant fraction of the

market with non-lithium-based electrochemistry, as there is not enough lithium in the world (contrary to the views of Elon Musk), to provide for transportation grid storage, and home/office storage[21].

1.3 Fundamentals of Electrochemical Cells

Electrochemical cell is a device which converts the stored chemical energy into electrical energy by an electrochemical oxidation and reduction reactions. The components of an electrochemical cell consist of an anode (negative electrode where oxidation take place during discharge), cathode (positive electrode where reduction takes place during discharge) and an electrically insulated electrolyte soaked in a separator[22].

1.3.1 Thermodynamics and Kinetics

The electrochemical reactions involved in a battery system are exhaustively complex, however, they follow the same traditional thermodynamic and kinetic formulations. Therefore, the maximum electrical energy that can be delivered by the active chemicals of a cell in standard conditions depends on the change in free energy ΔG of the electrochemical couple, as shown in **Eq. 1**

$$\Delta G^0 = nFE^0 \quad (1)$$

Where ΔG is the useful energy available for the reaction, n is the number of electrons transferred per mole, F is the faraday constant (96487 coulombs) and E^0 is the electromotive force require to initiate the reaction. However, for non-equilibrium states, the Gibb's free energy described by van't Hoff (**Eq.2**) can be combined with

Eq.1 to give Nernst equation which can be used to calculate the electrochemical potential of a cell **(Eq.3)**.

$$\Delta G = \Delta G^0 + RT.\ln\frac{A_{product}}{A_{reactant}} \qquad (2)$$

$$E = E^0 - \frac{RT}{nF}\ln\frac{A_{product}}{A_{reactant}} \qquad (3)$$

Where A is the activity of the relevant species while R and T are the gas constant and absolute temperature, respectively.

Moreover, various thermodynamics quantities for the active material can be determined experimentally using equation **Eq.4**

$$\Delta G = -nFE = \Delta H - T\Delta S$$

$$= \Delta H - nFT\left(\frac{dE}{dT}\right) \qquad (4)$$

Where ΔH is the enthalpy, or the energy released by the reaction.

By measuring the cell voltage as a function of temperature, this equation is quite helpful in predicting the thermal properties of a cell. If dE/dT is positive, the cells will heat on charge while cool on discharge and vice versa[23].

The total heat released during cell discharge is the sum of the thermodynamic entropy contribution plus the irreversible contribution. The irreversible heat is produced due to the loss of energy caused by various kinetic processes involved inside an electrochemical cell. These processes include: (1) activation polarization, which arises from kinetic hindrances of the charge-transfer reaction and follows the

Tafel equation **(Eq.5)** which can be transformed to an infamous Butler-Volmer equation **(Eq.6)**

$$E_{act} = a - b \log\left(\frac{I}{I_0}\right) \qquad (5)$$

$$i = i_0 \exp^{\frac{\alpha FE_{act}}{RT}} - \exp^{\frac{(1-\alpha)FE_{act}}{RT}} \qquad (6)$$

Where i_o is the exchange current density, E_{act} is the over potential due to charge-transfer reaction, α is the transfer coefficient, which is best considered as the fraction of the change of over potential that leads to a change in the rate constant for charge-transfer reaction. The second factor is concentration polarization, which arises from limited mass transport capabilities due to the sluggish diffusion of active species to and from the electrode surface. For limited diffusion, the concentration polarization, can be expressed by **Eq.7** as

$$E_{con} = \frac{RT}{n} \ln\left(\frac{C}{C_0}\right) \qquad (7)$$

Where C is the concentration at the electrode surface while C_0 is the concertation in the bulk solution. Third factor include ohmic polarization or IR drop, which is the sum of ionic resistance of electrolyte inside separator and porous electrode, the electronic resistance of the active mass, the current collector and the contact resistances.

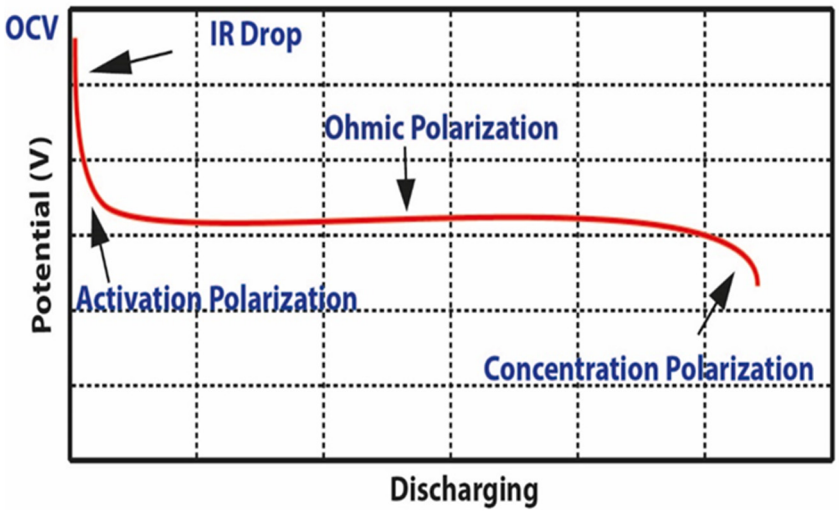

Figure 1.2: Discharged profile of an arbitrary electrochemical cell showing all contribution of polarization losses.

These resistances are proportional to the current drawn from the cell.

Therefore, the total cell voltage (V) with an external load (R), can be expressed using **Eq.8**

$$V = E^0 - E_{act} - E_{con} - E_{ohm} \qquad (8)$$

Where E^0 is the open circuit voltage, E_{act} is activation polarization or charge-transfer polarization, E_{con} is concentration polarization and E_{ohm} is the ohmic drop. **Figure 1-3** describes the contribution of over potentials in an arbitrary discharge profile of a battery.

1.4 Electrochemical Characterization Techniques

Many electrochemical techniques are available to obtain important electrochemical parameters of a battery. These parameters on one side can be used to assess and improve the performance of existing technologies while on the other hand useful to explore other chemistries for post lithium ion technologies.

1.4.1 Cyclic Voltammetry

This technique is one of the most versatile techniques to study the electrochemical reactions. Essentially, a linearly changing voltage is applied to an electrode which produces a small amount of current which is related to an electrochemical reaction at the interface of the electrode. Once a concentration gradient is created, the output current drops due to the decrease in rate of diffusive transport. Therefore, voltammograms obtained in cyclic voltammetry show multiple peaks each representing a different reaction. The peak current obtained in a cyclic voltammogram can be represented by **Eq.9**.

$$i_p = \frac{0.447\ F^{3/2} A\ n^{3/2} D^{1/2} C_0\ \vartheta^{1/2}}{R^{1/2}\ T^{1/2}} \qquad (9)$$

Where D is the diffusion coefficient, C_0 is the concertation of the reactants in bulk, ν is the scan rate, while rest has the same identity discussed before.

This technique provides both qualitative and quantitative measures of the electrode processes. For example, a revisable diffusion controlled reaction exhibits symmetrical pair of current peaks separated by ΔE which is given by **Eq.10**.

$$\Delta E = \frac{2.33\ RT}{nF} \qquad (10)$$

The separation of ΔE defines the reversibility of the reaction. For example, a reversible electrodeposition of an insoluble film (a process not governed by diffusion) give the value of ΔE close to zero. However, for quasi reversible system the value of ΔE is higher and highly dependent on sweep rate. Unfortunately, for complex systems like electrochemical cells, interpretation of voltammograms becomes complicated, nevertheless, the techniques is quite useful to calculate rate constant of various electrochemical reactions.

1.4.2 Chronopotentiometry

Chronopotentiometry also known as galvanostatic voltammetry is the most commonly used technique for acquiring various cell parameters including capacity, number of reactions, over potential and hysteresis of a cell. In this technique a constant current is applied to an electrode and its voltage response is observed during the electrochemical changes occurring at the interface of the electrode. The electrode processes may involve intercalation of lithium ions inside the crystal lattice of host material providing a steady amount of current. Once the host material is saturated with lithium ion, a sudden drop of potential is observed to acquire the next chemical reaction that can provide the same steady amount of current. Compare to voltammetry, this technique can be used conveniently to evaluate systems with high resistance (i.e. batteries) as the plots between time and voltage displays segments due to the IR component, the charging of the double layer, and the onset of the faradaic process[24].

1.4.3 Impedance Spectroscopy

Contrary to the preceding electroanalytical techniques, a more direct technique to study electrode processes is to change the electrical impedance of an electrode using electrochemical impedance spectroscopy (EIS). This technique is based on the classical method of transfer function (TF) where perturbation of a system using a sinusoidal input (E_t) results in a sinusoidal output (I_t) with different phase and amplitude[25]. Using the same principal, EIS when applied in potentiostatic mode uses a small perturbation of voltage (5-10 mV) and the response is measure in the form of electrical current. The mathematical approach to electrochemical impedance data is based on ohms law which can be written as **Eq.11**

$$Z(\omega) = \frac{E(t)}{I(t)} = \frac{E_0\,\mathrm{Sin}(\omega t)}{I_0\,\mathrm{Sin}(\omega t - \varphi)} = Z_0\frac{\mathrm{Sin}(\omega t)}{\mathrm{Sin}(\omega t - \varphi)} \qquad (11)$$

Where E_0 and I_0 is the amplitude of potential and current respectively, ω is the radial frequency in rad/s and Z_0 is the resultant impedance.

Interpretation of impedance data is tedious, therefore, these functions are represented in polar coordinates and can be described easily in complex numbers shown in **Eq.12**

$$\begin{aligned} Z(\omega) = Z_0 e^{-i\emptyset} &= Z_0(\mathrm{Cos}\emptyset + i\mathrm{Sin}\emptyset) = Z_0\mathrm{Cos}\emptyset + iZ_0\mathrm{Sin}\emptyset \\ &= Z_{Re} + iZ_{Im} \end{aligned} \qquad (12)$$

Where Z_{Re} and Z_{Im} are real and imaginary parts of the impedance, respectively while Φ is a phase angle.

One popular way of presenting electrochemical impedance data, consists of plotting the imaginary impedance component (Z_{Im}) against the real impedance component (Z_{Re}) at each excitation frequency. This representation is also known as Nyquist plot, Cole-Cole plot or a complex impedance plane plot. One of the primary advantage of this format is that it allows to obtain ohmic resistance of cell components, shown as R_1 in the Nyquist plot of **figure 1-4a**, by extrapolating the left edge of graph towards x-axis. Moreover, this plot emphasizes on circuit components which are combined in series making it convenient to interpret the data. Although the ohmic resistance and polarization (charge transfer) resistance can be easily read from Nyquist plot, the electrode capacitance can be calculated only after the frequency information is known. Therefore, an alternative way of representing impedance data is called Bode Plot where Z_w and φ are plotted against $\log\omega$. This representation allows the understanding of impedance dependence on the frequency.

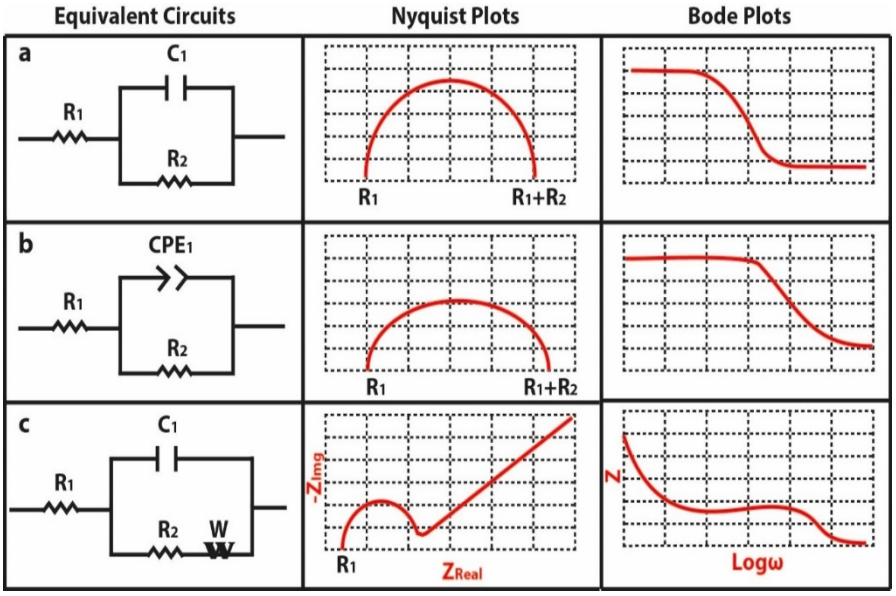

Figure 1.3: Most common equivalent circuits and their respective Nyquist plot used to model the electrode processes of a cell. C and R are capacitance and resistance respectively while CPE and W are constant phase element and Warburg element.

EIS data is commonly analyzed by simulating an equivalent circuit model consisting of individual electrical elements such as resistors (R), capacitors (C), and inductors (L). To understand the electrode processes, the elements in the model should have a physical meaning which can be associated to the processes involved in an electrochemical system. Hence, reactions occurring consequently are modelled by elements or circuits connected in series, whereas simultaneously occurring processes are modelled by elements or circuits connected in parallel. As an example, **Figure 1-4a** represents an equivalent circuit represented by the elements R_1, C_1 and R_2 where R_1 simulates ohmic resistance due to electrolyte solution and current collectors, C_1 simulates the capacity of double layer which was charged simultaneously due to a

charge transfer process. This process is associated to a charge transfer resistance (R_2) which is connected in parallel to C_1. The corresponding Nyquist plot represents a semi-circle from which ohmic and charge transfer resistances can be obtained directly from the x-intercepts.

Most of the electrode surfaces are not homogenous and contains kinks, jags, ledges and local charge inhomogeneities. Hence, the average impedance over the whole electrode surface gives a depressed semicircle in a Nyquist Plot **(Figure 1-4b)**. Modelling these electrochemical systems is far more complicated than the one predicted by the simple model containing resistance and capacitors. Therefore, it has become a popular practice to replace the double layer capacitance (C) by a constant phase element (CPE) which is given by **Eq.13**.

$$Z(\omega) = \frac{1}{Q}(j\omega)^{-n} \qquad (13)$$

Where Q is constant and n represent a factor whose values lie between 0 and 1. Putting n=1 bring the expression of pure capacitive impedance given by $Z_w = 1/\omega C$

Another commonly used circuit element in impedance data is the Warburg Impedance which accounts for the concertation over-potential in an electrode process. When transport phenomena play a significant role, the faradaic impedance can be separated into two terms including kinetic (Z_k) and diffusive impedance (Z_d). The diffusive impedance describes the contribution of concentration over-potential and depends on the transport phenomena inside the solution or solid electrode. Most intercalation materials store lithium inside the crystal lattice which builds up concentration gradient inside the active electrode material. The impedance

associated to the concentration gradient, in the absence of convection, is referred as Warburg impedance **(Eq.14.)**

$$Z(\omega) = \frac{\sigma}{\sqrt{\omega}} - j\frac{\sigma}{\sqrt{\omega}} \qquad (14)$$

Where δ is a Warburg coefficient which can be obtained from the slope of a plot between real part of the impedance (Z_R) and reciprocal square root of frequency ($1/\sqrt{\omega}$). The Warburg coefficient can be used to calculate the diffusion coefficient using Eq.15.

$$\sigma = \frac{RT}{An^2F^2C_{st}\sqrt{2D}} \qquad (15)$$

Where R, T, A, n, F have their usual meaning while C_{st} is the concentration of electrolyte inside electrode and D is the diffusion coefficient.

Figure 1-4c shows a typical Nyquist diagram consists of two distinct domains: at high frequency, a semicircle shows that the transfer resistance determines the impedance, while at low frequencies diffusion dominates and Warburg impedance is observed. However, there are certain condition that must be fulfilled before the interpretation of impedance data. These condition include linearity of the input and output signals, causality of the system (output signal are the cause of input perturbation), stability of the system and finiteness (the real and imaginary components must be finite over the entire range of frequency).

1.5 Lithium ion batteries

A battery consists of more than one cell interconnected in parallel, series or the combination of the two, depending on the application. Although, cell is an individual component of a battery, still it is wrongly popularized as battery in scientific literature. Therefore, we will define cell as an electrochemical device composed of an anode (always negative electrode), a cathode (always positive electrode), separator and an electrolyte. Lithium ion cell (LIC) is the most popular member of rechargeable cells with comparatively high energy (long discharge time) and power density (fast charging). Commercial anodes are made up of graphite while cathode materials varies from $LiCoO_2$ to $LiNiO_2$, and $LiMn_2O_4$ to $LiFePO_4$ depending on its application. However, active materials are always mixed with a small amount (3–5 wt%) of a polymer binder (polyvinylidene fluoride, PVDF) and conductive carbon (1–5 wt%) to make a homogenous slurry which is casted on metal current collector (an aluminum, Al, foil for a cathode and a copper, Cu, foil for an anode)[26]. Typical thickness, an important parameter of electrode performance, ranges from 60 to 100 μm. Usually, the electrodes are separated with a porous electrically insulated membrane with a typical thickness of 15–25 μm while electrolytes can either be a solid polymer or a non-aqueous liquid usually comprised of lithium salt dissolved in various solvents from the ester, ether or carbonate families. The difference between the electrochemical potentials of each electrode/electrolyte interface defines the theoretical voltage of a cell which generally differs from practical voltage of a cell.

The charge carriers in LIC are lithium ions which interacts with electrode active material through three different mechanisms[27,28] of which intercalation and de-

intercalation mechanism is historically, the most commercially successful mechanism involving transition metal oxide cathodes and graphite anodes. In this mechanism, while charging a full cell, made of graphite and lithium metal oxide, lithium ions migrate from negative electrode (Anode) towards positive electrode (Cathode) by oxidizing lithium metal oxide to metal oxide producing equivalent number of electrons.(**Eq 16 and 17**) Meanwhile, electrons traveling through external circuit to positive electrode reduces graphitic carbon to form LiC_6 **(Figure 1-5).**

CHARGING

$$LiMO_2 \xrightarrow{\text{Oxidation}} Li_{1-x}MO_2 + xLi^+ + xe^- \quad \text{(Anode)} \quad (16)$$

$$yC + xLi^+ + xe^- \xrightarrow{\text{Reduction}} Li_xC_y \quad \text{(Cathode)} \quad (17)$$

The process is reversed while discharging (graphite becomes cathode and lithium metal oxide becomes anode) where LiC_6 releases lithium ion which migrate through electrolyte and re-inserted in MO_2 to produce $LiMO_2$.(**Eq 18 and 19)**

DISCHARGING

$$Li_xC_y \xrightarrow{\text{Oxidation}} yC + xLi^+ + xe^- \quad \text{(Anode)} \quad (18)$$

$$Li_{1-x}MO_2 + xLi^+ + xe^- \xrightarrow{\text{Reduction}} LiMO_2 \quad \text{(Cathode)} \quad (19)$$

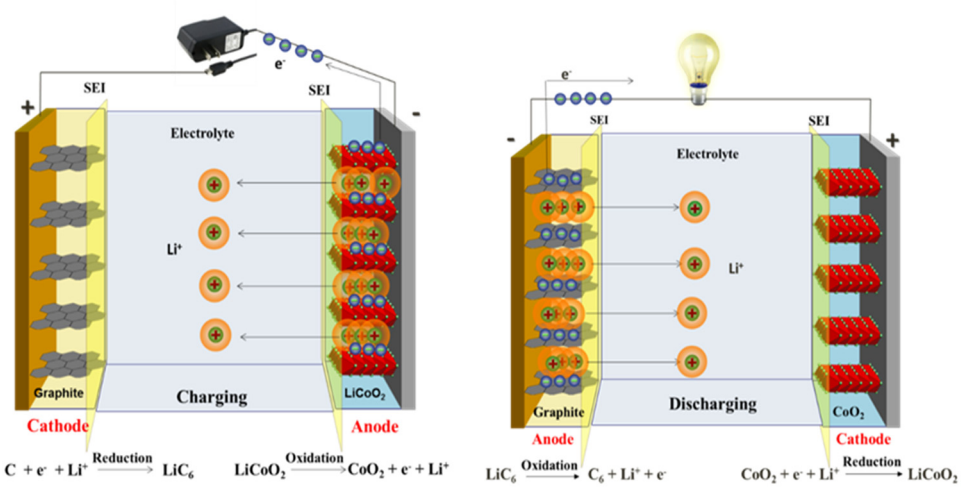

Figure 1.4: Charge discharge process of lithium ion battery

It is worth mentioning that oxidation occurs at anode which is always a negative electrode while reduction occurs at cathode which is always a positive electrode, irrespective of charge and discharge process. However, majority of galvanostatic cycling measurements, presented in the scientific literature are, in fact, conducted in half-cells where lithium metal acts as negative electrode and material to be tested is always positive. In this case, fully charged working electrode, therefore, is lithium free and comprised only of metal oxide or carbon while a fully discharged electrode is a lithium intercalated metal oxide or LiC_6. For example, $LiCoO_2$ when used as an electrode against lithium metal, it initially exist in a discharged lithiated state ($LiCoO_2$) and we need to charge it by releasing the lithium ions. On the other hand, when carbon electrode is used against the same lithium metal, it initially exists in a charged de-lithiated state which needs to be discharged by lithiation. Hence, care must be taken while assigning a certain material as anode or cathode.

1.6 Single Wall Carbon Nanohorns: Synthesis, Properties and Applications

Carbon, one of the building block of life, is poised to become the wonder element in the age of nanoscience due to its ability to assume extended two dimensional sheet structure. The in-sheet bonding of these structures is so strong that it allows them to be stable as isolated objects (graphene) as well as in curved geometries (nanotubes, fullerenes). Moreover, negative curvature geometries can also exist in the form of nanoporous carbon[30]. An intermediate state, namely carbon nanocone, also exist between sheet and fullerene structure where a single or multiple pentagonal rings defines a conical apex, which is then extended by a pure-hexagon graphenic network into a larger conical structure[31]. One major class of nanocone carbon structure is called "single wall carbon nanohorns" (SWCNHs. Besides having five pentagons at their tips, SWCNHs typically contain heptagons in their structure (**Figure 1-6a-c**) which acts as potential reactive sites with their own distinct chemistry[32]. While the tips typically have five pentagons, a sixth pentagon is required for the nanohorns walls to continue parallel to the nanohorns "axis" in the same manner as a carbon nanotube. Moreover, additional heptagon counteracts the curvature change of one pentagon, and it is common to observe spaced heptagon/pentagon pairs. The combination of pentagons and heptagons results in the elongated "short nanotube" form of nanohorns. These nanohorns typically exist as a clustered arrangement of closed conical cages typically 2–5 nm in diameter and 40–50 nm in length To date three different types of SWCNHs aggregates, 'dahlia-like', 'bud-like', and 'seed-like'

have been reported[33]. In the first type, SWCNHs protrude from the aggregate surface while, in the second and third types, the SWCNHs appear to develop inside the particle itself (**Figure 1-6d, e**). It is important to mention that dahlia-type aggregates are made of carbon nanohorns and graphene flakes bound tightly via van der Waals forces, since oxidative treatment to remove their outer layers finds no remaining material associated with the dahlia cores.

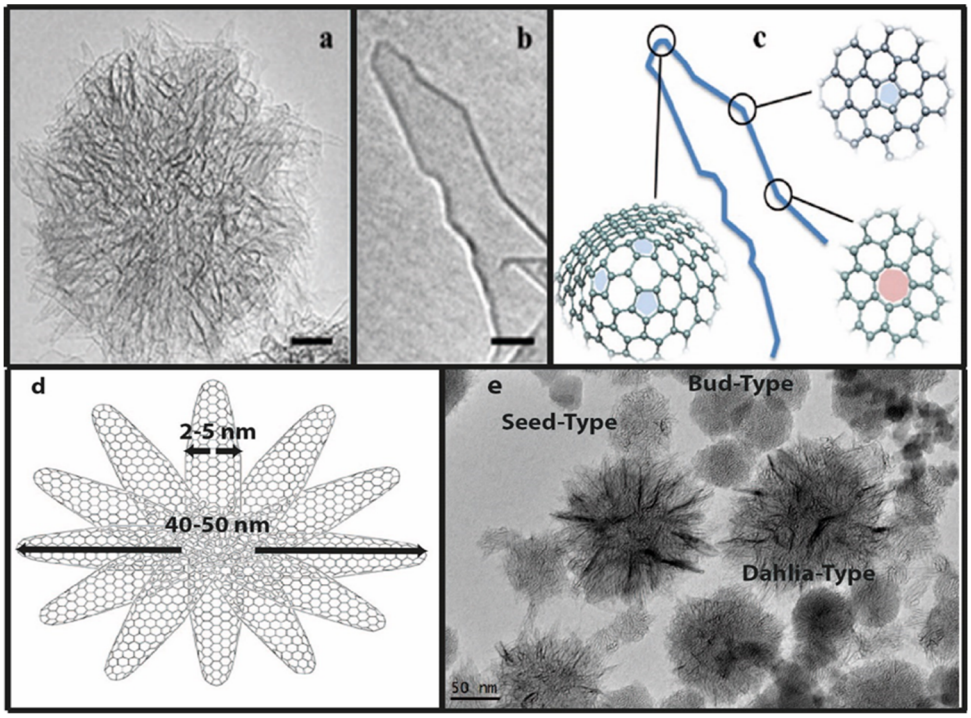

Figure 1.5: HRTEM images of (a) carbon nanohorns "dahlia" aggregate (scale bar 10 nm), and (b) an individual carbon nanohorns (scale bar 2 nm). (Reprinted from reference[54] with permission from ACS). (c) Schematic showing locations of typical pentagons (blue) and heptagons (pink). (d) Cartoon of nanohorns aggregates. (f) TEM image of dahlia-type, bud-type and seed-type aggregates

On the other hand, bud-type aggregates, where horns do not protrude from aggregate surface are produced by changing the experimental condition like carrier gas and its pressure.

1.6.1 Carbon Nanohorns Synthesis

Carbon nanohorns were first observed during arc-discharge production of fullerenes[30] where single and multiwall carbon nanohorns were produced by heating the produced soot at 2500-3500K with a positive-hearth electron gun for 4 hours. However, production of high purity dahlia-type aggregates used a pulsed arc-discharge between pure carbon rods in atmospheric pressure of air[34]. The quality of the sample can be improved by heating carbon rods to 1000°C just before ignition. Large scale production of SWCNHs uses a submerged DC arc-discharge process between graphite electrodes in liquid nitrogen producing 17 g/day of nitrogen doped SWCNHs[35]. An alternative way replaced liquid nitrogen with water while nitrogen or argon gas is injected into the arc zone through holes in the graphite electrode. The method only presented in a conference talk is capable of producing 1 Kg of SWCNHs per day[36].

Another method of synthesizing SWCNHs uses pulse laser ablation of graphite in argon atmosphere. Specifically, CO_2 laser, operated at room temperature (wavelength 10.6 μm, maximum power 5 kW, 10 ns pulse duration) produces a soot of aggregated dahlias with 85–90% purity[37]. Nanohorns obtained using this method are twice the size of those produced via arc- discharge (around 100 nm in diameter). Same experimental setup can produce Bud-type nanohorns under lighter gasses like

He and N_2[33]. A third route for the production of nanohorns, rarely mentioned in the literature, uses a high frequency eddy currents to heat graphite rods upto 3200°C producing a soot consist of dahlia and bud-like structures[38]. This deceptively simple joule heating method is able to produce around 0.1 kg of dahlias per hour, with the authors discussing the possibility of scale-up to produce tens of kilograms per hour.

Due to the cheap and scalable method of production along with minimal purification steps, four companies have step forward to commercially produce carbon nanohorn dahlias. The largest of these is NEC[39] who has facilities with production capacity of at least 1 kg per day (using ambient temperature pulsed Laser Ablation in air). Moreover, Carbonium SRL[40] announced production of 0.1 kg per hour using their Joule heating method described above., EenanoTech Ltd. with TIE GmbH[41] claimed to produce 1 kg per day of high purity dahlias via the "arc in water" arc-discharge method, described above. Finally, Advanced Technologies Partner S.r.l. with a new proprietary method claimed to produce Nitrogen Doped Single Wall Carbon Nanohorn up to ton/year. **Table 1-3** summarized the existing methods of preparing SWCNHs with varying yields.

1.6.2 Properties and applications

The unique conical structure of CNHs has a great influence on its electronic properties. Theoretical calculations have explored the stability, optimal geometry, and electronic properties of CNHs, demonstrating a net electron transfer to the pentagonal sites of the CNHs tips[42,43] and provides reactive sites for chemical functionalization.

Table 1-2: Different procedures of synthesizing SWCNHs

Method	Protocol	Quality	Amount
Pulsed Arc-Discharge	Pre-heating carbon rods to 1000C and creating arc between carbon rods in air at room temperature	Dahlias,50 nm,	Low yield
	Creating arc between graphite electrodes submerged in liquid nitrogen/Argon	Varies with Conditions	17g/day
Submerged Arc-Discharge	Creating arc between graphite electrodes surrounded by nitrogen/argon gas but submerged in water	Dahlia 95%	1Kg/day
	CO_2 laser, wavelength 10.6 μm, maximum power 5 kW, 10 ns pulse duration, Air	Dahlia, 100 nm, 85–90% purity	1Kg/day
Laser Ablation	Using Argon (20 kW/cm2 surface laser power density with 500 ms on–off pulses	Dahlia, 95% purity	1Kg/day
	Using Nitrogen (20 kW/cm2 surface laser power density with 500 ms on–off pulses	Bud, 95% Purity	1Kg/day
Joules heating	Under Helium inducing high frequency eddy currents in graphite rods	N/A	0.1 Kg/hr
Un-Disclosed	N/A	N-SWCNHs 95% Purity	Ton/Year

Another important property of CNHs is related to its porosity which makes them an attractive candidates for storing other materials. In fact, partial oxidation of CNHs allow access to internal pores by opening the tips of the cones with hole sizes smaller

than 0.9 nm[44]. CNH porosity was investigated through nitrogen adsorption and revealed the existence of micropores, with volume of 0.11 mL/g and a reasonably large surface area (308 m^2/g). However, opening of holes results in an increase of the surface area and the pore volume to 1300m^2/g and 0.9 mL/g, respectively[45–47]. To kinds of micropores have been discussed including interstitial and internal pores[46]. Another important property of SWCNHs is related to their aggregated structure (dahlia or bud) which appropriate for immobilizing metal particles on their surface. This property can be useful for anchoring alloying materials like silicon, germanium and tin to be used as anode material for lithium ion batteries.

Due to their unique structure and possibility of functionalization, SWCNHs have found plentiful applications in catalysis[48], drug delivery[49] and energy storage[50–52] and conversion[53]. Detailed applications of SWCNHs can be found in some recent reviews published elsewhere[54,55]. Interestingly, only few applications of SWCNHs have been found for energy storage, specifically for lithium ion batteries. Guan et al. has developed SnO_2/SWCNHs and Fe_2O_3/SWCNHs composites via a wet chemical method and a hydrothermal method, respectively[51,56]. SnO_2/SWCNHs composite delivered a high capacity of 530 mAh/g even after 180 cycles under a current density of 500 mA/g while Fe_2O_3/SWCNHs based electrode gave a stable capacity of 550 $mAh{\cdot}g^{-1}$ even at a high current density of 1000 $mA{\cdot}g^{-1}$ after 100 cycles. MnO_2 based composite also provided high capacities 565 mAh/g at 450 mAh/g after 60 cycles[52]. TiO_2 has also been used with SWCNHs as a composite, however, achieved gravimetric capacities were not high enough (150mAh/g at 1C) compared to other reported methods[50]. It might be due the fact that SWCNHs have been overloaded

with TiO_2 suppressing the intrinsic properties of SWCNHs. On the cathode side, Guan et al. synthesized a novel SWCNH-S composite with high S content up to 76% via a straightforward melt-infusion strategy[57]. The composite exhibited excellent electrochemical performance with a high capacity of 693 mAh/g retained after 100 cycles at a high rate of 1.6 A/g.

1.7 Conclusion

Energy storage devices, batteries in particular, are becoming one of the fundamental needs of our society. One might expect that all vehicles will be electrically powered by 2025. Therefore, developing new materials for energy storage is the most important research interest for scientific community. These materials shouldn't only provide higher energy and power densities but can be produced cost effectively on an industrial scale. In this regard, SWCNHs is a promising candidate to replace the existing technology as active storage material or supporting conducting agent for high storage active materials. It also provides an option to be tuned according to a certain application. However, extensive research is required to understand its intrinsic properties along with it lithium storage mechanism.

1.8 References

[1] Nathan S. Lewis, MRS Bull. **2007**, 32.

[2] IEC, Int. Electrotech. Comm. **2011**, 1.

[3] H. Chen, T. N. Cong, W. Yang, C. Tan, Y. Li, Y. Ding, Prog. Nat. Sci. **2009**, 19, 291.

[4] S. Linden, in Proceeding 1st Annu. Conf. Energy Storage Counc. Houston, Texas, March 3, 2003, Huston, Texas, **2003**.

[5] K. Ernest, **1971**, 154.

[6] B. Franklinn, Lett. to Peter Collinson **1749**, 3, 352.

[7] A. Volta, Philos. Trans. R. Soc. London **1800**, 90, 403.

[8] J. F. Daniell, Philos. Trans. R. Soc. London **1836**, 126, 107.

[9] G. Leclanché, French Patents, **1866**, 69,980 and 71,865.

[10] G. G. Yadav, J. W. Gallaway, D. E. Turney, M. Nyce, J. Huang, X. Wei, S. Banerjee, Nat. Commun. **2017**, 8, 14424.

[11] R. G. Planté, C. R. Hebd. Seances Acad. Sci. **1859**, 49, 402.

[12] K. Beccu, Negative Electrode of Titanium-Nickel Alloy Hydride Phases, **1974**.

[13] M. S. WHITTINGHAM, Science (80-.). **1976**, 192, 1126.

[14] R. Yazami, P. Touzain, J. Power Sources **1983**, 9, 365.

[15] M. M. Thackeray, W. I. F. David, P. G. Bruce, J. B. Goodenough, Mater. Res. Bull. **1983**, 18, 461.

[16] SONY, "Nexelion Hybrid Lithium Ion Battery," can be found under https://www.sony.net/SonyInfo/News/Press/200502/05-006E/, **2005**.

[17] A. K. Padhi, J. Electrochem. Soc. **1997**, 144, 1188.

[18] Z. Lu, D. D. MacNeil, J. R. Dahn, Electrochem. Solid-State Lett. **2001**, 4, A200.

[19] T. Ohzuku, Y. Makimura, Chem. Lett. **2001**, 30, 642.

[20] D. Larcher, J.-M. Tarascon, Nat. Chem. **2014**, 7, 19.

[21] M. S. Whittingham, Proc. IEEE **2012**, 100, 1518.

[22] U. Gulzar, S. Goriparti, E. Miele, T. Li, G. Maidecchi, A. Toma, F. De Angelis, C. Capiglia, R. P. Zaccaria, J. Mater. Chem. A **2016**, 4, 16771.

[23] M. Winter, R. J. Brodd, Chem. Rev. **2004**, 104, 4245.

[24] H. Cesiulis, N. Tsyntsaru, A. Ramanavicius, G. Ragoisha, Nanostructures and Thin Films for Multifunctional Applications, **2016**.

[25] C. Gabrielli, J. Electrochem. Soc. **1994**, 141, 1147.

[26] N. Nitta, G. Yushin, Part. Part. Syst. Charact. **2014**, 31, 317.

[27] J. Cabana, L. Monconduit, D. Larcher, M. R. Palacín, Adv. Mater. **2010**, 22, E170.

[28] B. Scrosati, Electrochim. Acta **2000**, 45, 2461.

[29] Y. Gogotsi, P. Simon, Science (80-.). **2011**, 334, 917.

[30] P. J. F. Harris, S. C. Tsang, J. B. Claridge, M. L. H. Green, J. Chem. Soc. Faraday Trans. **1994**, 90, 2799.

[31] M. Yudasaka, S. Iijima, V. H. Crespi, Growth Lakel. **2008**, 629, 605.

[32] D. P. Hashim, N. T. Narayanan, J. M. Romo-Herrera, D. A. Cullen, M. G. Hahm, P. Lezzi, J. R. Suttle, D. Kelkhoff, E. Muñoz-Sandoval, S. Ganguli, A. K. Roy, D. J. Smith, R. Vajtai, B. G. Sumpter, V. Meunier, H. Terrones, M. Terrones, P. M. Ajayan, Sci. Rep. **2012**, 2, 363.

[33] D. Kasuya, M. Yudasaka, K. Takahashi, F. Kokai, S. Iijima, J. Phys. Chem. B **2002**, 106, 4947.

[34] T. Yamaguchi, S. Bandow, S. Iijima, Chem. Phys. Lett. **2004**, 389, 181.

[35] H. Wang, M. Chhowalla, N. Sano, S. Jia, G. A. J. Amaratunga, Nanotechnology **2004**, 15, 546.

[36] K. Murata, K. Kaneko, H. Kanoh, D. Kasuya, K. Takahashi, F. Kokai, M. Yudasaka, S. Iijima, J. Phys. Chem. B **2002**, 106, 11132.

[37] J.-M. Bonard, R. Gaál, S. Garaj, L. Thien-Nga, L. Forró, K. Takahashi, F. Kokai, M. Yudasaka, S. Iijima, J. Appl. Phys. **2002**, 91, 10107.

[38] S. Mauro, Device and Method for Production of Carbon Nanotubes, Fullerene and Their Derivatives, **2010**.

[39] "NEC," can be found under http://www.nec.com/en/global/prod/cnh/, **n.d.**

[40] "Carbonium SRL," can be found under http://www.carbonium.it/public/site/index.php, **n.d.**

[41] "TIE GmbH," can be found under http://www.t-i-e.eu/index.php?id=2, **n.d.**

[42] J.-C. Charlier, G.-M. Rignanese, Phys. Rev. Lett. **2001**, 86, 5970.

[43] S. Berber, Y.-K. Kwon, D. Tománek, Phys. Rev. B **2000**, 62, R2291.

[44] C.-M. Yang, H. Noguchi, K. Murata, M. Yudasaka, A. Hashimoto, S. Iijima, K. Kaneko, Adv. Mater. **2005**, 17, 866.

[45] T. Ohba, T. Omori, H. Kanoh, M. Yudasaka, S. Iijima, K. Kaneko, Chem. Phys. Lett. **2004**, 389, 332.

[46] K. Murata, K. Kaneko, F. Kokai, K. Takahashi, M. Yudasaka, S. Iijima, Chem. Phys. Lett. **2000**, 331, 14.

[47] K. Murata, K. Kaneko, W. A. Steele, F. Kokai, K. Takahashi, D. Kasuya, K. Hirahara, M. Yudasaka, S. Iijima, J. Phys. Chem. B **2001**, 105, 10210.

[48] J. Adelene Nisha, M. Yudasaka, S. Bandow, F. Kokai, K. Takahashi, S. Iijima, Chem. Phys. Lett. **2000**, 328, 381.

[49] K. Ajima, M. Yudasaka, T. Murakami, A. Maigné, K. Shiba, S. Iijima, Mol. Pharm. **2005**, 2, 475.

[50] W. Xu, Z. Wang, Z. Guo, Y. Liu, N. Zhou, B. Niu, Z. Shi, H. Zhang, J. Power Sources **2013**, 232, 193.

[51] Y. Zhao, J. Li, Y. Ding, L. Guan, RSC Adv. **2011**, 1, 852.

[52] H. Lai, J. Li, Z. Chen, Z. Huang, ACS Appl. Mater. Interfaces **2012**, 4, 2325.

[53] F. Lodermeyer, R. D. Costa, D. M. Guldi, Adv. Energy Mater. **2017**, 7, 1.

[54] N. Karousis, I. Suarez-Martinez, C. P. Ewels, N. Tagmatarchis, Chem. Rev. **2016**, 116, 4850.

[55] Z. Zhang, S. Han, C. Wang, J. Li, G. Xu, Nanomaterials **2015**, 5, 1732.

[56] Y. Zhao, J. Li, Y. Ding, L. Guan, Chem. Commun. (Camb). **2011**, 47, 7416.

[57] W. Wu, Y. Zhao, C. Wu, L. Guan, RSC Adv. **2014**, 4, 28636.

Sulfur mine in Ijen Crater Indonesia Credits: http://www.indonesia-tourism.com

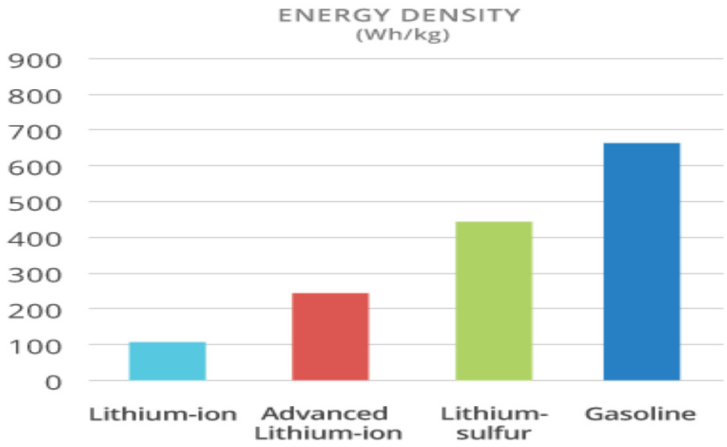

2 Achieving Higher Capacities using Nitrogen Doped SWCNHs based Composites for Lithium Sulfur Batteries

Abstract

High surface area of single wall carbon nanohorns allow them to encapsulate sulfur which can be used as a cathode material for lithium sulfur batteries. In this work, this characteristic was further enhanced by considering their nitrogen doping, as it is expected to increase the electronic and chemisorption properties of SWCNHs. Therefore, we explore for the first time the electrochemical performance of nitrogen doped SWCNHs as a sulfur encapsulating conductive material. A simple scalable method was used to synthesize N-SWCNHs-S composites and its electrochemical performance was evaluated using cyclic chronopotentiometry and impedance spectroscopy. Fabrication of lithium-sulfur cells based on N-SWCNHs-S composite could indeed achieve a remarkable initial gravimetric capacity of 1650 mAh g^{-1}, namely equal to 98.5% of the theoretical capacity (1675 mAh g^{-1}), with an exceptional sulfur content as high as 80 % at 0.1 C.

2.1 Introduction

Lithium ion batteries have been successfully serving the demand of portable energy storage since their commercialization in 1990. However, they are approaching their practical performance limits (140-240 Wh/Kg), hence unable to cope with ever increasing energy demand (~500-600 Wh Kg^{-1}) for electric vehicles and smart grid applications[1,2]. Therefore, research in high Ragone battery systems (high energy and power density) is critical for developing next-generation thinner, lighter and lower-cost battery systems.

The limiting factor impeding the development of high capacity battery system is the cathode side where transition metal oxides ($LiCoO_2$, $LiMnO_2$ and $LiFePO_4$) are commonly used as an active lithium storage material. Although these transition metal oxides operates at high potentials (4-4.5V vs Li/Li^+), nevertheless, they are limited by low storage capabilities. In search of new materials for cathodes, sulfur is the most promising alternative for future energy applications due to its high theoretical capacity (1675 mAh g^{-1}) and energy density (~2600 Wh Kg^{-1}). Although, Lithium air (Li-air) batteries provide higher energy densities (~3505 Wh Kg^{-1}), Li-S cells with solid-state sulfur cathode are expected to receive fewer commercialization challenges than Li-air cells, the latter needing gaseous cathodes [3]. Moreover, high abundance of sulfur along with its low cost makes lithium–sulfur batteries dominantly attractive and low-cost energy storage technology.

Despite the commercialization of Li-S batteries by OXIS Energy [4], SION POWER [5], and GS Yuasa[6], practical application of Li-S battery is still hindered by three main

challenges, namely a) poor electronic and ionic conductivities of sulfur (S_8) and lithium sulfide (Li_2S) [7] b) structural pulverization after multiple lithiation/de-lithiation c) dissolution of intermediate lithium polysulfides (Li_2S_x, $x \geq 4$) in electrolyte solution instigating shuttle effect [8]. Once polysulfides are dissolved in electrolyte they shuttle between anode and cathode during lithiation and de-lithiation inhibiting the complete utilization of the active material[9]. Moreover, the shuttled polysulfides react with the lithium metal anode, causing rapid corrosion of lithium along with the deposition of Li_2S on both the electrodes, giving rise to significant increase in impedance. Once the surface is completely covered, the electrochemical reaction stops and the cell ends its life.

Major breakthroughs in solving these problems came from Nazar et. al [10] and Mikhaylik et al. [11] where former used a conductive mesoporous carbon-host for sulfur encapsulation while later developed an electrolyte additive ($LiNO_3$) to limit shuttle effect by passivating lithium electrode. Later, different conductive materials like carbon nanotubes [12–17], graphene [18–22] and various polymers [23–26] have been employed as a host for sulfur encapsulation while nitrogen/oxygen doping [27–32] and metal oxide [33–37] have been extensively used to entrap polysulfides for reducing shuttle effect. Although, these carbon-based sulfur composite seems to show outstanding electrochemical performances, high capacity and long cyclability could not be simultaneously achieved with high sulfur content ($\geq$ 70 wt%).

Despite the unique properties of SWCNHs as conducting agents (discussed in Chapter 1), few accounts were found related to their application as anode material for lithium ion[38–40] and cathode material for lithium sulfur batteries[41] where former

used SWCNHs as a host material for metal oxides (Fe_2O_3, MnO_2 and TiO_2) nanoparticles while later used it for sulfur encapsulation. Therefore, we report for the first time nitrogen doped single wall carbon nanohorns (N-SWCNHs) as sulfur encapsulating hosts to be used as cathode material for Li-S batteries. In particular, the choice of nitrogen is motivated by the quest for improved interaction between SWCNHs and the surrounding active material. In this regard, nitrogen as doping agent is suggested for its high electronegativity, which realizes C-N bonds characterized by permanent electric dipoles located at the surface of the nanohorns. This effect is expected to increase the surface chemical reactivity of N-SWCNHs, hence inducing the link between nitrogen sites and the surrounding active material (sulfur in the present case)[42].

2.2 Experimental

2.2.1 Preparation of N-SWCNHs-sulfur composites

Nitrogen doped single wall carbon nanohorns (N-SWCNHs) were provided by Advanced Technology Party s.r.l., Italy. N-SWCNHs-S composite was prepared by a facile melt diffusion method. Typically, N-SWCNHs and sulfur (99.99%, STERM Chemicals) with weight ratios of 1:5 were dissolved in 5 mL of carbon disulfide (CS_2) (≥ 99%, anhydrous) and sonicated for 1 hr at room temperature. After evaporating CS_2, dried carbon-sulfur mixture was placed in crucible and heated at 155 ^{0}C for 24 hours under argon environment.

2.2.2 Material characterizations

Thermogravimetric analysis (TGA) was carried out using TGA Q500-TA Instrument. Samples were heated from 30 °C to 500 °C at a heating rate of 10 °C/min under nitrogen atmosphere which was set at a flow rate of 50 mL/min. Transmission electron microscopy images were obtained using a JEOL JEM 1011 (Jeol, Tokyo, Japan) operating at 100 kV acceleration voltage, equipped with a tungsten thermionic electron source and a FEI TECNAI G2 F20 instrument, equipped with a Schottky field emission gun (FEG), operating at 200 kV acceleration voltage. Scanning electron microscopy was carried out with a Nova 600 NanoLab microscope (FEI), equipped with a field emission gun for scanning electron imaging and a focused ion beam of gallium ions for milling. XRD patterns were collected on a PANalytical Empyrean X-ray diffractometer equipped with a 1.8 kW CuKα ceramic X-ray tube, PIXcel3D 2 x 2 area detector and operating at 45 kV and 40 mA. Raman spectroscopy measurements were carried out with Renishaw in Via Micro Raman equipped with a laser source at 633 nm through a 50x objective (LEICA N PLAN EPI 50/ 0.75). X-ray photoelectron spectroscopy (XPS) analysis was performed on a Kratos Axis Ultra DLD spectrometer, using a monochromatic Al Kα source (15 kV, 20 mA). High resolution narrow scans were performed at constant pass energy of 20 eV and steps of 0.1 eV. The photoelectrons were detected at a takeoff angle θ = 0° with respect to the surface normal. The pressure in the analysis chamber was maintained below 7×10^{-9} Torr for data acquisition. The data were converted to VAMAS format and processed using Casa XPS software, version 2.3.16. The binding energy (BE) scale was internally referenced to the C 1s peak (BE for C–C = 284.8 eV).

Specific surface area and porosity measurements were carried out by nitrogen physisorption at 77 K in a Quantachrome equipment, model autosorb iQ. Prior to measurements, samples were degassed for 3 hours at 200°C under vacuum to eliminate weakly adsorbed species. The specific surface areas were calculated using the multi-point BET (Brunauer–Emmett–Teller) model, considering 11 equally spaced points in the P/P0 range from 0.05 to 0.30. The micropore volume and micropore area were obtained by the t-plot Carbon Black method (R. W. Magee, Evaluation of the External Surface Area of Carbon Black by Nitrogen Adsorption, Presented at the meeting of the Rubber Division of the American Chem. Soc., October, 1994.). The Horvath-Kawazoe (HK) method was instead applied to determine the micropore size distribution.

2.3 Electrochemical Characterization

The electrochemical performance of as-prepared N-SWCNHs-S composite was tested using CR2032 coin cells which consist of lithium chips (15.6 Dia x 0.45t mm; MTI Corporations) as reference and counter electrode, dried glass fibers membrane (Whatman GF/D) as separator and C-S composite, casted on a pre-etched aluminum foil, as working electrode. Slurries casted on aluminum foil (15 mm Dia) were composed of 90% C-S composite, 5% super-P carbon and 5% polyvinylidene difluoride (PVDF) mixed with an appropriate amount of N-methyl-2-pyrrolidone. The casted electrodes were dried overnight at 60 ^{0}C under vacuum and the mass loadings of active material were found in the range of 1-1.2 mg. 250 μL of electrolyte was used in each coin cell which contain 1molL^{-1}lithium

bis(trifluoromethanesulphonyl)imide in 1:1 (v/v) of 1,4-dioxane and 1,2-dimethoxyethane with 0.1 mol L^{-1} of $LiNO_3$ as an additive. After assembling inside MBraun glovebox, with H_2O and O_2 levels below 0.1 ppm, all cells were electrochemically tested using BioLogic BCS-805 multichannel battery unit controlled by BT Lab V1.30. Impedance analyses were performed using the same instrument in the frequency range of 10 kHz to 100 mHz with a voltage amplitude of 5 mV. Impedance spectra were simulated and fitted using biologic integrated software Z-SIM and Z-Fit.

2.4 Result and discussion

2.4.1 Material Synthesis and Characterization

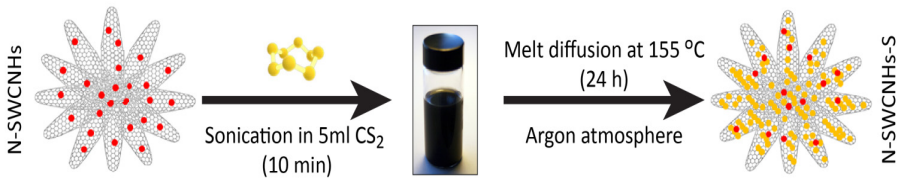

Figure 2.1: Schematic illustration describing the sulfur encapsulation of N-SWCNHs. The red and orange dots represent the N and S doping, respectively.

Figure 2-1 illustrates the synthetic scheme of N-SWCNHs-S composites, prepared by a facile melt diffusion method. N-SWCNHs and sulfur with weight ratios of 1:5 were dissolved in 5 ml of carbon disulfide (CS_2) and sonicated for 10 min at room temperature. After drying the mixture was placed in a crucible and heated to 155 °C for 24 hours under argon environment. The temperature choice was dictated by the

minimum viscosity of sulfur, which facilitates the diffusion of sulfur into N-SWCNHs.

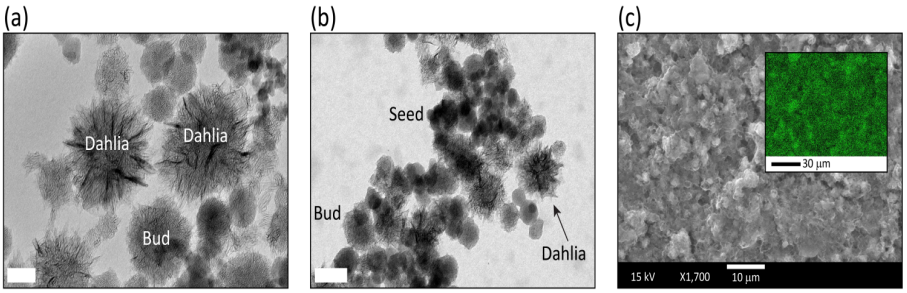

Figure 2.2: a) TEM images of N-SWCNHs with dahlia- and bud-like aggregates. Scale bar 50 nm. b) TEM image of N-SWCNHs-S composites. Scale bar 100 nm. c) SEM image of N-SWCNHs-S composite electrode. Inset: EDS mapping of sulfur distribution (green represents sulfur, black is carbon).

As discussed in Chapter 1, three different types of SWCNHs aggregates including 'dahlia-like', 'bud-like', and 'seed-like' have been reported[43]. Our TEM analysis of N-SWCNHs depicted in **Figure 2-2a** shows dahlia-like (100-150 nm) and bud-like (80-100nm) aggregates while **Figure 2-2b** shows their aggregation after sulfur encapsulation. To confirm the homogeneity of active material (Sulfur), electrodes prepared from 90% N-SWCNHs-S composite, 5% carbon black and 5% PVDF were analysed using scanning electron microscopy (SEM) and energy dispersive X-ray spectroscopy (EDS). The results shown in **Figure 2-2c** and inset demonstrate a homogenous distribution of sulfur after the fabrication process.

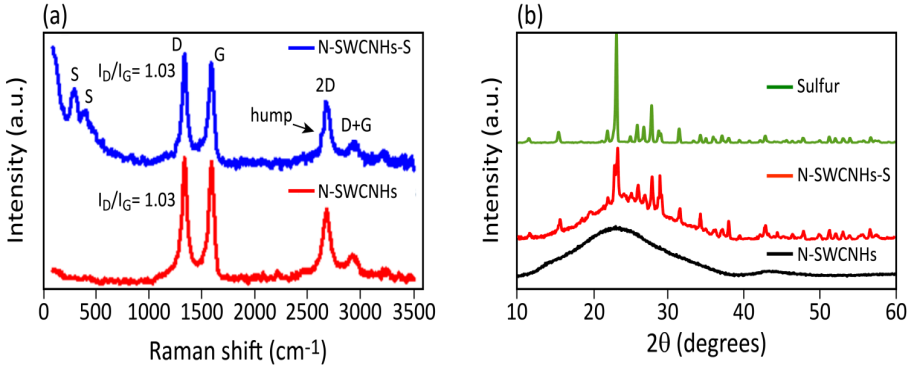

Figure 2.3: a) Raman spectra of N-SWCNHs and sulfur composite. b) XRD patterns of N-SWCNHs, N-SWCNHs-S and pure sulfur taken as reference.

Due to the graphitic nature of N-SWCNHs, Raman analysis was performed to elucidate the defected nature of N-SWCNHs, as illustrated in **Figure 2-3a**. Two prominent peaks in the Raman spectrum of SWCNHs are associated to the D and G bands where the former is attributed to disordered sp^2 carbon caused by the presence of defects while the latter is related to the vibrational modes of graphitic carbons[44]. Due to the topological defects of pentagons and heptagons in SWCNHs, these D and G peaks appears at 1348 and 1590 cm^{-1}, respectively[45]. **Figure 2-3a** also shows the Raman spectrum of N-SWCNHs-S. Peaks are observed near 1350 cm^{-1} (D), 1589 cm^{-1} (G), 2676 cm^{-1} (2D), 2953 cm^{-1} (D+G) and 3225 cm^{-1} (2D'). I_D/I_G ratio was calculated for both spectra providing values close to unity, result which is explained through the peculiar defects structure associated to N-SWCNHs[45]. Finally, peaks of sulfur appear in the range of 300-500 cm^{-1} demonstrating its physical encapsulation inside or on the surface of the carbon material. Interestingly, a hump at 2628 cm^{-1} was observed in N-SWCNHs-S composites, where the splitting of the 2D peak into

$2D_1$ and $2D_2$ suggests the stacking of carbon material due to a strong interaction between sulfur and nitrogen groups.

X-ray Diffraction (XRD) analysis was then performed to confirm the presence as well as the crystalline structure of sulfur inside N-SWCNHs-S composite. **Figure 2-3b** depicts XRD analysis of pure sulfur, pristine N-SWCNHs and their sulfur composites. The pattern of pristine N-SWCNHs shows a broad (002) peak around $2\theta = 23°$. This wide d_{002} peak is commonly observed in structures with turbostratic stacking of the graphene sheets[46]. An additional peak at $2\theta \sim 43°$, can be readily assigned to the (10) reflection. Finally, the XRD pattern of N-SWCNHs-S composite (red line) shows the presence of characteristic peaks of orthorhombic sulfur (ICSD reference code: 27261) on top of the broad peaks of N-SWCNHs previously described.

The surface chemical properties of N-SWCNHs and N-SWCNHs-S composite were then studied through X-ray Photoelectron Spectroscopy (XPS). **Figure 2-4a** shows the XPS spectrum collected on N-SWCNHs: C 1s, N 1s and O 1s peaks are clearly visible, hence confirming the presence of nitrogen as well as carbon and oxygen within the aggregates. The C 1s peak **(Figure 2-4c)** shows the typical shape for graphitic-like compounds[47] given by an asymmetric peak centred at 284.4±0.2 eV (corresponding to sp^2-hybridized carbon atoms) accompanied by a low intensity shake-up feature at 290.8±0.2 eV, related to $\pi \rightarrow \pi^*$ transition. The best fit of the C 1s profile has been obtained by adding other low intensity peaks, ascribable to adventitious carbon species[48] (peaks centred at 284.9±0.2 eV, 286.4±0.2 eV, 288.0±0.2 eV and 289.7±0.2 eV, assigned respectively to sp^3-hybridized carbon

atoms, C-O, C=O and O-C=O species). The peak at 286.4±0.2 eV is also due to C-N species, corresponding to the N-sp^2 C bonds originated from the inclusion of N atoms in the carbon network of the nanohorns[49]. This assignment is supported by the presence of the N 1s broad peak appearing between 396 and 406 eV **(Figure 2-4d)**; it could be decomposed into three components centred at 399.0±0.2 eV, 400.8±0.2 eV, and 402.2±0.2 eV, corresponding respectively to pyridinic, pyrrolic, and graphitic nitrogen[50] hence confirming the presence of nitrogen doping, together with a fourth component at 404.3±0.2 eV, assigned to oxidized N forms.

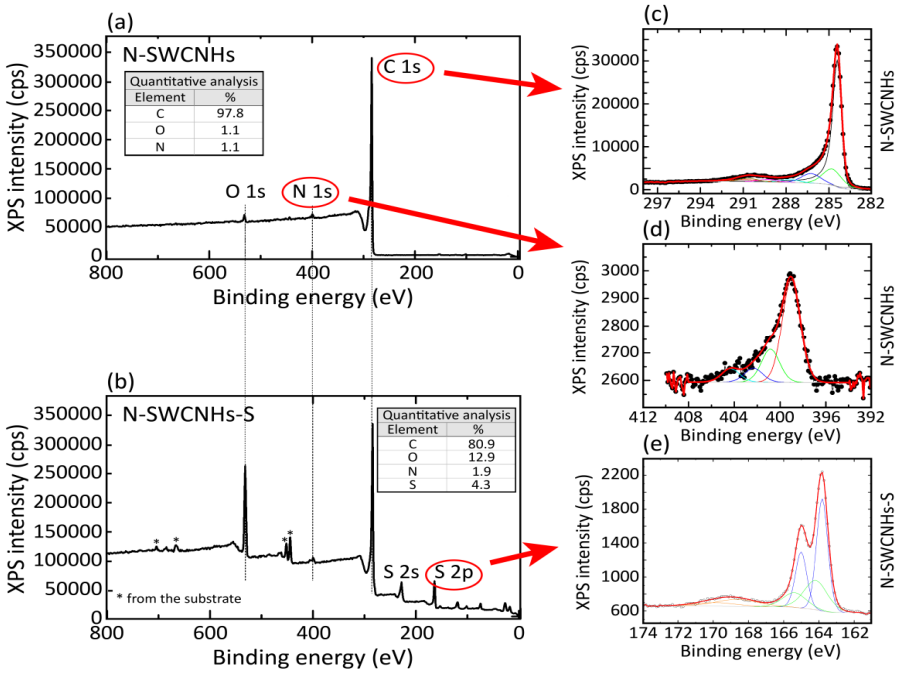

Figure 2.4: a) XPS spectra of N-SWCNHs; b) N-SWCNHs-S composite mixed with carbon black and PVDF; c) and d) High resolution spectra of C1s and N1s peaks; e) High resolution spectrum of S2p peak in the range of 162-174 eV.

The atomic percentage of carbon, nitrogen and oxygen were found to be 97.8, 1.1 and 1.1%, respectively **(Figure 2-4a)**.

Similar analysis has been carry out on the electrode material, containing N-SWCNHs-S composite, carbon black, and PVDF. **Figure 2-4b** clearly shows the presence of S 2s and S 2p peaks confirming the presence of sulfur in the electrode slurry. High resolution analysis on the S 2p peaks energy region (**Figure 2-4e**) revealed that sulfur is present mainly as elemental S (S $2p_{3/2}$ component centred at 163.8 eV); low intensity S components are also observed at higher binding energy values (S $2p_{3/2}$ component centred at 164.2 eV and at 168.6 eV) and could be assigned to oxidized S species[29].

SWCNHs are known to possess micro (pore size less than 2 nm) and meso-porosity (2-50nm), originating from their peculiar morphology[51]. This suggests that SWCNHs might retain high surface area even after nitrogen doping, so that sulfur can infiltrate especially at 155 °C where it shows its lowest viscosity, hence enabling intimate contact between sulfur and the conductive carbon material[52]. To verify this aspect N_2 physisorption analysis was performed to determine the surface area and the pores size distribution of the as prepared N-SWCNHs and N-SWCNHs-S aggregates. **Figure 2-5a** shows the N_2 adsorption/desorption isotherm obtained for N-SWCNHs and N-SWCNHs-S, the former exhibiting mixed type I and II isotherms, indicating the existence of pore sizes ranging from micropores (pore width: 0.4-1.0 nm, see inset in **Figure 2-5a**) to macropores with total surface area of 211 $m^2 g^{-1}$ and total pore volume of 1.097 $cm^3 g^{-1}$. Moreover, for N-SWCNHs, we observed that the micro-pores represent only a minor fraction of the total pore sizes

(2.3 %), with an estimated volume of 0.025 $cm^3\ g^{-1}$, as summarized in **Table 2-1**. On the opposite side, N-SWCNHs-S composites showed significantly lower surface area of about 12 $m^2\ g^{-1}$ due to the sulfur infiltration.

Table 2-1: Pore-structure parameters of N-SWCNHs. Here a_t, a_{ext}, and V_t stand for total surface area, area excluding the contributions from micro-pores and total volume, respectively.

Sample	**Pore-structure parameters**				
	a_t	a_{ext}	V_t	$V_{micro\text{-}porous}$	$V_{meso\text{-}porous}$
	(m^2/g)	(m^2/g)	(cm^3/g)	(cm^3/g)	(cm^3/g)
N-SWCNHs	211	156	1.097	0.025	1.072

Finally, thermo-gravimetric analysis (TGA) was performed to determine the sulfur content in N-SWCNHs-S composites. **Figure 2-5b** illustrates a sharp decrease in weight for temperature increase from 115 °C to 300 °C corresponding to the removal of sulfur. In particular, TGA shows that sulfur accounts for about the 80% of the total weight of N-SWCNHs-S composites therefore suggesting an effective bonding between sulfur and N-SWCNHs.

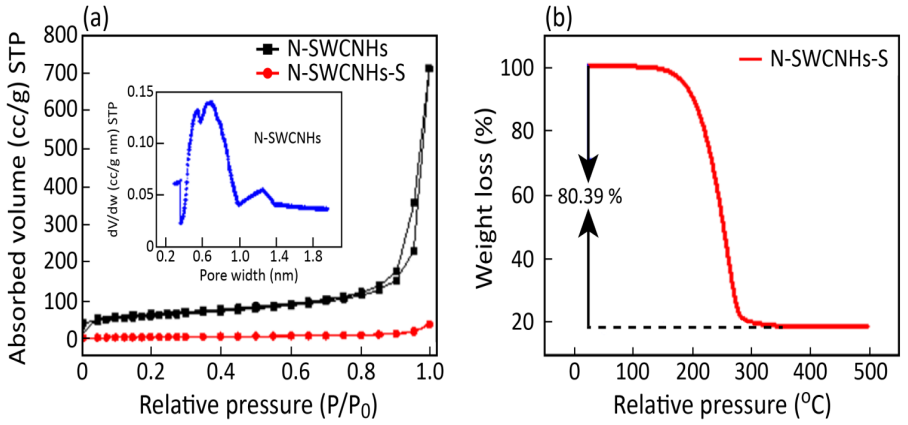

Figure 2.5: a) N_2 adsorption/desorption isotherms of N-SWCNHs and N-SWCNHs-S measured at standard temperature and pressure (STP). Inset: Pore width of N-SWCNHs, where V is the volume adsorbed in cc and w is the pore width in nm. The data are normalized vs. the weight. (b) TGA analysis of N-SWCNHs-S composites.

2.4.2 Electrochemical characterization

In order to explore N-SWCNHs-S composites as cathode material for Li-S batteries, electrochemical properties of N-SWCNHs-S composites were tested using cyclic chrono-potentiometry (galvanostatic charge/discharge measurements) and impedance spectroscopy. To understand the redox process of sulfur, differential capacity plots of N-SWCNHs-S composites were produced from galvanostatic charge discharge profiles, as shown in **Figure 6a**. It is quite known that the distribution of polysulfides and their reduction potentials depend on the nature of the electrolyte, the sulfur to electrolyte ratio, current density, sulfur electrode composition and its architecture[53,54]. In our case, three prominent reductive peaks were observed in the range of 2.39-2.29 V (region I), 2.17-2.09 V (region II) and 2.08-1.90 V (region III). The peaks in the regions I to III are usually associated to the

reduction of sulfur typical of lithium-sulfur chemistries. In particular, region I corresponds to a relatively fast conversion of elemental sulfur (S_8) into lithium polysulfide anions (Li_2S_x; where x is typically 4–6) while region III corresponds to the conversion of polysulfides into Li_2S_2 and then to Li_2S[55]. Furthermore, we observed additional peaks in the region II which can be associated to the electrochemical conversion of long chain polysulfides to their shorter counterparts[56].

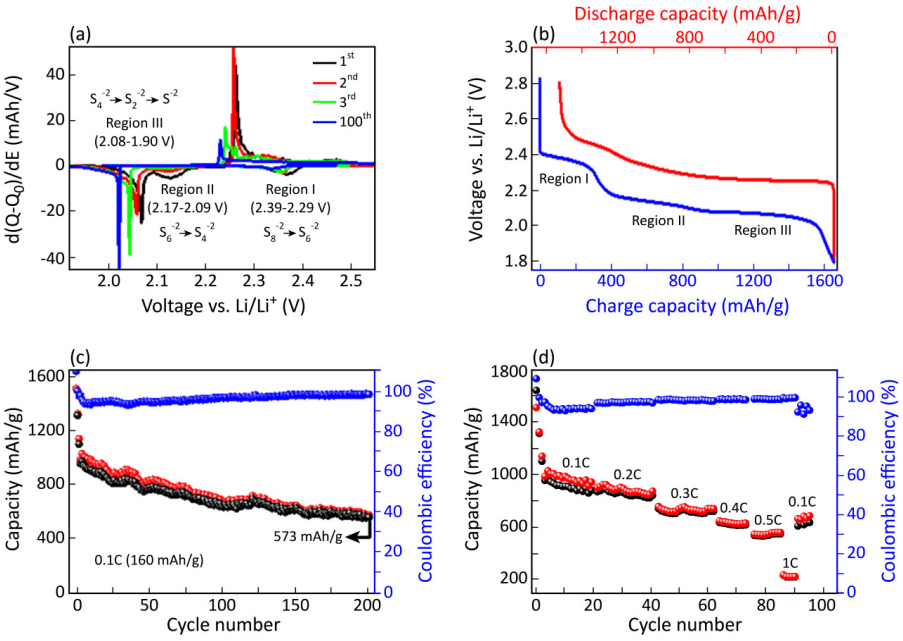

Figure 6. Electrochemical characterization. a) Differential Capacity plot (dQ/dE) of N-SWCNHs-S composite. b) Charge/discharge profile of N-SWCNHs-S composite. c) Cycling performance of N-SWCNHs-S composite at 0.1 C. d) Cycling performance of N-SWCNHs-S composites at different C-rates.

Figure 6b shows charge/discharge profile of N-SWCNHs-S composites represented by three plateaus corresponding to the three regions highlighted in **Figure 6a**. The achieved initial gravimetric capacity at 0.1 C was 1650 mAh g^{-1}, extremely close to

the theoretical capacity (1675 mAh g^{-1}), as shown in **Figure 6c**. However, a fast capacity decay was recorded during first few cycles with a total capacity loss of about 65 % after 200 cycles. It is interesting and important to notice that the majority of the capacity was lost during the first three cycles (40 %) while only 25 % loss was observed for the remaining 197 cycles with a columbic efficiency in the range of 95-97%. This initial rapid decay can be explained by the dissolution of polysulfide ions from the electrode surface. Once the electrode surface becomes free of polysulfide the capacity stabilizes as the pores of N-SWCNHs are able to avoid further dissolution of polysulfide into the bulk electrolyte due to their confinement properties. This stable behavior can be observed especially in the last 100 cycles where the capacity loss was merely 5 %. Additionally, the capacity associated to lowest plateau (region III) accounts for 65 % of the total capacity, which remains almost constant during cycling, while the remaining 35 % is associated to the upper plateaus (regions I and II), which decrease with increasing cycle numbers. After 200 cycles, the gravimetric capacity for N-SWCNHs-S composites was found to be 573 mAh g^{-1} at 0.1C. In this respect, the columbic efficiency showed an improved response over cycling, approaching 100% after 200 cycles. The performance of the N-SWCNHs-S electrode was also examined at various C-rates as shown in **Figure 6d.** The discharge capacities of ~ 1100, 890, 725, 258, 630, 560 and 250 mAh g^{-1} were recorded at the current rates of 0.1C, 0.2C, 0.3C, 0.4C, 0.5C, 1C, respectively.

2.4.3 Impedance Spectroscopy

To understand the dissolution of polysulfides ions from the electrode surface, Electrochemical Impedance Spectroscopy (EIS) was performed at various stages of

lithiation. The impedance spectra, shown in **Figure 7**, were obtained at different stage of discharge (from 2.6 V, corresponding to open circuit voltage, down to 2 V) in the frequency range from 10 KHz to 10 mHz with a stimulus amplitude of 5 mV.

The Nyquist plots illustrated in **Figure 7a-d** show a high frequency (HF) depressed semicircle and a low frequency (LF) straight line. In particular, the intercept in the HF region is related to internal resistance (R_1) of the electrolyte, separator, and current collectors whereas the intercept from the high to middle frequency range is related to the charge transfer processes at the electrode/electrolyte interface (R_2). The straight line at LF is instead associated to the diffusion of lithium ions inside the N-SWCNHs-S composite while sulfur is still in its solid elemental form. When the Nyquist plots for the regions I, II and III are compared to the OCV (Open Circuit Voltage) counterpart, a decrease in charge transfer resistance R_2 is observed (**Figure 7f**). Similarly and specifically for the regions I and II, a suppressed straight line in the LF range is also noticed.

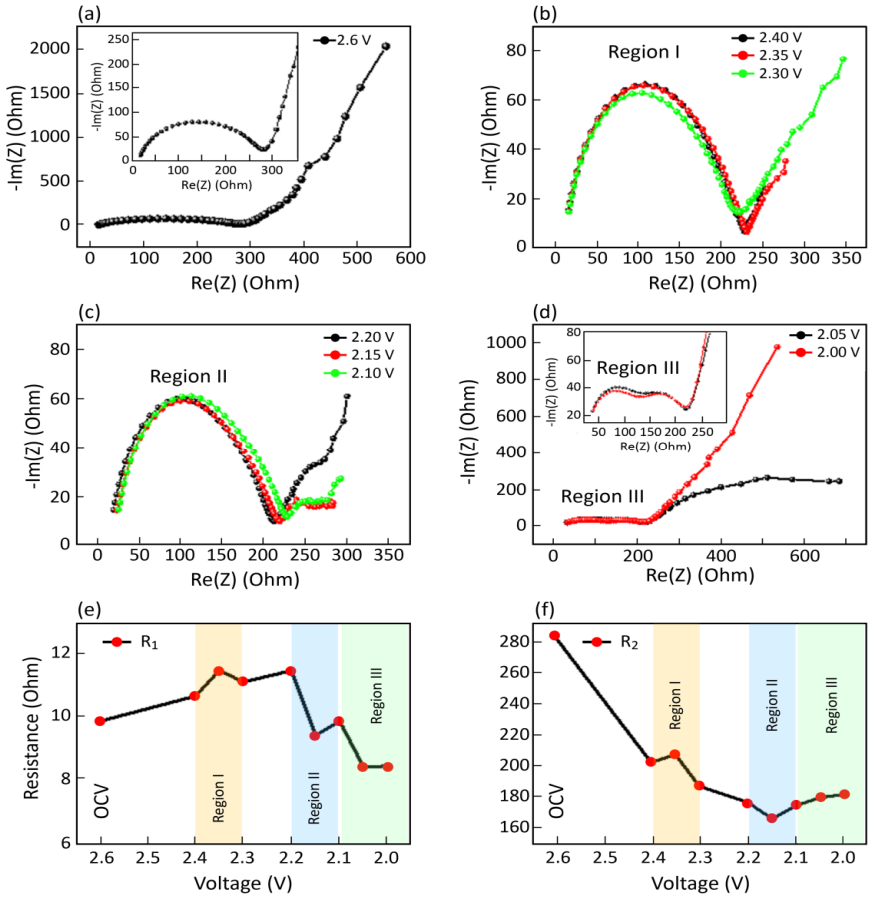

Figure 7. (a)-(d) Impedance spectra of N-SWCNHs-S composite at different stages of lithiation. a) OCV (2.6 V). In b), c) and d) are shown the impedance behaviors of the three regions highlighted in Figure 6a. e) Variation in internal resistance (R_1) at different voltages during discharge. f) Variation of charge transfer resistance (R_2) at different voltage during discharge.

This rapid lowering of both R_2 and the straight line is consequence of the dissolution of polysulfides from the solid cathode into the liquid electrolyte, resulting in high polysulfides mobility and in a cathode surface with beneficial higher porosity/surface area, two characteristics leading to enhanced charge transfer process and increased

ionic/electronic conductivity [57]. Furthermore, in the region I, the dissolution of polysulfide into the electrolyte increases its internal resistance (R_1) from 9.61 to 10.51 Ω due to an increased viscosity (**Figure 7e**). A small semi-circle starts also to appear at 2.15V (region II) and becomes prominent in the region III (**Figure 7c**) suggesting the formation of Li_2S while, due to the consumption of polysulfide from the electrolyte, a slight decrease in electrolyte resistance (R_1) is observed until the end of discharge process (**Figure 7e**). At the end of the discharge process (region III), two depressed semi-circles appear along with the reappearance of the straight line in the LF range, the latter associated to the diffusive behavior of lithium inside solid Li_2S. We suggest that the variation in the slope of the straight line could be ascribed to the thickness of Li_2S, where a thin layer of Li_2S allows for less hindrance as compared to a thick Li_2S layer, which is formed at the end of discharge phase. Finally, the semi-circle in the HF range is associated to the conversion of the remained polysulfide on the surface of N-SWCNHs into smaller polysulfide whereas the semi-circle in the middle frequency region (MF) range is related to the formation of Li_2S.

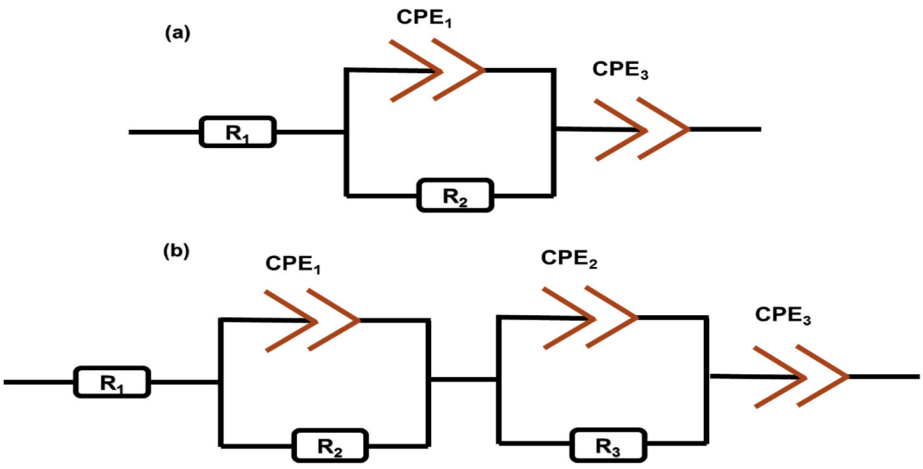

Figure 8. Proposed equivalent circuits of lithium-sulfur cell. R_1 represents the resistance of electrolyte and conductors, CPE_x are the constant phase elements and $R_{2,3}$ are associated to the charge transfer resistances. (a) and (b) describe the behavior of electrode before (OCV, region I and II) and after the formation of Li_2S phase (region III), respectively.

In order to reproduce the non-ideal behaviour of N-SWCNHs-S based electrode, therefore to design the plots in **Figure 7**, we have employed a R//CPE circuit description rather than several R//C circuits in series, as depicted in **Figure 8**, where the Constant Phase Element (CPE) translates in an empirical manner the non-ideal behaviour of the composite electrode[58] (porosity of the material, roughness of the surface). In this regard, CPE_1 and CPE_2 describe the amplitudes of the semicircles, whereas CPE_3 is associated to the Warburg region (straight line) in the LF region. **Figure 8a** describes the circuit capable of modelling OCV, regions I and II, whereas upon the appearing of an additional semi-circle in the MF region for lower potentials (region III), a different circuit scheme requiring one extra CPE//R has to be considered, as shown in **Figure 8b**.

2.5 Conclusions

We have explored the physical and electrochemical properties of nitrogen doped single wall carbon nanohorns (N-SWCNHs) with the intent of achieving an enhanced sulfur encapsulation to realize an efficient cathode material for lithium-sulfur batteries. Our results show that N-SWCNHs-S composites give higher gravimetric capacity with respect to previously reported method [41] where just SWCNHs were employed, providing remarkable capacity values as high as 1650 mAh g^{-1} at 0.1 C, corresponding to 98.5 % of the theoretical capacity (1675 mAh g^{-1}).

A detailed impedance analysis was also performed to understand the behaviour of polysulfide formation in our lithium-sulfur cells. From our results we can conclude that N-SWCNHs represent an innovative and cheap solution for sulfur encapsulation. Indeed, owing to their peculiar morphology characterized by high density of micro/mesopores which can assist the mass transport of lithium-ions as well as enhance the active reaction sites density, N-SWCNHs are recognized to provide a fundamental contribute to the improvement of the initial capacity.

Finally, these findings suggest that a proper engineering of the micro-porosity and nitrogen doping of N-SWCNHs might be a valid approach to reduce the shuttle effect hence making this active material stable at higher capacities with even higher rate performance.

2.6 References

[1] M. Wild, L. O'Neill, T. Zhang, R. Purkayastha, G. Minton, M. Marinescu, G. J. Offer, *Energy Environ. Sci.* **2015**, *8*, 3477.

[2] Z. W. Seh, Y. Sun, Q. Zhang, Y. Cui, *Chem. Soc. Rev.* **2016**, *45*, 5605.

[3] P. G. Bruce, S. a. Freunberger, L. J. Hardwick, J.-M. Tarascon, *Nat. Mater.* **2011**, *11*, 172.

[4] **n.d.**

[5] "http://www.sionpower.com/," **n.d.**

[6] "GS Yuasa Lithium Power," can be found under http://www.gsyuasa-lp.com/, **2017**.

[7] D.-H. Kim, B. Lee, K.-Y. Park, K. Kang, *Chem. - An Asian J.* **2016**, n/a.

[8] Y. V. Mikhaylik, J. R. Akridge, *J. Electrochem. Soc.* **2004**, *151*, A1969.

[9] C. Barchasz, F. Molton, C. Duboc, J. C. Leprêtre, S. Patoux, F. Alloin, *Anal. Chem.* **2012**, *84*, 3973.

[10] X. Ji, K. T. Lee, L. F. Nazar, *Nat. Mater.* **2009**, *8*, 500.

[11] Y. V. Mikhaylik, *Electrolytes for Lithium Sulfur Cells*, **2008**, US7354680 B2.

[12] L. Yuan, H. Yuan, X. Qiu, L. Chen, W. Zhu, *J. Power Sources* **2009**, *189*, 1141.

[13] J. Guo, Y. Xu, C. Wang, *Nano lett.* **2011**, *11*, 4288.

[14] Z. W. Seh, Q. Zhang, W. Li, G. Zheng, H. Yao, Y. Cui, *Chem. Sci.* **2013**, *4*, 3673.

[15] L. Sun, M. Li, Y. Jiang, W. Kong, K. Jiang, J. Wang, S. Fan, *Nano Lett.* **2014**, *14*, 4044.

[16] S. Dörfler, M. Hagen, H. Althues, J. Tübke, S. Kaskel, M. J. Hoffmann, *Chem. Commun.* **2012**, *48*, 4097.

[17] G. Zheng, Y. Yang, J. J. Cha, S. S. Hong, Y. Cui, *Nano Lett.* **2011**, *11*, 4462.

[18] J.-Z. Wang, L. Lu, M. Choucair, J. a. Stride, X. Xu, H.-K. Liu, *J. Power Sources* **2011**, *196*, 7030.

[19] K. Zhang, L. Wang, Z. Hu, F. Cheng, J. Chen, *Sci. Rep.* **2014**, *4*, 6467.

[20] H. Wang, Y. Yang, Y. Liang, J. T. Robinson, Y. Li, A. Jackson, Y. Cui, H. Dai, *Nano lett.* **2011**, *11*, 2644.

[21] H. Chen, C. Wang, W. Dong, W. Lu, Z. Du, L. Chen, *Nano Lett.* **2015**, *15*, 798.

[22] M.-Q. Zhao, Q. Zhang, J.-Q. Huang, G.-L. Tian, J.-Q. Nie, H.-J. Peng, F. Wei, *Nat. Commun.* **2014**, *5*, 3410.

[23] F. Wu, J. Chen, R. Chen, S. Wu, L. Li, S. Chen, T. Zhao, *J. Phys. Chem. C* **2011**, *115*, 6057.

[24] J. Wang, J. Chen, K. Konstantinov, L. Zhao, S. H. Ng, G. X. Wang, Z. P. Guo, H. K. Liu, *Electrochim. Acta* **2006**, *51*, 4634.

[25] L. Xiao, Y. Cao, J. Xiao, B. Schwenzer, M. H. Engelhard, L. V. Saraf, Z. Nie, G. J. Exarhos, J. Liu, *Adv. Mater.* **2012**, *24*, 1176.

[26] W. Zhou, Y. Yu, H. Chen, F. J. Disalvo, H. D. Abruña, *J. Am. Chem. Soc.* **2013**, *135*, 16736.

[27] Y. Cao, X. Li, I. a Aksay, J. Lemmon, Z. Nie, Z. Yang, J. Liu, *Phys. Chem. Chem. Phys.* **2011**, *13*, 7660.

[28] L. Ji, M. Rao, H. Zheng, L. Zhang, O. Y. Li, W. Duan, *J. Am. Chem. Soc.* **2011**, *133*, 18522.

[29] L. Zhang, L. Ji, P.-A. Glans, Y. Zhang, J. Zhu, J. Guo, *Phys. Chem. Chem. Phys.* **2012**, *14*, 13670.

[30] Z. Wang, X. Niu, J. Xiao, C. Wang, J. Liu, F. Gao, *Rsc Adv.* **2013**, *3*, 16775.

[31] S. H. Chung, P. Han, A. Manthiram, *ACS Appl. Mater. Interfaces* **2016**, *8*, 4709.

[32] G. Zheng, Q. Zhang, J. J. Cha, Y. Yang, W. Li, Z. W. Seh, Y. Cui, *Nano Lett.* **2013**, *13*, 1265.

[33] N. Ding, L. Zhou, C. Zhou, D. Geng, J. Yang, S. W. Chien, Z. Liu, M.-F. Ng, A. Yu, T. S. A. Hor, M. B. Sullivan, Y. Zong, *Sci. Rep.* **2016**, *6*, 33154.

[34] Q. Pang, L. F. Nazar, *ACS Nano* **2016**, *10*, 4111.

[35] Z. Wei Seh, W. Li, J. J. Cha, G. Zheng, Y. Yang, M. T. McDowell, P.-C. Hsu, Y. Cui, *Nat. Commun.* **2013**, *4*, 1331.

[36] Q. Pang, D. Kundu, M. Cuisinier, L. F. Nazar, *Nat Commun* **2014**, *5*, 4759.

[37] X. Tao, J. Wang, C. Liu, H. Wang, H. Yao, G. Zheng, Z. W. Seh, Q. Cai, W. Li, G. Zhou, C. Zu, Y. Cui, *Nat. Commun.* **2016**, *7*, 11203.

[38] W. Xu, Z. Wang, Z. Guo, Y. Liu, N. Zhou, B. Niu, Z. Shi, H. Zhang, *J. Power Sources* **2013**, *232*, 193.

[39] Y. Zhao, J. Li, Y. Ding, L. Guan, *RSC Adv.* **2011**, *1*, 852.

[40] H. Lai, J. Li, Z. Chen, Z. Huang, *ACS Appl. Mater. Interfaces* **2012**, *4*, 2325.

[41] W. Wu, Y. Zhao, C. Wu, L. Guan, *RSC Adv.* **2014**, *4*, 28636.

[42] F. Wu, J. Li, Y. Tian, Y. Su, J. Wang, W. Yang, N. Li, S. Chen, L. Bao, *Sci. Rep.* **2015**, *5*, 13340.

[43] D. Kasuya, M. Yudasaka, K. Takahashi, F. Kokai, S. Iijima, *J. Phys. Chem. B* **2002**, *106*, 4947.

[44] C. M. Yang, H. Noguchi, K. Murata, M. Yudasaka, A. Hashimoto, S. Iijima, K. Kaneko, *Adv. Mater.* **2005**, *17*, 866.

[45] T. Fujimori, K. Urita, Y. Aoki, H. Kanoh, T. Ohba, M. Yudasaka, S. Iijima, K. Kaneko, T. Agency, *Sci. Technol.* **1900**, 5.

[46] S. Bandow, F. Kokai, K. Takahashi, M. Yudasaka, L. C. Qin, S. Iijima, *Chem. Phys. Lett.* **2000**, *321*, 514.

[47] H. Dai, X. Gao, E. Liu, Y. Yang, W. Hou, L. Kang, J. Fan, X. Hu, *Diam. Relat. Mater.* **2013**, *38*, 109.

[48] D. J. Miller, M. C. Biesinger, N. S. McIntyre, *Surf. Interface Anal.* **2002**, *33*, 299.

[49] D. Wei, Y. Liu, Y. Wang, H. Zhang, L. Huang, G. Yu, *Nano Lett.* **2009**, *9*, 1752.

[50] C. Zhang, L. Fu, N. Liu, M. Liu, Y. Wang, Z. Liu, *Adv. Mater.* **2011**, *23*, 1020.

[51] C.-M. Yang, H. Noguchi, K. Murata, M. Yudasaka, A. Hashimoto, S. Iijima, K. Kaneko, *Adv. Mater.* **2005**, *17*, 866.

[52] K. Xi, S. Cao, X. Peng, C. Ducati, R. Vasant Kumar, A. K. Cheetham, *Chem. Commun.* **2013**, *49*, 2192.

[53] K. H. Wujcik, D. R. Wang, A. Raghunathan, M. Drake, T. A. Pascal, D. Prendergast, N. P. Balsara, *J. Phys. Chem. C* **2016**, *120*, 18403.

[54] M. Cuisinier, C. Hart, M. Balasubramanian, A. Garsuch, L. F. Nazar, *Adv. Energy Mater.* **2015**, *5*, 1.

[55] H. Yamin, *J. Electrochem. Soc.* **1988**, *135*, 1045.

[56] Y. V. Mikhaylik, J. R. Akridge, *J. Electrochem. Soc.* **2003**, *150*, A306.

[57] N. a. Cañas, K. Hirose, B. Pascucci, N. Wagner, K. A. Friedrich, R. Hiesgen, *Electrochim. Acta* **2013**, *97*, 42.

[58] C. Barchasz, J. C. Leprêtre, F. Alloin, S. Patoux, *J. Power Sources* **2012**, *199*, 322.

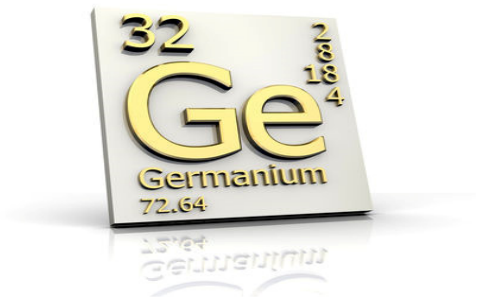

GERMANIUM ELECTRODES: EXPENSIVE BUT PROMISING FOR NICHE APPLICATIONS

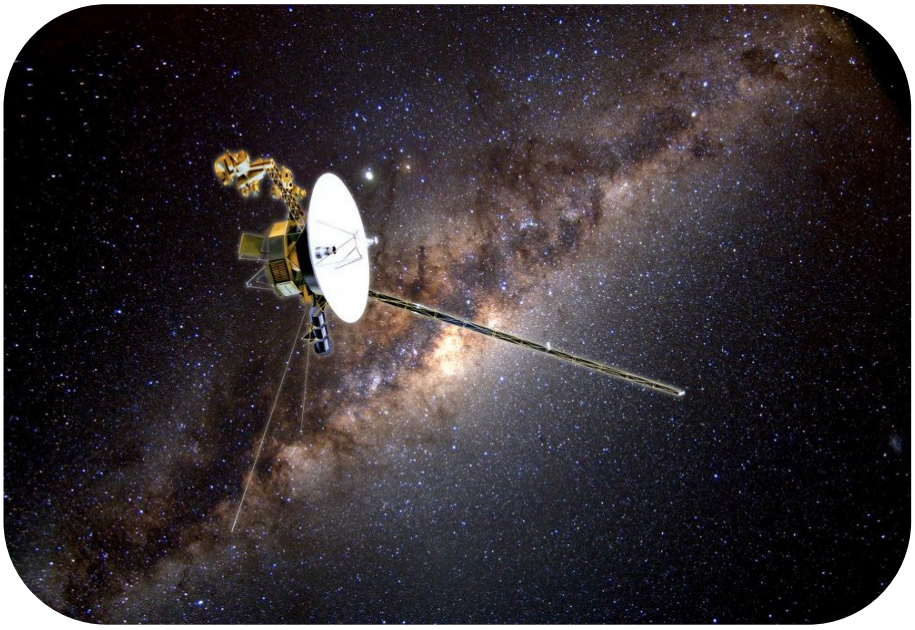

Orbiting satellite Credits https://www.nasa.gov/

3 Preferential Growth of Germanium Nanocrystals on the tips of Nitrogen Doped Single Wall Carbon Nanohorns and their Electrochemical Performance as Anode Material for Lithium ion Battery

Abstract

Tremendous efforts have been devoted to replace the existing anode material (graphite: 372 mAh/g) by group IV elements including silicon (Si), tin (Sn) and germanium (Ge). Despite the low cost and higher capacity of Si based anodes, Ge exhibits higher electronic conductivity and lithium ion diffusivity than silicon at room temperature. These properties can be exploited to provide high rated batteries for extravagant applications like medical and space technologies. Herein, we report a selective growth of Ge (5-10 nm) on the tips of single wall carbon nanohorns (SWCNHs) using a facile solvothermal method. The Ge@N-SWCNHs composite was characterized using TEM, XRD and Raman analysis and used as an anode material for lithium ion battery providing extremely high capacities of 1285 mAh/g at 0.1C after 100 cycles.

3.1 Introduction

Among various clean and renewable energy sources, lithium ion batteries (LIBs) have predominantly provided the electrical power necessary to operate existing portable electronics and hybrid electric vehicles (HEVs)[1,2]. However, demand for safe batteries with higher power and capacities have started a worldwide hunt of new electrode materials for LIBs. Many researchers from academic and industrial domains have considered Si, Ge and Sn as promising anode materials for next generation LIBs. In fact, Sony has already developed its Nexelion battery using an anode material mainly composed of a Sn/Co/C composite[3]. Main attraction of these elements lie in their high theoretical capacities (4200 mAh/g for Si, 1600 mAh/g for Ge, and 992 mAh/g for Sn) which is based on alloy reactions between the respective elements and lithium (Li_xM_y)[4]. Moreover, lower working potentials (0.1-0.6 V vs Li/Li^+) compare to insertion (TiO_2) and conversion (Fe_2O_3) materials (1.0-2.5V vs Li/Li^+) make them even more attractive for full cell configuration with higher energy densities[5].

Although Sn and Si based electrodes take the lead in terms of cost and production, Ge has also been in the spotlight due to its electronic conductivity (10^4 times higher than Si) and lithium ion diffusivity (400 times higher than Si)[6]. Contrary to silicon, isotropic lithiation of Ge allows additional structural stability during pulverization of electrode[7]. Therefore, structurally tough Ge can offer an alternative for the development of durable, high-capacity and high-rate anodes for extravagant applications like medical and space technologies[8]. Nevertheless, commercialization

of Ge based electrodes for LIB is mainly hindered by massive volumetric expansion (~250% for $Li_{15}Ge_4$), continuous breakage of SEI layer and electrochemical aggregation of Ge particles during multiple lithiation/de-lithiation[9]. The most popular approach to address these problems involves nanostructuring of Ge particles[10–13] where mechanical stress and diffusion length is minimal. Despite the reduction of particle size, Ge based anode still suffer from welding or aggregation effect during multiple lithiation/de-lithiation cycles[14]. This effect can be minimized by anchoring nanoparticles on a conductive substrates like carbon nanotubes (CNTs)[19], carbon nanofibers (CNFs)[15], graphene/reduced graphene oxide[16] (RGO) and hollow carbon encapsulating active material[17]. These carbon materials not only provide high electrical conductivity but prevent large volumetric expansion providing high power and long term stability. However, the ratio between active material (Ge NPs) and carbon has a strong influence on capacity and cycle life as higher ratios may lead to the clustering of NPs (aggregation effect).

Recent efforts to improve the electrochemical performance of Ge based anodes involved various carbon based composites. Fang et al.[18] has prepared Ge-RGO-CNTs composite comprising of 20-30 nm Ge NPs fixed tightly on the surface of RGO while using CNTs as an efficient electron transport medium. The composite could retain a specific discharge capacity of about 863.8 mAh/g after 100 cycles under a current density of 100 mA/g. Similarly, Wang et al.[19] developed a free-standing germanium/single-walled CNTs (SWCNTs) composite by trapping different amount of Ge NPs on the entangled network of CNTs. The composite with 50% Ge content gave a stable capacity of 400 mAh/g after 40 cycles at a current density of 25

mA/g. Recently, our group have developed a facile solvothermal method to anchor Ge NPs on the surface of MWCNTs. The Ge@MWCNTs composite showed improved electrochemical performance with discharge capacity of 1160 mAh/g after 60 cycles[6]. This remarkable electrochemical performance can be ascribed to the high conductive properties of MWCNTs which also prevent the aggregation of Ge nanoparticles during multiple lithiation/de-lithiation.

Despite the attractive properties of these carbon materials, higher production cost of CNTs[20] and low quality of graphene[21] limit their industrial use in many applications including lithium ion batteries. Contrarily, single wall carbon nanohorns (SWCNHs) are a kind of carbon materials that can be produced on a large scale (ton/year) using a simple arc-discharge method[22]. Typically, this exotic material exist in a clustered arrangement of horn shaped graphitic tubules (2-5 nm diameter and 40-50 nm tube length) which, upon aggregation, form dahlia-like, bud-like and seed-like structures.[23,24] Interestingly, each conical tubules have five pentagons at their tips coupled with heptagons which acts as potential reactive sites with their own distinct chemistry[25]. Moreover, local chemical reactivity is also enhanced in regions of higher curvature due to pyramidal distortion of the sp^2 carbon bonding.[26] Due to these unique and tunable properties, SWCNHs have found applications in gas storage,[27] catalysis[28] and supercapacitors.[29] Although, few reports mention their application as an anode material for lithium ion batteries,[30–32] none of them fully characterized their electrochemical performance .

In an ongoing project of understanding the potential of SWCNHs as a conductive agent for lithium and post-lithium batteries, we exploited the reactive sites of

nitrogen doped-SWCNHs by preferentially growing germanium nanocrystals (Ge NCs) onto their conical tips using oleylamine as a mild reducing agent (The choice of mild reducing agent is important as strong reducing agents cause aggregation of NPs). As prepared Ge@SWCNHs composite was used as an anode material for lithium ion battery providing high and stable capacities of 1285 mAh/g after 100 cycle. We believe that the preferential growth of Ge NCs on the tips of SWCNHs not only allow high utilization of active material but prevents the aggregation of Ge NCs after multiple cycling. These impressive results make the Ge@N-SWCNHs composite a suitable anode for LIBs to be used in high energy and high power applications.

3.2 Experimental

3.2.1 Synthesis of Ge@N-SWCNHs composites

Ge NCs and Ge@N-SWCNHs composite were prepared using a facile solvothermal approach in a 25 mL Teflon vessel. In particular, 163 mg of GeI_2 (concentration, 33 mM) was dissolved into 15 ml of degassed oleylamine. 9 mg of N-SWCNHs were subsequently added to GeI_2 solution in an inert argon atmosphere. The final mixture was transferred to a Teflon vessel equipped with a stainless steel container and kept in a furnace at 230 ^{0}C for 6 hours. Ge@N-SWCNHs composite was obtained by washing the product with 1:4 mixture of ethanol and chloroform, respectively. Finally, the obtained product was thermally treated in an argon/hydrogen (95/5%) atmosphere at 500 ^{0}C, and transferred into a glovebox to avoid surface oxidation. For

comparison, pure Ge-nanocrystals were also prepared using the same procedure without adding N-SWCNHs.

3.2.2 Material Characterization

Transmission electron microscopy images were obtained using a JEOL JEM 1011 (Jeol, Tokyo, Japan) operating at 100 kV acceleration voltage, equipped with a tungsten thermionic electron source and a FEI TECNAI G2 F20 instrument, equipped with a Schottky field emission gun (FEG), operating at 200 kV acceleration voltage. Scanning electron microscopy was carried out with a Nova 600 NanoLab microscope (FEI), equipped with a field emission gun for scanning electron imaging and a focused ion beam of gallium ions for milling. High resolution transmission electron miscopy was performed onto ultrathin carbon/holey carbon-coated Cu grids using JEM-2200FS, image Cs-corrected (Schottky emitter, HT 200 kV), with in-column imaging filter, equipped with Bruker XFlash 5060 SDD system. Raman spectroscopy measurements were carried out with Renishaw in Via Micro Raman equipped with a laser source at 633 nm through a 50x objective (LEICA N PLAN EPI 50/ 0.75). XRD patterns were collected on a PANalytical Empyrean X-ray diffractometer equipped with a 1.8 kW CuKα ceramic X-ray tube, PIXcel3D 2 x 2 area detector and operating at 45 kV and 40 mA. XPS analysis was per-formed on a Kratos Axis Ultra DLD spectrometer, using a monochromatic Al Kα source (15 kV, 20 mA). High resolution narrow scans were performed at constant pass energy of 20 eV and steps of 0.1 eV. The photoelectrons were detected at a takeoff angle $\theta = 0°$ with respect to the surface normal. The pressure in the analysis chamber was maintained below 7×10^{-9} Torr for data acquisition. The data were converted to

VAMAS format and pro-cessed using Casa XPS software, version 2.3.16. The binding energy (BE) scale was internally referenced to the C 1s peak (BE for C–C = 284.8 eV).

3.2.3 Electrochemical Characterization

The electro-chemical performance of as-prepared Ge@N-SWCNHs composite was tested using CR2032 coin cells which consist of lithium chips (15.6 Dia x 0.45t mm; MTI Corporations) as reference and counter electrode, dried glass fibers membrane (What-man GF/D) as separator and Ge@N-SWCNHs composite, casted on a copper substrate, as working electrode. Slurries casted on copper foil (15 mm Dia) were composed of 70% weight Ge NCs or Ge@N-SWCNHs composite (containing 80% Germanium), 20% super-P carbon and 10% polyvinylidene difluoride (PVDF) mixed with an appropriate amount of N-methyl-2-pyrrolidone. The casted electrodes were dried overnight at 60 °C under vacuum and the mass loadings of active material were found in the range of 1-1.2 mg. 250 μL of electrolyte was used in each coin cell which contain 1 M lithium hexafluorophosphate ($LiPF_6$) dissolved in 1:1 mixture of ethylene carbonate (EC) and dimethyl carbonate (DMC), respectively. 5% (v/v) vinylene carbonate (VC) was also used as an additive. After their assembling inside a MBraun glovebox, with H_2O and O_2 levels below 0.1 ppm, all cells were electrochemically tested using BioLogic BCS-805 multichannel battery unit controlled by BT Lab V1.30. Impedance analyses were performed using the same instrument in the frequency range of 10 kHz to 100 mHz with a voltage amplitude of 5 mV.

3.3 Result and discussion

3.3.1 Synthesis and Characterization of Ge@N-SWCNHs

Solution phase synthesis of Ge NPs is mainly based on employing a strong reducing agents like alkali metals or organoalkali reagents.[34–36] However, one-pot heat up methods can also be used to synthesize crystalline Ge NCs where chemicals like oleylamine not only act as a solvent but also a mild reducing agent[37] to grown Ge NCs on the tips of N-SWCNHs. Our method depicted in **Figure 2.1a** utilizes thisproperty of single wall carbon nanohorns to provide reactive site for the growth of Ge NCs. This unique nano-structured Ge@N-SWCNHs composite not only provides void space to accommodate volume changes, but suggested to prevent aggregation of Ge NCs during charge/discharge process.

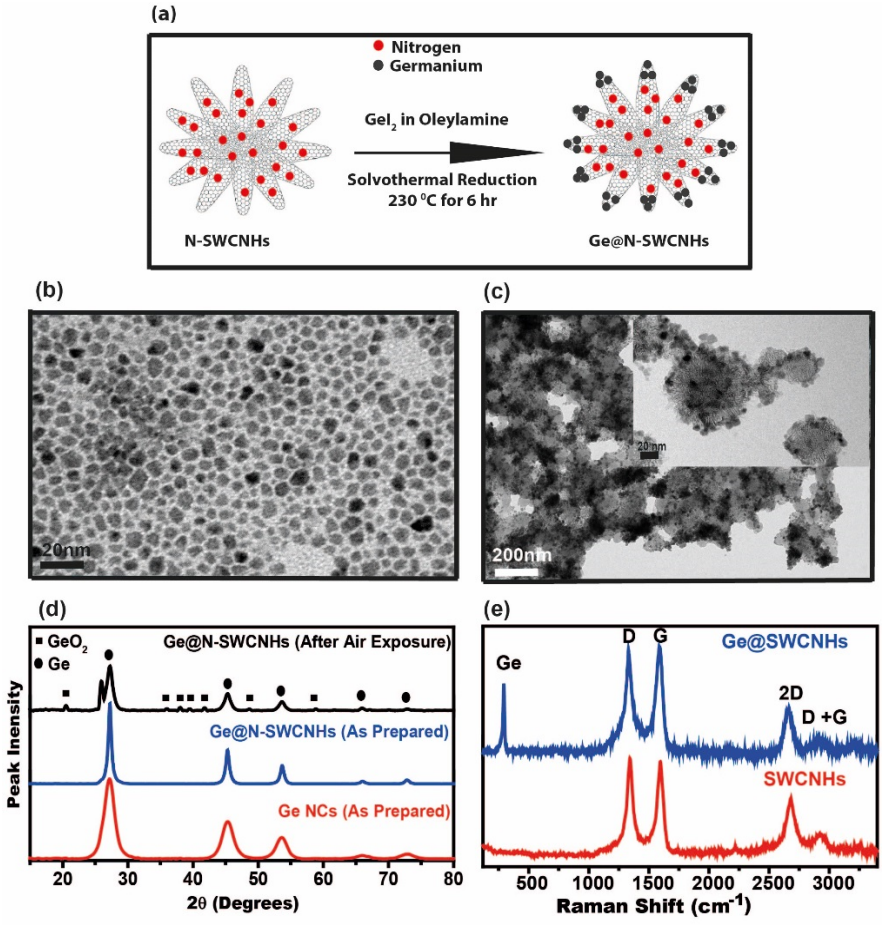

Figure 3.1: Schematics of the synthetic protocol of Ge@N-SWCNHs composite

Transmission electron microscopic (TEM) analysis of as prepared Ge NCs and Ge@N-SWCNHs composite was performed to understand the morphology of NCs and their distribution over the surface of N-SWCNHs. Our TEM results show 4-10 nm Ge NCs intrinsically capable of sustaining large volumetric expansion.(**Figure 3.1b**) In case of Ge@N-SWCNHs, we observed the preferential arrangement of Ge NCs at the conical tips of N-SWCNHs.(**Figure 3.1c**) We believe that the preferential

growth is the result of enhance reactivity of conical tips of N-SWCNHs due to the heptagons[25] providing a nucleation site of Ge NCs to grow.[26]

Crystallinity of Ge NCs and Ge@N-SWCNHs composite was confirmed using X-ray diffraction (XRD) analysis **(Figure 3.1d)**. In particular,. XRD spectra of freshly prepared Ge NCs and Ge@N-SWCNHs composite show characteristic peaks of cubic germanium at 2θ values of 27.32°, 45.22°, 53.76°, 65.92° and 72.83° (JCPDS card No. 03-065-0333)[15,38]. The average particle size of Ge NCs obtained using Scherrer equation was found to be 8.5 nm matching well with our TEM observations. However, small fraction of Ge NCs were converted to GeO_2 by exposing Ge@N-SWCNHs to air **(Figure 3.1d)**. Exposed samples were also analyzed using high resolution transmission electron microscopy which showed two different kind of particles on the edges of N-SWCNHs confirming partial oxidation of Ge NCs. (**Figure 3.2**)

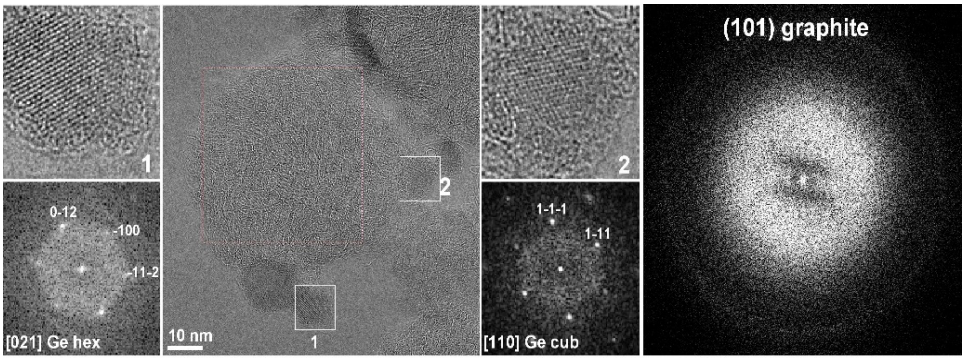

Figure 3.2 HRTEM images of Ge@N-SWCNHs showing two kinds of particles including cubic germanium and hexagonal GeO_2.

Detailed characterization of N-SWCNHs and Ge@N-SWCNHs composite was performed using raman spectroscopy. **Figure 3.1e** shows two prominent peaks associated to the D and G bands where the former is attributed to disordered sp^2 carbon while the latter is related to the vibrational modes of graphitic carbons[39]. Due to the topological defects of pentagons and heptagons in N-SWCNHs, these D and G peaks appears at 1348 and 1590 cm^{-1}, respectively[40]. Additional peaks at 2953 cm^{-1} (2D) and 3225 cm^{-1} (D+G) are the overtones of D and G peaks, respectively[41]. I_D/I_G ratios calculated for both spectra showed values close to unity, explaining the defected structure associated to N-SWCNHs[40]. Finally, the peak of Ge appear close to 300 cm^{-1} demonstrating its presence in Ge@N-SWCNHs composites

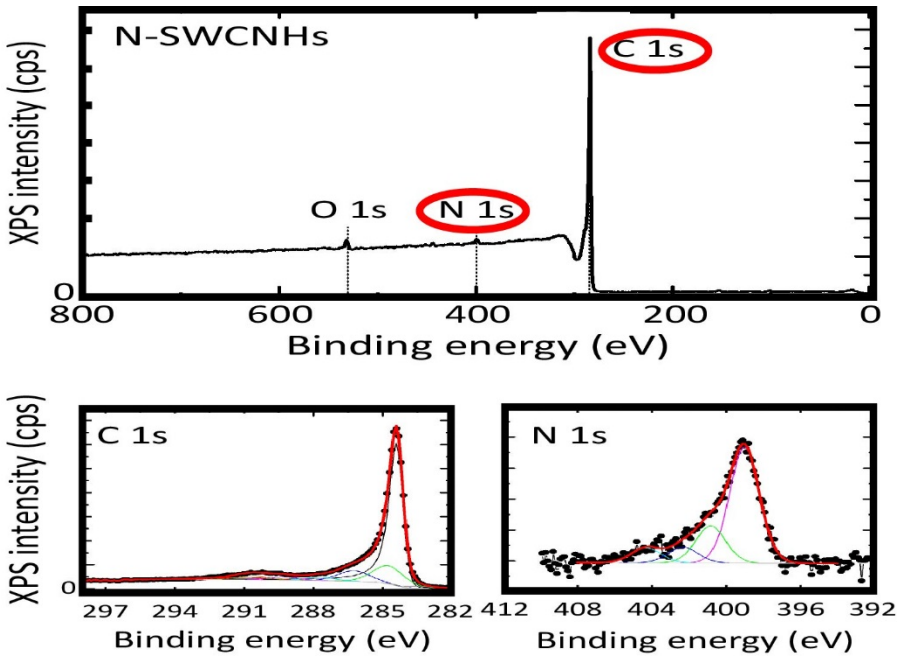

Figure 3.3. XPS analysis of N-SWCNHs with a magnified regions of N1s and C1s

To confirm the presence of nitrogen doping and surface chemical properties X-ray Photoelectron Spectroscopy (XPS) was performed on N-SWCNHs. **Figure 3-3a** shows the XPS spectrum of N-SWCNHs depicting C 1s, N 1s and O 1s peaks. The C 1s peak **(Figure 3-2c)** shows the typical shape related to graphitic-like compounds[42] given by an asymmetric peak centered at 284.4±0.2 eV (corresponding to sp^2-hybridized carbon atoms) accompanied by a low intensity shake-up feature at 290.8±0.2 eV, related to $\pi \rightarrow \pi^*$ transition. The best fit of the C 1s profile has been obtained by adding other low intensity peaks, ascribable to adventitious carbon species[43] (peaks centered at 284.9±0.2 eV, 286.4±0.2 eV, 288.0±0.2 eV and 289.7±0.2 eV, assigned respectively to sp^3-hybridized carbon atoms, C-O, C=O and O-C=O species). However, the peak at 286.4±0.2 eV can also be associated to C-N species, corresponding to the N-sp^2 C bonds originated from the inclusion of N atoms in the carbon network of the nanohorns[44]. This assignment is supported by the presence of the N 1s broad peak appearing between 396 and 406 eV **(Figure 3-2d)** which could be decomposed into three components centered at 399.0±0.2 eV, 400.8±0.2 eV, and 402.2±0.2 eV, corresponding to pyridinic, pyrrolic, and graphitic nitrogen, respectively[45]. The atomic percentage of carbon, nitrogen and oxygen were found to be 97.8, 1.1 and 1.1%, respectively **(Figure 3-2a)**.

3.3.2 Electrochemical Performance of Ge@N-SWCNHs

Use of electrolyte additives is the most economic method for improving the performance of lithium ion batteries. They are known to facilitate the formation of mechanically stable solid electrolyte interface (SEI) which acts as a passivating layer to inhibit further electrolyte reduction[46]. Vinylene carbonate (VC) and

fluoroethylene carbonate (FEC) are the most common electrolyte additives used to improve the stability of SEI in Si, Ge and Sn based anode materials[47]. **Figure 3.3** show different voltammograms of SWCNHs, Ge NCs and Ge@N-SWCNHs composite in the potential range between 2.5 and 0.005 V vs. Li^+/Li at a scan rate of 0.2 mV/s. For comparison, initial tests performed on N-SWCNHs using base electrolyte (1M $LiPF_6$ in EC:DMC) showed two prominent peaks at 0.61V (disappeared after 1st cycle) and 0.005 V (**Figure 3.3a Inset**). Peak at 0.61V can be associated to the reductive decomposition of EC while the peak at 0.005V can be ascribed to adsorption/intercalation of lithium inside N-SWCNHs[31]. During anodic scan, peak at 0.21V describes the de-intercalation of lithium from N-SWCNHs. The low intensity of anodic peak compare to its cathodic counterpart suggests the irreversible intercalation/de-intercalation of N-SWCNHs which might explains the lower columbic efficiency of Ge@N-SWCNHs at low C-rates (described later). Cyclic voltammetry performed on Ge NCs based electrodes showed a first cycle reduction peak at 0.75V which can be ascribed to the decomposition of EC (**Figure 3.3 b**). Besides, additional reduction peaks from 0.31 to 0.05V describe lithium insertion into equipotential sites and the formation of Ge-alloys, i.e. Li_9Ge_4 and Li_7Ge_4 followed by $Li_{15}Ge_4$ and $Li_{22}Ge_4$[10,12,38,49] Similar behavior was observed for electrodes made from Ge@N-SWCNHs composites in the base electrolyte of EC:DMC. **(Figure 3.3c)**

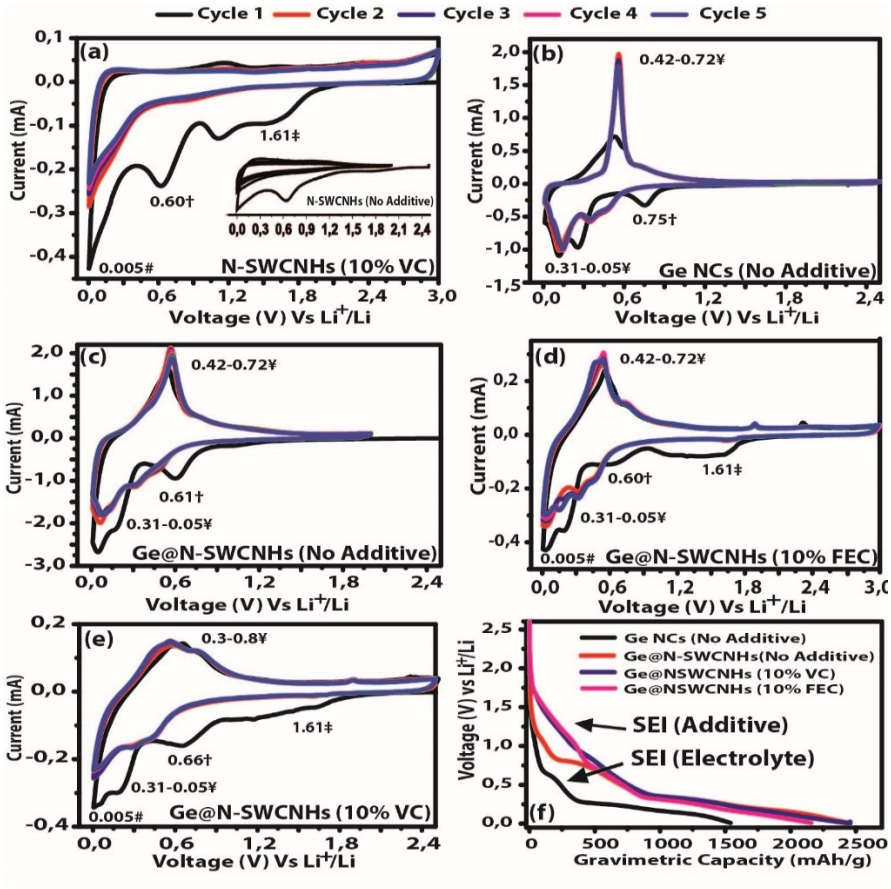

Figure 3.4 Cyclic voltammograms of a) N-SWCNHs with 10% VC, b) Ge NCs without additives, c)Ge@N-SWCNHs without additives, d) Ge@N-SWCNHs with 10% FEC, e) Ge@N-SWCNHs with 10% VC and e) Discharge profiles of Ge NCs and Ge@N-SWCNHs with different additives. ‡ represents SEI peaks related to additives (VC or FEC),† represents SEI peaks related to electrolyte decomposition, # represent peaks related to adsorption/intercalation of lithium inside N-SWCNHs while ¥ represents the region of various peaks related to lithium intercalation inside Germanium.

However to understand the effect of electrolyte additive including VC and FEC, same experiments were performed by adding VC (10% v/v) into the base electrolyte. In

case of N-SWCNHs, a broad peak appeared at 1.61V which can associated to the decomposition of VC. (**Figure 3.3a**). The same peak appeared in case Ge@N-SWCNHs composite suggesting similar decomposition of VC at higher potentials **(Figure 3.3e)**[48]. After changing the electrolyte additive from VC to FEC, a broad hump was observed ranging from 1.61 to 1.2 V. This additional broad peak suggests the decomposition of FEC into lithium fluoride (LiF) and polyvinylene carbonate (polyVC)[48] **(Figure 3.3d)** Interestingly, peaks at 0.61V (related to the decomposition of EC) were suppressed in the presence of electrolyte additives, however, the effect of FEC was more pronounced than VC[46]**(Figure 3.3d and e).** Similar behavior was observed at the first lithiation cycle of chronopotentiometric curves where Ge@N-SWCNHs composite, in the absence of electrolyte additives, showed a prominent shoulder at 0.61 V which was suppressed by the addition of electrolyte additives (**Figure 3.3f**) Finally, the anodic (de-lithiation) scan of the Ge NCs and Ge–N-SWCNHs composite shows oxidative peaks, located in the range of 0.42-0.72V.suggesting de-alloying process of Ge–Li composites (**Figure 3.3 b, c, d and e**).

In order to avoid the irreversibility cause by N-SWCNHs, galvanostatic charge discharge measurements were performed in the potential range of 1.5 and 0.01 V vs. Li^+/Li at 0.1C. **Figure 3.4 a** compare the charge discharge profile of Ge NCs and Ge@N-SWCNHs composite in the presence of VC additive at 0.1C (1C =1600 mAh/g). Indeed the initial lithiation gravimetric capacities achieved for Ge@N-SWCNHs composites (2549 mAh/g) are higher than Ge NCs (1495 mAh/g), however, after 5 cycles these capacities stabilized to 1435 and 1046 mAh/g,

respectively. Moreover, the voltage profile of Ge@N-SWCNHs appeared at lower activation potentials compare to the voltage profiles of Ge NCs (**Figure 3.4a**). We believe that higher capacities obtained for Ge@N-SWCNHs composites are associated to the lower activation energies allowing complete utilization of active material in a given potential range of 0.01-1.5V. Moreover, the comparison between 5^{th} and 100^{th} charge discharge profile of Ge@N-SWCNHs show minimal activation barrier and the loss of capacity is mainly due to the concentration overpotential created at the electrode surface (**Figure 3.4b**) Finally, the capacity retention of pristine Ge NCs and Ge@N-SWCNHs composite in the presence of VC was tested for over 100 cycles (**Figure 3.4c,d**).

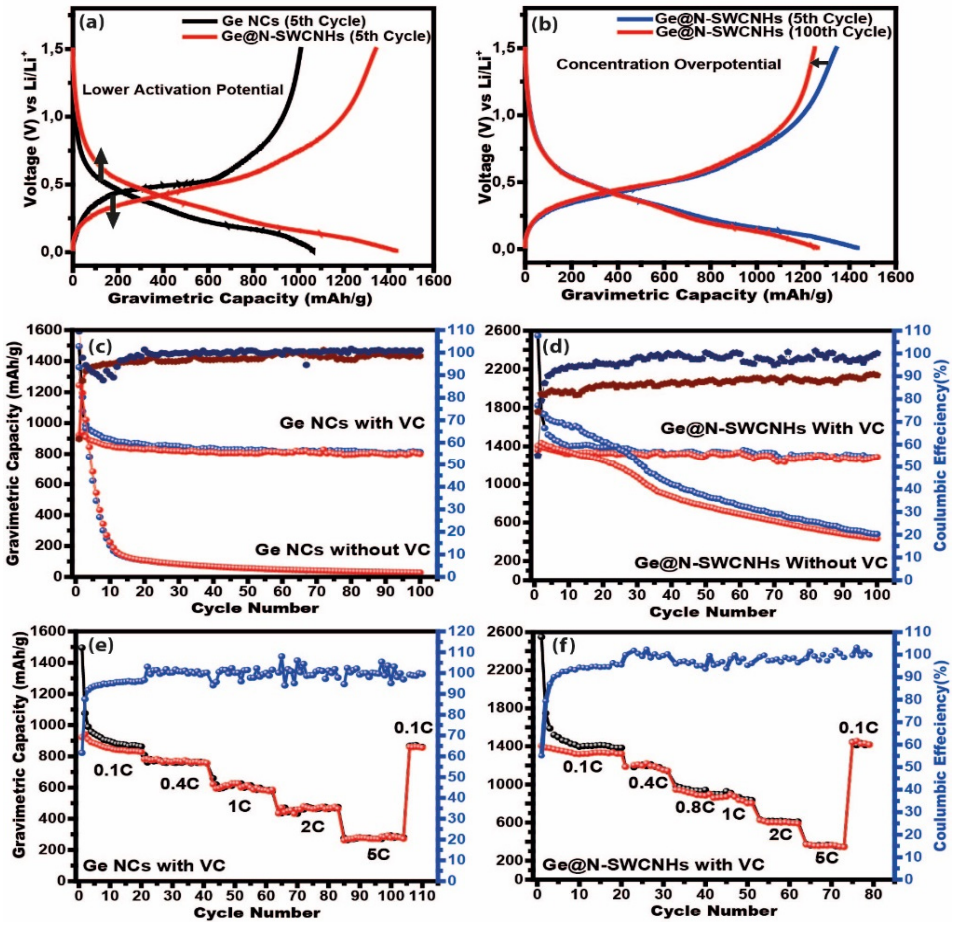

Figure 3.5. a) Comparison for the 5th cycle charge discharge curves of Ge NC and Ge@N-SWCNHs . b) Charge discharge profiles of the 5th and 100th cycles for Ge@N-SWCNHs composite. Cycling performance of c) Ge NCs and d) Ge@N-SWCNHs composite with and without VC at 0.1C. Rate performance of e) Ge NCs and f) Ge@N-SWCNHs

Pristine Ge NCs and Ge@N-SWCNHs composites show initial discharge capacities of 1495 and 2549 mAh/g which stabilized at 811 and 1285 mAh/g after 100 cycles, respectively. It is interesting and important to notice that the majority of the de-lithiation capacity in Ge@N-SWCNHs composite was lost during the first 10 cycles

(6 %) while only 2.5 % loss was observed for the remaining 90 cycles. Similar results have been obtained for Ge@N-SWCNHs composite in FEC based electrolytes, however, detailed understanding on the effect of FEC is still under investigation. On the other hand, electrodes operated in VC or FEC free electrolytes show a rapid decay of capacities due to unstable SEI formation. The remarkable storage capacities observed for Ge@N-SWCNHs using VC or FEC as an electrolyte additive were comparatively higher to our previously reported method where carbon nanotubes were used a conductive host for Ge NCs[6] Therefore, these results suggest an intimate contact between Ge nanocrystals and N-SWCNHs allowing high utilization of the active material.

Table 3.1: Comparison of the performance metrics between Ge @N-SWCNHs and other carbon based Ge composites

Ge Composites	Synthetic route	Capacities (mAh/g)	Current Densities (mA/g)	Cycles	Ref
Ge-C	Magnetic sputtering coupled with plasma reactors	980	2000	100	[50]
Ge-N-RGO	Hydrolysis to GeO2 and annealed back to Ge	700	5000	200	[51]
Ge-RGO	Colloidal synthesis in inert conditions	1350	1600	600	[52]
Ge-RGO-CNT	Colloidal method in inert condition	863.8	100	100	[18]
Ge-C	Hydrolysis followed by annealing	1232	C/2	1000	[10]
Ge-CNT paper	Hydrolysis to GeO2	417	25	40	[19]

Ge-hollow carbon	Hydrolysis to GeO2	1000	C/10	100	[12]
Ge-MWCNTs	Solvothermal	1060	160	60	[6]
Ge@N-SWCNHs	Solvothermal	1285	120	100	This work

The rate performance of Ge NCs and Ge@SWCNHs composite was analyzed at different charge discharge rates Ge@N-SWCNHs composite based electrodes showed de-lithiation capacities of 1420, 1193, 935, 866, 611, 366 mAh/g at 0.1C, 0.4C, 0.8C, 1C, 2C and 5C. respectively(**Figure 3.4e**). Superior performance of Ge@N-SWCNHs composite can be realized by the fact that electrode material regained its original capacity of 1413 mAh/g after been cycled at high scan rates. On the other hand, Ge NCs show de-lithiation capacities of 908, 762, 599, 462, and 271 mAh/g at 0.1C, 0.4C, 1C, 2C and 5C. respectively while regained the capacity of 850 mAh/g at 0.1C. The comparison of Ge@N-SWCNHs composite with recently reported Ge-carbon composites (**shown in table 1**) suggest its suitability as an active material for applications in high energy and high power LIBs. Moreover, large scale and cost effective production of industrial grade N-SWCNHs along with as-reported performance of Ge@N-SWCNHs composite provide this electrode material an edge over graphene and carbon nanotube based composites.

3.4 Conclusion

We have reported a facile solvothermal synthesis of 5-10 nm germanium nanocrystal decorated on the tips of nitrogen doped single wall carbon nanohorns. As-prepared

Ge@N-SWCNHs composites were electrochemical tested as an anode material for lithium ion battery showing remarkable capacities of 1285 mAh/g after 100 cycles. Moreover, the electrochemical performance of Ge@N-SWCNHs composites was compared with bare Ge-NC with and without electrolyte additives. Our results suggests that Ge@N-SWCNHs show superior presentence in the presence of electrolyte additive VC and FEC due to the formation of stable SEI. We also believe that N-SWCNHs are attractive carbon materials for achieving high theoretical capacities and their low cost production give them an advantage over carbon nanotubes and graphene.

3.5 References

[1] U. Gulzar, S. Goriparti, E. Miele, T. Li, G. Maidecchi, A. Toma, F. De Angelis, C. Capiglia, R. P. Zaccaria, *J. Mater. Chem. A* **2016**, *4*, 16771.

[2] S. Goriparti, E. Miele, F. De Angelis, E. Di Fabrizio, R. Proietti Zaccaria, C. Capiglia, *J. Power Sources* **2014**, *257*, 421.

[3] A. N. Dey, *J. Electrochem. Soc.* **1971**, *118*, 1547.

[4] H. Tian, F. Xin, X. Wang, W. He, W. Han, *J. Mater.* **2015**, *1*, 153.

[5] D. Liu, Z. Liu, X. Li, W. Xie, Q. Wang, Q. Liu, Y. Fu, D. He, *Small* **2017**, *1702000*, 1.

[6] S. Goriparti, U. Gulzar, E. Miele, F. Palazon, A. Scarpellini, S. Marras, S. Monaco, R. Proietti Zaccaria, C. Capiglia, *J. Mater. Chem. A* **2017**, *5*, 1.

[7] H. Yang, S. Huang, X. Huang, F. Fan, W. Liang, X. H. Liu, L. Q. Chen, J. Y. Huang, J. Li, T. Zhu, S. Zhang, *Nano Lett.* **2012**, *12*, 1953.

[8] W. Liang, H. Yang, F. Fan, Y. Liu, X. H. Liu, J. Y. Huang, T. Zhu, S. Zhang, *ACS Nano* **2013**, *7*, 3427.

[9] S. Yoon, C.-M. Park, H.-J. Sohn, *Electrochem. Solid-State Lett.* **2008**, *11*, A42.

[10] D. T. Ngo, R. S. Kalubarme, H. T. T. Le, J. G. Fisher, C. N. Park, I. D. Kim, C. J. Park, *Adv. Funct. Mater.* **2014**, *24*, 5291.

[11] C. K. Chan, X. F. Zhang, Y. Cui, *Nano Lett.* **2008**, *8*, 307.

[12] D. Li, C. Feng, H. kun Liu, Z. Guo, *J. Mater. Chem. A* **2015**, *3*, 978.

[13] Y. Liu, X. H. Liu, B.-M. Nguyen, J. Yoo, J. P. Sullivan, S. T. Picraux, J. Y. Huang, S. A. Dayeh, *Nano Lett.* **2013**, *13*, 4876.

[14] Z. Hu, S. Zhang, C. Zhang, G. Cui, *Coord. Chem. Rev.* **2016**, *326*, 34.

[15] T. Wang, G. Xie, J. Zhu, B. Lu, *Electrochim. Acta* **2015**, *186*, 64.

[16] H. Li, L. Shi, W. Lu, X. Huang, L. Chen, *J. Electrochem. Soc.* **2001**, *148*, A915.

[17] D. Li, C. Feng, H. kun Liu, Z. Guo, *J. Mater. Chem. A* **2015**, *3*, 978.

[18] S. Fang, L. Shen, H. Zheng, X. Zhang, *J. Mater. Chem. A* **2015**, *3*, 1498.

[19] J. Wang, J. Z. Wang, Z. Q. Sun, X. W. Gao, C. Zhong, S. L. Chou, H. K. Liu, *J. Mater. Chem. A* **2014**, *2*, 4613.

[20] C. Wu, M. A. Nahil, -->Norbert -->Miskolczi, J. Huang, P. T. Williams, *Process Saf. Environ. Prot.* **2016**, *103*, 107.

[21] B. Zhang, J. Song, G. Yang, B. Han, *Chem. Sci.* **2014**, *5*, 4656.

[22] H. Wang, M. Chhowalla, N. Sano, S. Jia, G. A. J. Amaratunga, *Nanotechnology* **2004**, *15*, 546.

[23] S. Iijima, M. Yudasaka, R. Yamada, S. Bandow, K. Suenaga, F. Kokai, K. Takahashi, *Chem. Phys. Lett.* **1999**, *309*, 165.

[24] S. Iijima, T. Ichihashi, *Nature* **1993**, *363*, 603.

[25] D. P. Hashim, N. T. Narayanan, J. M. Romo-Herrera, D. A. Cullen, M. G. Hahm, P. Lezzi, J. R. Suttle, D. Kelkhoff, E. Muñoz-Sandoval, S. Ganguli, A. K. Roy, D. J. Smith, R. Vajtai, B. G. Sumpter, V. Meunier, H. Terrones, M. Terrones, P. M. Ajayan, *Sci. Rep.* **2012**, *2*, 363.

[26] S. Park, D. Srivastava, K. Cho, *Nano Lett.* **2003**, *3*, 1273.

[27] Y. Liu, C. M. Brown, D. A. Neumann, D. B. Geohegan, A. A. Puretzky, C. M. Rouleau, H. Hu, D. Styers-Barnett, P. O. Krasnov, B. I. Yakobson, *Carbon N. Y.* **2012**, *50*, 4953.

[28] J. Adelene Nisha, M. Yudasaka, S. Bandow, F. Kokai, K. Takahashi, S. Iijima, *Chem. Phys. Lett.* **2000**, *328*, 381.

[29] A. Izadi-Najafabadi, T. Yamada, D. N. Futaba, M. Yudasaka, H. Takagi, H. Hatori, S. Iijima, K. Hata, *ACS Nano* **2011**, *5*, 811.

[30] W. Xu, Z. Wang, Z. Guo, Y. Liu, N. Zhou, B. Niu, Z. Shi, H. Zhang, *J. Power Sources* **2013**, *232*, 193.

[31] Y. Zhao, J. Li, Y. Ding, L. Guan, *RSC Adv.* **2011**, *1*, 852.

[32] H. Lai, J. Li, Z. Chen, Z. Huang, *ACS Appl. Mater. Interfaces* **2012**, *4*, 2325.

[33] B. Wang, B. Luo, X. Li, L. Zhi, *Mater. Today* **2012**, *15*, 544.

[34] A. Kornowski, M. Giersig, R. Vogel, A. Chemseddine, H. Weller, *Adv. Mater.* **1993**, *5*, 634.

[35] H. W. Chiu, C. N. Chervin, S. M. Kauzlarich, *Chem. Mater.* **2005**, *17*, 4858.

[36] H. W. Chiu, S. M. Kauzlarich, *Chem. Mater.* **2006**, *18*, 1023.

[37] S. Mourdikoudis, L. M. Liz-Marzán, *Chem. Mater.* **2013**, *25*, 1465.

[38] S. Fang, L. Shen, H. Zheng, Z. Tong, G. Pang, X. Zhang, *RSC Adv.* **2015**, *5*, 85256.

[39] C. M. Yang, H. Noguchi, K. Murata, M. Yudasaka, A. Hashimoto, S. Iijima, K. Kaneko, *Adv. Mater.* **2005**, *17*, 866.

[40] T. Fujimori, K. Urita, Y. Aoki, H. Kanoh, T. Ohba, M. Yudasaka, S. Iijima, K. Kaneko, T. Agency, *Sci. Technol.* **1900**, 5.

[41] A. C. Ferrari, D. M. Basko, *Nat. Publ. Gr.* **2013**, *8*, 235.

[42] H. Dai, X. Gao, E. Liu, Y. Yang, W. Hou, L. Kang, J. Fan, X. Hu, *Diam. Relat. Mater.* **2013**, *38*, 109.

[43] D. J. Miller, M. C. Biesinger, N. S. McIntyre, *Surf. Interface Anal.* **2002**, *33*, 299.

[44] D. Wei, Y. Liu, Y. Wang, H. Zhang, L. Huang, G. Yu, *Nano Lett.* **2009**, *9*, 1752.

[45] C. Zhang, L. Fu, N. Liu, M. Liu, Y. Wang, Z. Liu, *Adv. Mater.* **2011**, *23*, 1020.

[46] S. S. Zhang, *J. Power Sources* **2006**, *162*, 1379.

[47] A. L. Michan, B. S. Parimalam, M. Leskes, R. N. Kerber, T. Yoon, C. P. Grey, B. L. Lucht, *Chem. Mater.* **2016**, *28*, 8149.

[48] M. Nie, J. Demeaux, B. T. Young, D. R. Heskett, Y. Chen, A. Bose, J. C. Woicik, B. L. Lucht, *J. Electrochem. Soc.* **2015**, *162*, A7008.

[49] H. Jung, P. K. Allan, Y. Y. Hu, O. J. Borkiewicz, X. L. Wang, W. Q. Han, L. S. Du, C. J. Pickard, P. J. Chupas, K. W. Chapman, A. J. Morris, C. P. Grey, *Chem. Mater.* **2015**, *27*, 1031.

[50] W. Li, J. Zheng, T. Chen, T. Wang, X. Wang, X. Li, *Chem. Commun. (Camb).* **2014**, *50*, 2052.

[51] Y. Xu, X. Zhu, X. Zhou, X. Liu, Y. Liu, Z. Dai, J. Bao, **2014**.

[52] F. W. Yuan, H. Y. Tuan, *Chem. Mater.* **2014**, *26*, 2172.

SN BASED ELECTRODES: CHEAP BUT CHALLENGING

Beta Tin converting into alpha tin at low temperatures. Credits: periodic table.com

4 Facile Synthesis of Nitrogen Doped Single Wall Carbon Nanohorns Based Tin Composite as Anode Material for Lithium ion Battery

Abstract

Due to limited capacity provided by the existing graphite anode (372 mAh/g) group IV elements including silicon (Si), tin (Sn) and germanium (Ge) are highly sought after materials for next generation lithium ion batteries. Among them, tin (Sn) based electrodes are the most attractive candidates due to their high conductivity and low cost. Moreover, upon lithiation, Sn based electrodes show moderate volumetric expansion as compare to Ge and Si. Herein, we report a simple synthetic route for preparing Sn nanocrystals (NCs) (size:10-30 nm) on the surface of nitrogen doped single wall carbon nanohorns (N-SWCNHs) using a strong and easy to prepare reducing agent (lithium naphthalenide). As-prepared Sn@N-SWCNHs composite was characterized using TEM, XRD, Raman analysis and used as an anode material for lithium ion battery providing high gravimetric capacities of 795 mAh/g at 0.1C after 140 cycles. Cells tested for long term stability provided 375 mAh/g at 1C for 1000 cycles.

4.1 Introduction

Besides germanium, tin (Sn) has also received a considerable attention due to its higher theoretical capacity (992 mAh/g for $Li_{22}Sn_5$)[1]. Although, the cheap and abundant nature of tin makes it an attractive candidate as anode material, the commercial use of Sn based electrodes is still hindered due to many technological challenges. Similar to Ge and Si, one of the critical issues is related to severe capacity fading during the insertion and extraction of lithium ions, which mainly results from the pulverization of active material caused by the huge volumetric expansion[2]. Therefore, elaborately tailoring the structure of Sn-based materials to effectively accommodate the volumetric expansion is one of the critical challenge for the scientific community. Extensive efforts have been made to improve the electrochemical behavior of Sn anodes using various approaches including (1) reducing Sn particle size (<50 nm) to efficiently mitigate the absolute strain induced by the large volume change during lithiation/de-lithiation; (2) uniformly dispersing nano-Sn inside a conductive matrix (such as carbon) to accommodate volume change and maintain the mechanical integrity of the composite electrode.

Both strategies have been extensively used for the improvement of Sn based electrodes. For example, Scrosati et al.[3] developed a novel method of synthesizing Sn particles (~ 30 nm) embedded in carbon matrix. The composite provided gravimetric capacity of 500 mAh/g for several hundred cycles and allowed cycling at 5C recovering 40% of its total capacity. Later, the same group reported a full cell using Sn/C composite anode coupled with $Li[Ni_{0.45}Co_{0.1}Mn_{1.45}]O_4$ spinel cathode

providing capacities of 105 mAh/g at 5C.[4] Recently, Xu et al.[5] used a facile aerosol spray pyrolysis technique to synthesize nano-Sn/C spherical composites (size: 10 nm). They were able to achieve high capacities up to 710 mAh/g after 130 cycles at 0.25 C while ~600 mAh/g at 20 C. Same group previously reported a novel sponge like porous Sn/C composites giving capacity of 1300 mAh/g after 450 cycles. Reported capacities (higher than theoretical values) were attributed to the reversible formation/ decomposition of the gel-like polymers formed on the mesoporous Sn/C composite.[6]. Moreover, different structural dimensionalities (0D[6,7], 1D[8], 2D[9], 3D[10]) of Sn have also been explored as an anode materials with different carbon materials including graphene and carbon nanotubes.[11]

After achieving remarkable capacities using Ge@N-SWCNHs composite as anode material, we switched to tin as a less expensive anode material and developed a facile room temperature synthetic route for preparing Sn@N-SWCNHs composite. The method utilized an easily prepared reducing agent (lithium naphthalenide) to reduce Sn NCs on the surface of N-SWCNHs. As prepared material was electrochemical tested as an anode material for lithium ion battery which provided high gravimetric capacity of 795 mAh/g after 140 cycles at 0.1C. This enhance utilization of capacity is attributed to the porous structure of Nitrogen doped single wall carbon nanohorns which not only provide a conductive substrate but limit the aggregation process during multiple cycling.

4.2 Experimental

4.2.1 Synthesis of Sn@N-SWCNHs composites

Synthesis of Sn@N-SWCNHs was carried out by reducing $SnCl_2$ using lithium naphthalenide (Li-Nap) at room temperature. Initially, Li-Nap was prepared by adding equal moles (20 m-mol) of naphthalene (Sigma Aldrich) and lithium metal (battery grade) in 10 mL of 1,2 dimethoxyethane. The solution turned into dark green color which was kept on constant stirring for 12 hrs. In a separate vial, 189 mg of $SnCl_2$ was dissolved in 5 mL of anhydrous N-methyl-2-pyrrolidone followed by the addition of 18 mg of N-SWCNHs. Later, 2mL of as-prepared Li-Nap solution was added to the mixture of as-prepared $SnCl_2$ and N-SWCNHs at room temperature. The mixtures changed its color to darkish black indicating the presence of Sn nanoparticles. Final product was subsequently washed with anhydrous toluene and methanol to remove naphthalene and lithium chloride. All experiments were performed in an argon filled glove box with water and oxygen levels below 0.1ppm. Li-NAP stock solution remained stable even after 6 months inside an argon filled glovebox. For comparison bare Sn NCs were prepared using the same procedure without adding N-SWCNHs

4.2.2 Material Characterization

Sn@N-SWCNHs composite was characterized using transmission electron microscopy (TEM), X-ray diffraction (XRD) analysis, Raman and X-ray

photoelectron spectroscopy (XPS). Details can be found in the experimental section of Chapter III.

4.2.3 Electrochemical Characterization

The electro-chemical performance of as-prepared Sn@N-SWCNHs composite are similar to the procedure described in chapter III, however, electrode slurries were composed of 70% w/w Sn@N-SWCNHs (containing 90% Sn), 20% super-P carbon and 10% polyvinylidene difluoride (PVDF) mixed with an appropriate amount of N-methyl-2-pyrrolidone. Moreover, 10% (v/v) fluoroethylene carbonate (FEC) was also used as an electrolyte additive.

4.3 Result and discussion

4.3.1 Synthesis and Characterization of Ge@N-SWCNHs

Solution phase synthesis of Sn NPs is mainly based on employing a strong reducing agents[9] like $LiAlH_4$ and $NaBH_4$ at room temperatures. Lithium naphthalenide (Li-NAP) is another powerful but less explored reducing agent with formal potentials of 3.10V in tetrahydrofuran (THF). Few solvents including glymes, THF and ethers can be used to prepare Li-NAP as most of the solvents react with naphthalenide anion compromising its reducing properties[12] In addition to its simple preparation method, the reaction byproducts of Li-NAP such as naphthalene and dihydronaphthalene can be easily removed using simple organic solvents allowing oxide free synthesis of Sn nanoparticles. Our synthetic protocol shown in **figure 4.1a**

utilized Li-NAP to reduce halide salts of Sn to produce nanocrystals in the range of 10-30 nm decorated on the surface of N-SWCNHs (**Figure 4.1b, c**). The selection of N-SWCNHs as a conductive substrate for Sn nanocrystals was motivated by our pervious results where the unique properties of N-SWCNHs not only provides void space to accommodate volume changes, but also prevents aggregation of Ge NCs during charge/discharge process. The crystallinity of as-prepared Sn@N-SWCNHs composite was characterized using X-ray diffraction analysis while the graphitic nature of N-SWCNHs was tested using Raman spectroscopy.

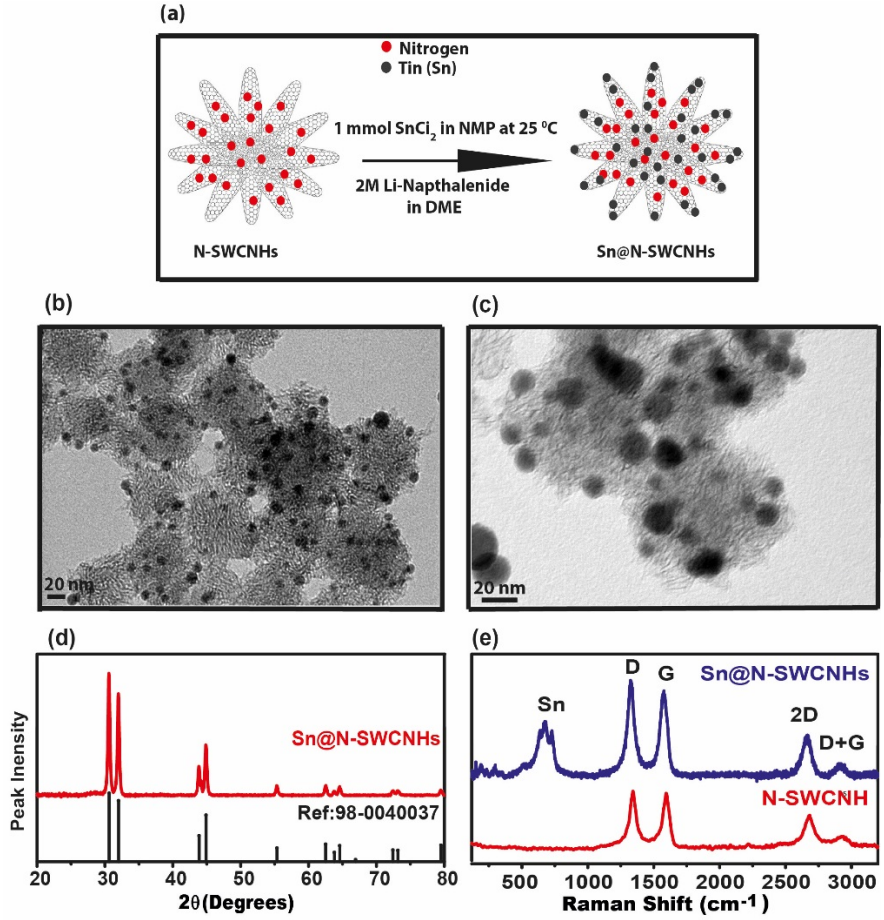

Figure 4.1: Schematics of the synthetic protocol of Ge@N-SWCNHs composite

In particular, XRD spectra of freshly prepared Sn@N-SWCNHs composite show characteristic peaks of cubic tetragonal beta tin at 2θ values of 30.58°, 31.98°, 43.86°, 44.86°, 55.34° 62.54°, 63.74°, 64.58°, 72.46°, 73.14° and 79.46° (Ref. 98-0040037). The average particle size of Sn NCs obtained using Scherrer equation was found to be 28 nm matching well with our TEM observations. Detailed characterization of N-SWCNHs and Sn@N-SWCNHs composite was performed using raman

spectroscopy. **Figure 4.1e** shows two prominent peaks associated to the D and G bands where the former is attributed to disordered sp^2 carbon while the latter is related to the vibrational modes of graphitic carbons[13]. Due to the topological defects of pentagons and heptagons in N-SWCNHs, these D and G peaks appears at 1348 and 1590 cm^{-1}, respectively[14]. Additional peaks at 2953 cm^{-1} (2D) and 3225 cm^{-1} (D+G) are the overtones of D and G peaks, respectively[15]. I_D/I_G ratios calculated for both spectra showed values close to unity, explaining the defected structure associated to N-SWCNHs[14]. Finally, multiple peak of Sn appear in the range 300 and 800 cm^{-1} demonstrating its intimate contact with N-SWCNHs.

4.3.2 Electrochemical Performance of Sn@N-SWCNHs

The electrochemical behavior of bare Sn NCs and Sn@N-SWCNHs composite electrodes were investigated in coin cells configuration using lithium metal as a reference electrode. FEC is known to facilitate the formation of mechanically stable solid electrolyte interface (SEI) which acts as a passivating layer to inhibit further electrolyte reduction[16] Therefore, 10% (v/v) fluoroethylene carbonate (FEC) was added to traditional electrolyte of 1M $LiPF_6$ in EC:DMC. **Figure 4.2a** show cyclic voltammograms of Sn@N-SWCNHs at a scan rate of 0.1mV/s using FEC as an electrolyte additive. Multiple reduction peaks in the range of 0.5-0.2V can be assigned to the lithiation reaction between tin and lithium to form the Li_xSn alloy while corresponding oxidation peaks between 0.4 V and 0.9 V can be associated to the de-lithiation reaction of the Li_xSn alloy.[17–19] An additional peak at 3.0V was only observed in the first oxidation scan **(not shown in figure 4.2a).** The cause of this mysterious peak, also observed by other researchers[6,20] is still under investigation.

The irreversible peaks in the range of 1.6-1.0V appeared due to the catalytic decomposition of FEC additive on the surface of the electrode. **Figure 4.2b** show the differential capacity plot of Sn@N-SWCNHs obtained from the charge discharge profile of a cell cycled at 0.1C. It is evident that after multiple cycles, the redox peak at 0.35V is shifted to lower potentials of 0.4V indicating the activation of Sn particles. Moreover, the lithiation of N-SWCNHs can be clearly seen at 0.015V. We believe that this irreversible lithiation is responsible for lower columbic efficiency during multiple cycling of Sn@N-SWCNHs based electrodes.

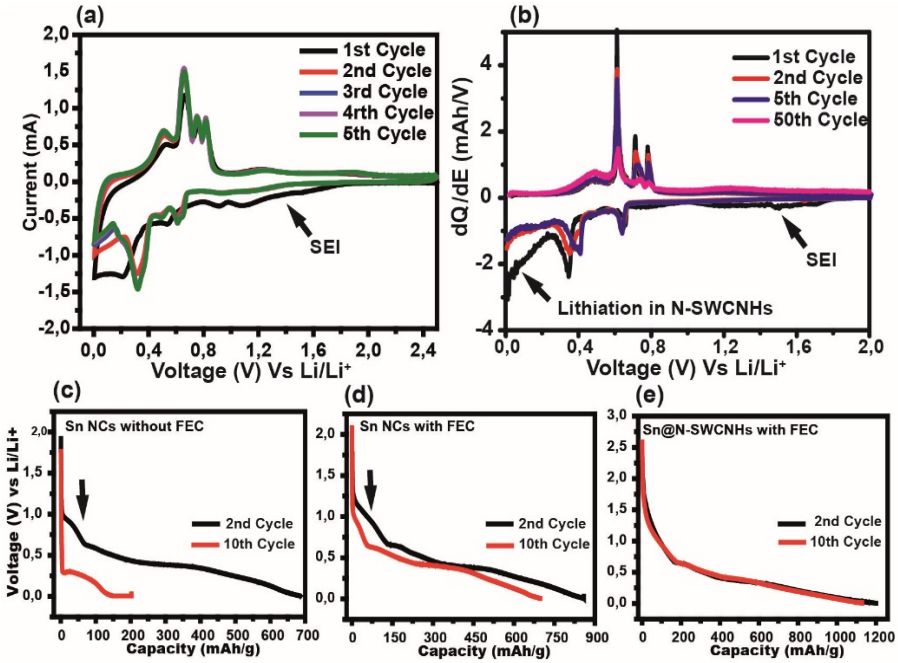

Figure 4.2: a) Cycling voltammogram of Sn@N-SWCNHs using 10% FEC as an electrolyte additive. b) Differential capacity plot of Sn@N-SWCNHs showing decrease in activation potential after multiple cycling. Comparison of 2nd and 10th discharge profile of c) Sn NCs without FEC d) Sn NCs with FEC and e) Sn@N-SWCNHs with FEC.

Comparison of Sn NCs and Sn@N-SWCNHs composite showed an increase overpotential for bare Sn NCs between 2nd and 10th cycles. **(Figure 4.2c and d**). However, minimal activation barrier between 2nd and 10th cycle was observed in the case of Sn@N-SWCNHs. **(Figure 4.2e)**. These results suggest the homogenous distribution of Sn NCs on the surface of N-SWCNHs limiting the aggregation process after multiple cycling.

The cycling performance of Sn NCs and Sn@N-SWCNHs composite was tested using chronopotentiometry. **Figure 4.2a** show the cycling performance of Sn NCs at 0.1 C (theoretical Capacity: 992 mAh/g) without using FEC as an electrolyte additive. It is quite evident that Sn NCs provided an initial discharge capacity of 1139 mAh/g which decayed rapidly to its lowest value of 73 mAh/g after 25 cycles. Similar electrochemical performance was observed for Sn NCs with FEC electrolyte additive where capacity decreased gradually to 225 mAh/g after 100 cycles. The decay in capacity observed in Sn NCs with and without FEC can be attributed to unstable SEI formation on the surface of Sn NCs and continuous aggregation of nanoparticles. Contrarily, Sn@N-SWCNHs showed stable cycling performance when cycled at 0.1C in the presence of FEC electrolyte additive. The initial discharge capacity of 2021 mAh/g was obtained in which half of the gravimetric capacity can be attributed to the decomposition electrolyte (EC, DMC) and additive (FEC). After the first cycle, the discharge capacity reached a value of 816 mAh/g and increased to the value of 925 mAh/g within 10 cycles. This capacity increasing behavior during charge/discharge cycles has also been reported on porous carbon[21], SnO_2/graphene nanocomposites[22] and Si/C nanocomposite anode materials[23] for lithium ion

batteries. The mechanism behind it is still not clear. After 140 cycles, the gravimetric capacity of Sn@N-SWCNHs stabilized at 795 mAh/g (**Figure 4.2c**). The remarkable storage capacities observed for Sn@N-SWCNHs using FEC as an electrolyte additive were comparatively higher to previously reported method where graphene and carbon nanotubes have been employed[9,22,24,25]. These results suggest an intimate contact between Sn nanocrystals and N-SWCNHs while allowing the high utilization of the active material.

The rate performance of Sn@N-SWCNHs composite was analyzed at different charge discharge rates where Sn@N-SWCNHs composite based electrodes show de-lithiation capacities of 960, 815, 735, 704 and 650 at 0.1C, 0.4C, 0.6C, 0.8C and 1C. respectively (**Figure 4.3d**). Superior performance of Sn@N-SWCNHs composite can realized by the fact that electrode material regained its original capacity of 921 mAh/g after been cycled at high scan rates. Finally, long term cycling was performed at 1C while limiting the potential range at different discharge voltages. When cells were cycled in the range of 2.5-0.1 V, they provided discharge capacity of 344 mAh/g at 1C. A shorter potential window between 2.5-0.05V gave higher capacities of 416 mAh/g. This increase in capacity can be associated to higher utilization of active material at same current densities.

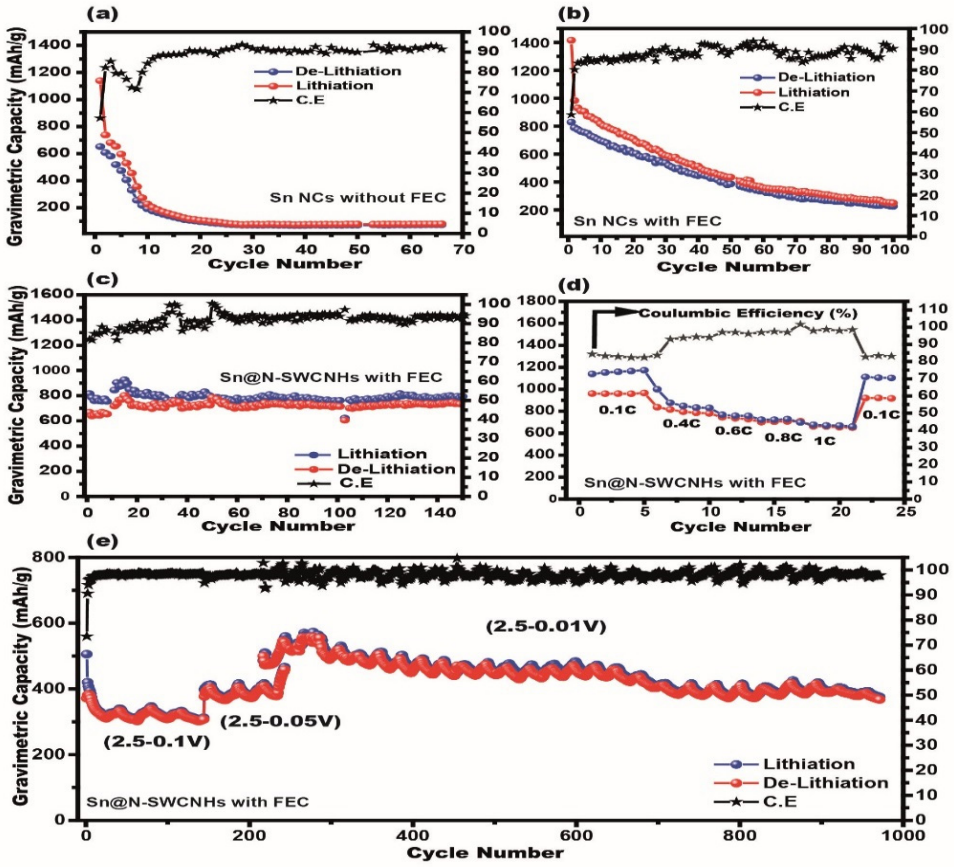

Figure 4.3. Cycling performance of Sn NCs a) without FEC b) with FEC c) Sn@N-SWCNHs composite with FEC. d) Rate performance of Sn@N-SWCNHs using 10% FEC. e) Long term cycling of Sn@N-SWCNHs composite at different lithiation voltages.

Finally, the discharge voltage was set in the range of 2.5-0.01V which provided even higher capacities of 570 mAh/g. This potential range was maintained for more than thousand cycles where gravimetric capacities were fluctuating after regular intervals. The reason for this fluctuating behavior is demands further investigation.

4.4 Conclusion

We report a facile synthetic route for the production of Sn nanocrystals on the surface of nitrogen doped single wall carbon nanohorns using Li-Naphthalenide as a reducing agent. As-prepared Sn@N-SWCNHs composite was used an anode material for lithium ion batteries. The electrochemical performance of bare Sn NCs were compared with Sn@N-SWCNHs composite. Half cells composed of Sn@N-SWCNHs cathode tested against lithium reference electrode provided high gravimetric capacities of 795 mAh/g at 0.1 after 140 cycles. Moreover, cells provided high rate performance and retained a gravimetric capacity of 375 mAh/g even after 1000 cycles at 1C.

4.5 References

[1] A. R. Kamali, D. J. Fray, *Rev. Adv. Mater. Sci.* **2011**, *27*, 14.

[2] I. A. Courtney, *J. Electrochem. Soc.* **1997**, *144*, 2045.

[3] G. Derrien, J. Hassoun, S. Panero, B. Scrosati, *Adv. Mater.* **2007**, *19*, 2336.

[4] J. Hassoun, K.-S. Lee, Y.-K. Sun, B. Scrosati, *J. Am. Chem. Soc* **2011**, *133*, 3139.

[5] Y. Xu, Q. Liu, Y. Zhu, Y. Liu, A. Langrock, M. R. Zachariah, C. Wang, *Nano Lett.* **2013**, *13*, 470.

[6] Y. Xu, J. Guo, C. Wang, *J. Mater. Chem.* **2012**, *22*, 9562.

[7] S.-D. Seo, G.-H. Lee, A.-H. Lim, K.-M. Min, J.-C. Kim, H.-W. Shim, K.-S. Park, D.-W. Kim, *RSC Adv.* **2012**, *2*, 3315.

[8] B. Luo, B. Wang, M. Liang, J. Ning, X. Li, L. Zhi, *Adv. Mater.* **2012**, *24*, 1405.

[9] B. Luo, B. Wang, X. Li, Y. Jia, M. Liang, L. Zhi, *Adv. Mater.* **2012**, *24*, 3538.

[10] Y. Yu, C.-H. Chen, Y. Shi, *Adv. Mater.* **2007**, *19*, 993.

[11] B. Wang, B. Luo, X. Li, L. Zhi, *Mater. Today* **2012**, *15*, 544.

[12] N. G. Connelly, W. E. Geiger, *Chem. Rev.* **1996**, *96*, 877.

[13] C. M. Yang, H. Noguchi, K. Murata, M. Yudasaka, A. Hashimoto, S. Iijima, K. Kaneko, *Adv. Mater.* **2005**, *17*, 866.

[14] T. Fujimori, K. Urita, Y. Aoki, H. Kanoh, T. Ohba, M. Yudasaka, S. Iijima, K. Kaneko, T. Agency, *Sci. Technol.* **1900**, 5.

[15] A. C. Ferrari, D. M. Basko, *Nat. Publ. Gr.* **2013**, *8*, 235.

[16] S. S. Zhang, *J. Power Sources* **2006**, *162*, 1379.

[17] L. Y. Beaulieu, S. D. Beattie, T. D. Hatchard, J. R. Dahn, *J. Electrochem. Soc.* **2003**, *150*, A419.

[18] Y. S. Jung, K. T. Lee, J. H. Ryu, D. Im, S. M. Oh, *J. Electrochem. Soc.* **2005**, *152*, A1452.

[19] W.-M. Zhang, J.-S. Hu, Y.-G. Guo, S.-F. Zheng, L.-S. Zhong, W.-G. Song, L.-J. Wan, *Adv. Mater.* **2008**, *20*, 1160.

[20] B. Guo, J. Shu, K. Tang, Y. Bai, Z. Wang, L. Chen, *J. Power Sources* **2008**, *177*, 205.

[21] S. Yang, X. Feng, L. Zhi, Q. Cao, J. Maier, K. Müllen, *Adv. Mater.* **2010**, *22*, 838.

[22] P. Lian, X. Zhu, S. Liang, Z. Li, W. Yang, H. Wang, *Electrochim. Acta* **2011**, *56*, 4532.

[23] A. Magasinski, P. Dixon, B. Hertzberg, A. Kvit, J. Ayala, G. Yushin, *Nat. Mater.* **2010**, *9*, 353.

[24] X. Zhou, J. Bao, Z. Dai, Y. G. Guo, *J. Phys. Chem. C* **2013**, *117*, 25367.

[25] Y. Zhong, X. Li, Y. Zhang, R. Li, M. Cai, X. Sun, *Appl. Surf. Sci.* **2015**, *332*, 192.

[26] S. Goriparti, U. Gulzar, E. Miele, F. Palazon, A. Scarpellini, S. Marras, S. Monaco, R. Proietti Zaccaria, C. Capiglia, *J. Mater. Chem. A* **2017**, *5*, 1.

Sodium Ion Batteries: For Times When Lithium Becomes the New Gold

Piles of Lithium Salts near the Lithium extraction facility in Bolivia. Credits:

5 INSIGHT ON SODIATION/DE-SODIATION MODE OF DAMAGE OF SN FILMS. AN ELECTROCHEMICAL AND MORPHOLOGICAL STUDY

Abstract

The development of anode materials for sodium-ion batteries is mainly hindered by the limited understanding of sodiation/de-sodiation mechanisms inside the active material, which typically results in electrode damage. Herein, we report a post-mortem ex-situ scanning electron microscopic analysis of Sn thin film motivated by the intention to elucidate these mechanisms. Our results reveal that during the sodiation process, the surface of Sn electrode film becomes highly porous with no presence of obvious crack, a surprising result when compared to previous reports performed on Sn particles. Even more surprisingly, our observations demonstrate that once the de-sodiation starts and reaches the second de-sodiation plateau (0.28V), obvious cracks in the Sn film are instead observed along with porous islands of active material. These islands result from the aggregation of smaller particles, and they further split into smaller islands when the de-sodiation potential reaches its maximum value (2.0V). Finally, impedance analysis is performed to correlate the electrochemical and morphological results..

5.1 Introduction

Sodium-ion batteries (SIBs) are being considered a viable replacement to existing lithium-ion batteries (LIBs) for stationary applications.[1] In search of electrode materials for SIBs, hard carbon has shown a reasonable capacity of ~300 mAh g^{-1} and being considered the "First Generation" anode for sodium ion systems.[2] However, due to the limited capacity of hard carbon, alloying material, preferentially tin (Sn) have been proposed as a high capacity alternative (847 mAh g^{-1} at $Na_{15}Sn_4$).[3] However, Sn based electrodes suffer from large volumetric expansion (~420%) which leads to severe mechanical stress causing electrode degradation.[4] Moreover, an important challenge to overcome in SIBs is the sluggish reaction kinetics due to the large ionic radius of Na ion (102 pm) which impedes fast sodium transport.[5]

Great endeavours have been devoted to solve these issues by preparing various nanostructured Sn[6,7] or Sn/carbon nanocomposites[8–17] and promising performances have been achieved. Meanwhile, extensive experimental and theoretical studies has also been conducted to better understand the sodium storage mechanisms in Sn anodes so as to establish their electrochemical performance as well as their viability as anodes in SIBs.[18–23] Furthermore, it is important to understand the nature of damage in Sn based electrode during the process of sodiation/de-sodiation.

Recent efforts in this direction were done by Huang et al.[24] who investigated the structural evolution and phase transformation of Sn nanoparticles using in-situ transmission electron microscopy (TEM). Negligible fractures were observed during

multiple sodiation/de-sodiation of Sn particles below ~200 nm. Similar sodiation/de-sodiation experiments performed using in-situ synchrotron hard X-ray nanotomography could not detect cracks in Sn particles with dimensions below 500 nm.[25] By comparing sodium insertion with its lithium counterpart, authors concluded that sodiation process results in large volume expansion and fracture of nanoparticles, whereas de-sodiation only induces the volume shrinkage with negligible pulverization and maintains microstructural integrity. All these observations are in striking contrast with the electrochemical behaviour of Sn when cycled against lithium, where de-lithiation causes severe structural damage. Moreover, phase diagrams for Li-Sn and Na-Sn reveal that the melting points of Na-Sn compounds are substantially lower than the Li-Sn analogues,[26] therefore, plasticity mechanisms might be more active in the Na-Sn electrodes. A different approach was applied by Datta et al.[27] where an ex-situ morphological study was performed on Sn/C composite electrodes (Crystal size: ~90 nm) after 20 cycles. Unfortunately, the results were not conclusive and the lack of clear evidence was associated to the cell environments where results are compromised by the introduction of multiple particle sizes distributions, binding materials and conductive matrix covering the active particles.

A morphological and electrochemical characterization of carbon and binder free Sn electrode, on a macroscopic level, is important to understand the actual mode of damage in Sn based electrodes. The information could indeed be helpful for designing carbon and binder free Sn electrodes as already occurred for lithium-ion batteries.[28,29] Moreover, the planar geometry associated to the macroscopic level

electrode, will experience a relatively simple state of stress produced by the one-dimensional gradient in lithium concentration therefore the current density used in the cycling can be easily interpreted. In the present work, a detailed morphological characterization of Sn thin film electrodes before and after sodiation is presented in order to understand the mode and evolution of damage using ex-situ scanning electron microscopy (SEM). Morphological results are then compared with electrochemical characterization techniques including impedance spectroscopy.

5.2 Experimental

5.2.1 Materials Preparation

Sn thin film of around 1 μm in thickness was deposited on a large piece of Cu foil substrate by PVD method using Sn foil (purity of 99.998%, purchased from Sigma Aldrich Co, LLC) as the tin source. Small disks of 15 mm in diameter were cut from the as-prepared large piece of Sn thin film and stored in a MBraun glove box under Ar atmosphere with a water and oxygen content less than 0.1 ppm before making a coin-type cell.

5.2.2 Electrochemical Cycling

The electrochemical performance of the as-prepared Sn thin film electrode was evaluated using R2032-type coin cells. The Cu foil substrate served as the current collector to obtain a uniform current distribution. The assembly of the sodium half-cell was conducted in the Ar-filled glove box with sodium metal employed as the

counter and reference electrode, Whatman fiber glass as separator, and 1.0 M of $NaClO_4$ in propylene carbonate (PC) as electrolyte. Galvanostatic cycling of the cells at the low current of 20 μA (C/40 in rate) was carried out within a voltage range of 0.005–2.0 V (vs. Na+/Na) using Biologic BCS-805 multichannel battery test system at room temperature..

5.2.3 Characterization

Powder X-ray diffraction (XRD) was carried out utilizing a Rigaku Smart Lab 9 kW diffractometer equipped with Cu Kα X-ray source operated at 40 kV and 150 mA. Scanning electron microscopy (SEM) images were obtained using a JEOL JEM 6490LA (Jeol, Tokyo, Japan) equipped with a cold FEG, operating at 15 kV acceleration voltage. Both the XRD and SEM of the tin film electrode before and after cycling were conducted. In order to perform the XRD and SEM of the tin film electrode after cycling, the coin-type cells after discharging or charging were disassembled and the Sn film electrodes were washed with PC and then dried at 70 °C for 3 h. The resulting dried tin film electrodes after cycling was further cut into small pieces and kept in a vial before performing the XRD and SEM. All the above operations were carried out in the Ar-filled glove box.

5.3 Result and discussion

5.3.1 Electrode fabrication and characterization

Sn thin films were prepared by physical vapour deposition (PVD) method on a battery grade copper foil substrate and cut into circular disks with surface area of 1.76 cm^2.

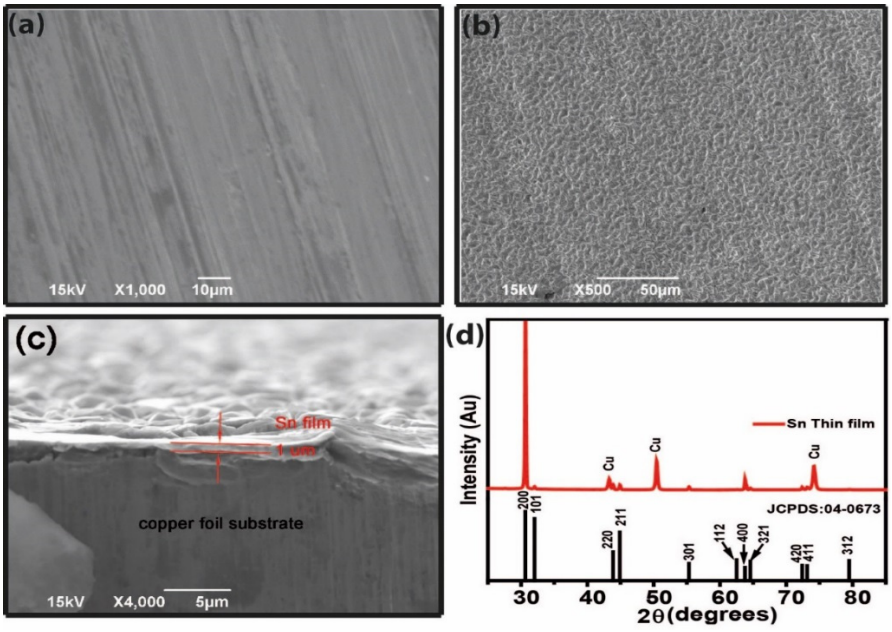

Figure 5.1: SEM images of the surface morphology of a) copper substrate b) Sn film on the surface of substrate and (c) the cross section of the as-prepared Sn thin film by PVD method on Cu foil substrate. The thickness of Sn film is around 1 um, as shown in (c). (d) XRD pattern of the Sn thin film electrode before cycling.

Surface morphologies of the copper (Cu) substrate and as-prepared Sn thin film are shown in **Figure 5.1a, b,** respectively. In particular, **Figure 5.1b** shows a dense and sinusoidal surface composed of coarse particles with diameter in the range 3–4 μm

while **Figure 5.1c** shows a cross-sectional image of Sn thin film (1 μm thickness) deposited on top of 25 μm thick copper substrate It is well-known that the crystal structure and the crystallographic orientation of the deposited material depends on experimental conditions and the crystal orientation of the substrate.[30] Therefore, X-ray diffraction (XRD) analysis was performed to understand the crystallographic structure of the as-prepared Sn film. The XRD patterns displayed in **Figure 5.1d** reveal that the main diffraction peaks match well with the reference Sn phase (JCPDS No. 04-0673). As expected, Sn film shows a preferred crystalline orientation along [200] direction while peaks corresponding to the other planes have limited amplitudes, which can be associated to the growth mechanism under our experimental conditions. Moreover, no peaks of SnO_2 or SnO were identified during the XRD analysis.

5.3.2 Electrochemical Characterization

Electrochemical characterization was performed by cycling as-prepared electrodes against freshly cut sodium reference electrode in a coin cell configuration. The employed electrolyte was formed by 200 μL of 1.0 M $NaClO_4$ in propylene carbonate (PC) with a mass loading for 1 μm thin layer of tin equal to 0.9 mg/cm^2. In particular, galvanostatic cycling at 20 μA (C/40 in rate) in the voltage range of 0.005–2.0 V (vs. Na/Na^+) was carried out to investigate the sodiation/de-sodiation process. The sodiation of Sn is known to occur in four distinct steps corresponding to the characteristic bi-phasic reactions.[12,19,20,30] The differential capacity plot of the Sn thin film electrode obtained from galvanostatic charge/discharge profile shown in **Figure 5.2a** clearly confirms the four distinct sodiation peaks at 0.36, 0.19, 0.08 and 0.035 V

along with the de-sodiation peaks at 0.14, 0.25, 0.53 and 0.58 V. However, a close inspection shows an additional broad sodiation peak at 0.41 V (**Figure 5.3a**) which can be associated to the conversion of SnO_2 layer to Sn.[20]

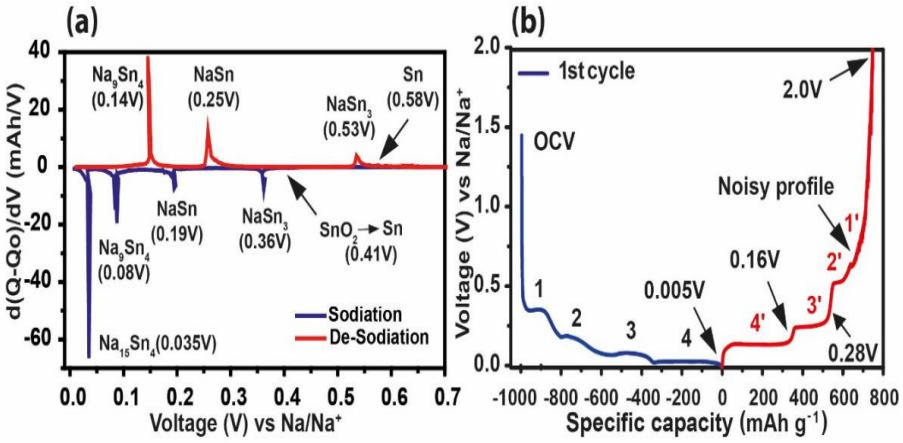

Figure 5.2: a) Differential Capacity plot obtained from galvanostatic charge discharge profile showing distinct peaks of various phases formed during sodiation and de-sodiation. b) Galvanostatic charge discharge profile of as-prepared Sn film (mass loading: 0.9 mg/cm^2) cycled at 20 μA. Red dots show the electrochemical potentials at which SEM images were taken

The voltage plateaus in the first discharge/charge profile (**Figure 5.2b**) are in general agreement with the density functional theory (DFT) calculations by Chevrier et al.[18]

However, due to the high polarization, the discharge/charge potentials of each experimental plateaus are considerably shifted compared to DFT calculated voltages. Similar results were reported in the study of sodiation/de-sodiation mechanism of Sn film electrodes prepared by electrodeposition and magnetron sputtering.[19,20,30] Interestingly, potential dips before each bi-phasic reaction were observed during the sodiation process along with a noisy voltage profile at the end of the de-sodiation

process (**Figure 5.2b** and **5.3b**), which might be related to various complex phenomena including pore formation, continuous electrolyte decomposition and improved diffusion in amorphous $NaSn_x$ phases. All these detrimental effects might indeed be the cause of the rapid capacity decay observed in the second cycle, therefore suggesting the pulverization of Sn electrodes (**Figure 5.3c**).

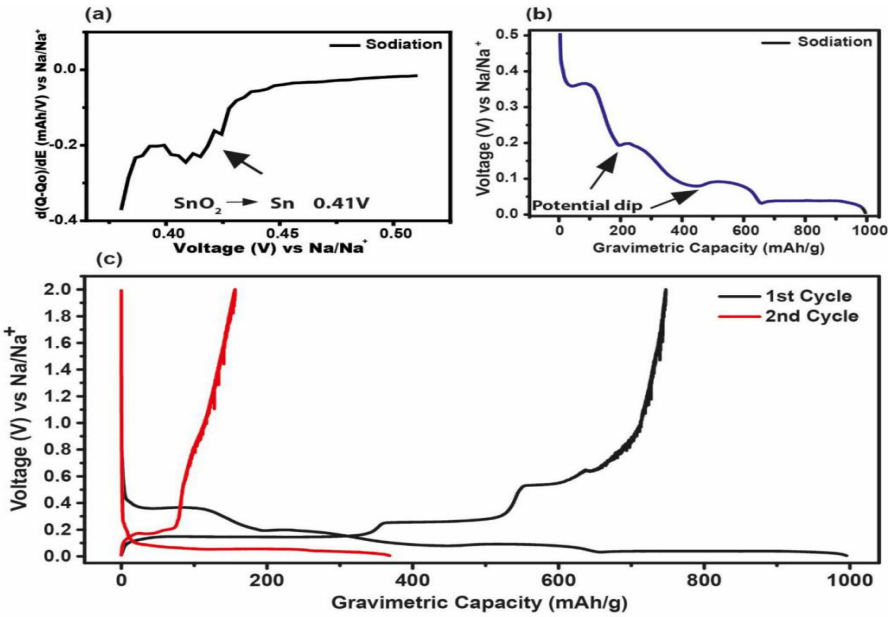

Figure 5.3: a) differential capacity plot of Sn electrode in the range of 0.9-0.50V showing an additional peak at 0.41V. b) Charge-discharge profile of Sn electrodes showing obvious potential dips before the start of each bi-phasic reactions. c) First and second cycles of charge discharge profile.

5.4 Morphological Characterization

To understand the degradation mechanism of Sn electrode, ex-situ scanning electron microscopy was performed at different stages of first sodiation and de-sodiation

process. **Figure 5.4** show SEM images of Sn electrode before and after complete sodiation (0.005V). It is quite evident that the uneven surface of Sn film (**Figure 5.4a**) consists of 3–4 μm particles separated by valleys containing smaller particles of ~1 μm. Once the electrode is completely sodiated up to 0.005 V, its surface becomes highly porous and inflated, suggesting severe volumetric expansion, due to the formation of $Na_{15}Sn_4$ (**Figure 5.4b**). Differently from the previous report by Wang et al.[25] no obvious cracks along the lateral surface of electrode were observed. However, after close inspection of the porous electrode, small cracks within the pores were identified which may be associated to inhomogeneous expansion of Sn electrode during sodiation (**Figure 5.4c**).

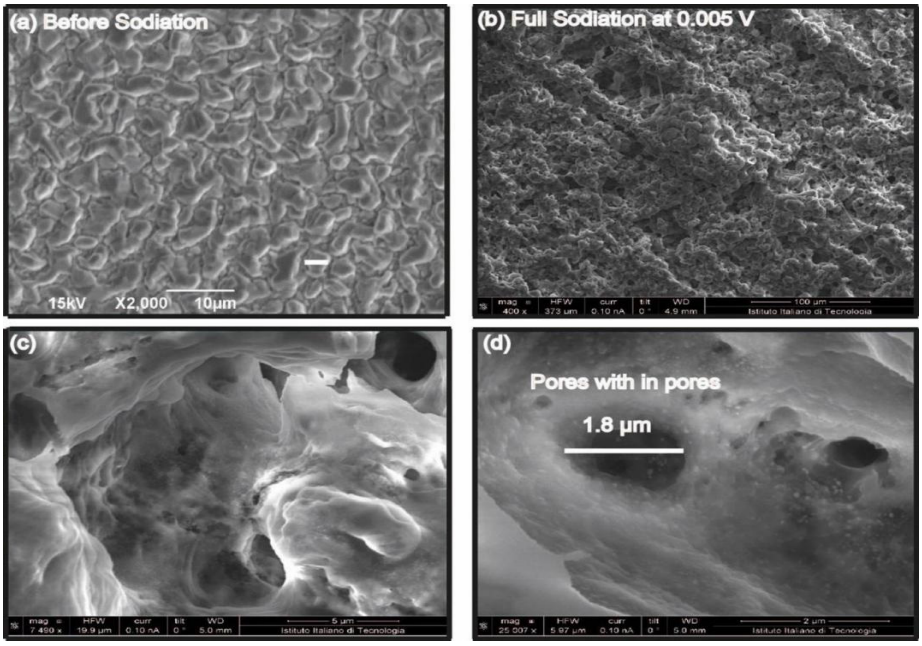

Figure 5.4: Scanning electron microscopy images of Sn thin film a) before cycling b) after full sodiation at 0.005V. c and d) are the magnified images of (b) showing the porous structure of Sn film with nanoparticles on the surface.

This inhomogeneous expansion would be caused by the different crystallite size on Sn films providing different diffusion pathways. Large number of nanometer size particles were also observed on the interior surface of the pores along with additional small pores. The size of the small pores were in the range of 0.2–1.8 μm (**Figure 5.4d**) while the nature and cause of small particles is still unknown. These results suggest that the process of sodiation causes severe expansion of the electrode making it porous without however breaking or cracking the surface of the electrode. It is interesting to note that the Sn film electrode undergoes volume expansion accompanied with large amounts of pores formation at the sodium insertion (sodiation) process, which is quite different from those reported pore formation in Sn particles[25,31] and Si nanowires[32,33] at the lithium extraction (de-lithiation) step. Chao et al. attributed the formation of porous Sn particles observed during the first de-lithiation to the re-crystallization process of Sn.[31] The observation of pore formation in Si nanowires during de-lithiation can be interpreted as a result of the fast lithiation/de-lithiation kinetics.[33] However, the cause of the surprising observation of pore formation with no presence of obvious crack in Sn film at the sodiation process in the present study is not known and needs further investigation.

These results suggest that the destruction of Sn electrode during sodiation process is not evident and, therefore, must be happening during the process of de-sodiation. To verify this hypothesis, we obtained the SEM images of electrodes at different

stages of de-sodiation. In particular, the SEM images obtained after the first de-sodiation step at 0.16 V showed some structural deformation, however, no obvious lateral cracks were observed (**Figure 5.5a** and **b**). During de-sodiation, $Na_{15}Sn_4$ with a volumetric expansion of 420% is expected to convert into Na_9Sn_4 with a volumetric expansion of 252%.[24] SEM analysis performed after de-sodiation of electrodes up to 0.16V show no considerable evidence of cracking and suggests that volumetric contraction of 168% is not enough to produce cracks under these experimental conditions. However, further de-sodiation of the electrode up to 0.28 V showed severe cracks along the lateral size of the electrode resulting in ~50 μm islands of active material (**Figure 5.5c**). Interestingly, each island seems to be an aggregation of ~5 μm particles one another anchored (**Figure 5.5d**). Upon complete de-sodiation process up to 2 V, the size of the islands become smaller (~5 μm) while the active material starts to peel off from the substrate surface (**Figure 5.5e** and **f**). We suggest that these smaller islands might be the same particles shown in **Figure 5.5d** which are just de-aggregated upon further de-sodiation making islands of the similar size. Furthermore, these smaller islands are porous and contain small particles anchored to their surface.

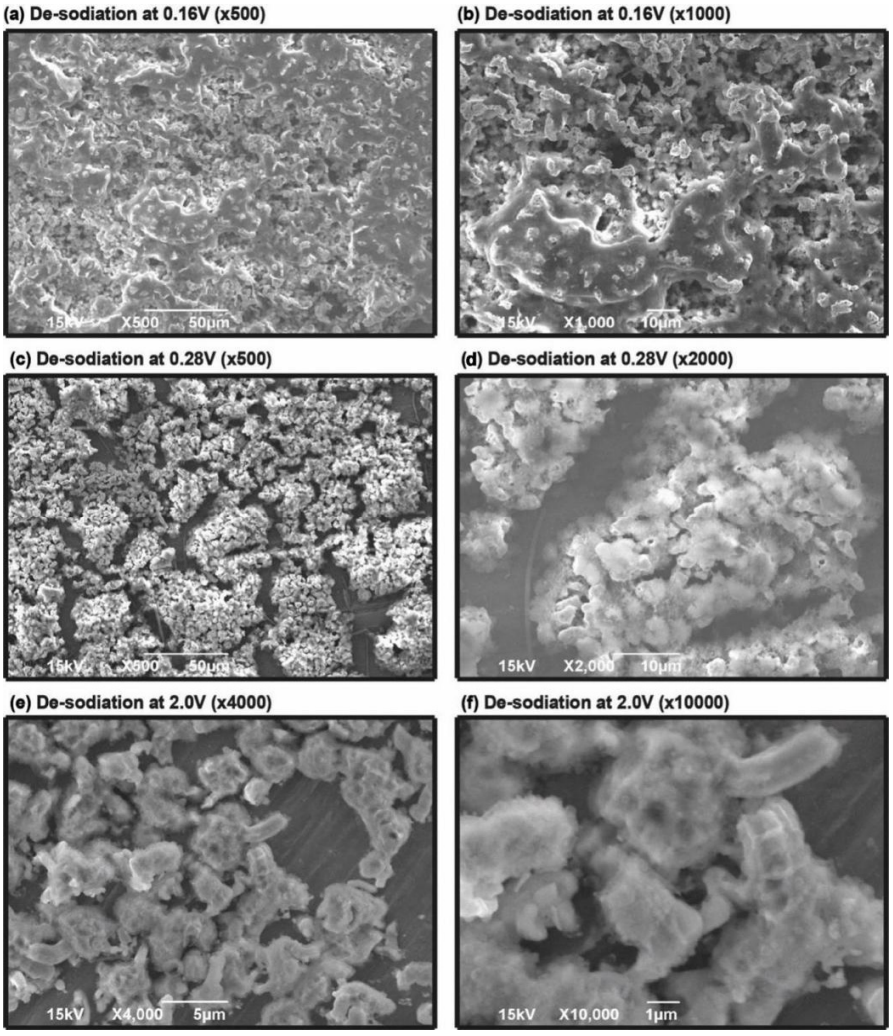

Figure 5.5: Scanning electron microscopy images of Sn thin film a) before cycling b) after full sodiation at 0.005V. c and d) are the magnified images of (b) showing the porous structure of Sn film with nanoparticles on the surface.

A further indication of the severe electrode destruction and islands formation is provided by the noisy voltage profile at the end of de-sodiation process shown in **Figure 5.6a**, also accompanied by a rapid decay in the capacity after the first cycle.

This fast decay is due to the loss of electrical contact between active material and current collector, with the particles maintaining the same size after multiple cycling (**Figure 5.6b**).

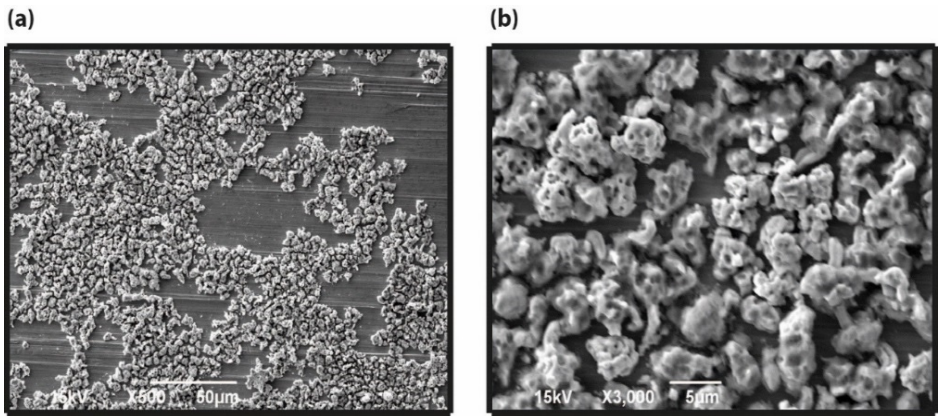

Figure 5.6: SEM images of Sn electrode after two cycles of sodiation/de-sodiation showing no difference in the particles size.

5.5 Electrochemical Impedance Spectroscopy

To correlate the structural evolution of Sn electrode with electrochemical electrode failure, impedance spectroscopy was performed at the same potentials where SEM analysis was carried out. The Faradaic impedance of an electrode material can be separated into kinetic (Z_k) and diffusive impedance (Z_d). Due to the conductive nature of Sn, kinetic impedance (Z_k) can be represented by the charge transfer resistance, whereas diffusive impedance (Z_d) describes the contribution from the concentration overpotential, hence it depends on the transport phenomena of the sodium ions.[34] Moreover, Nyquist diagram of the Faradaic impedance consists of two distinct domains with semicircles in the high and low frequency regions and a

straight line in the low frequency region. As expected, the Nyquist plot of the Sn electrodes obtained at OCV (before sodiation) shows a high frequency (HF) small arc followed by a large arc in the low frequency (LF) region. The HF arc (**Figure 5.7a**, inset) can be associated to the charge transfer resistance while the second arc at LF can be associated to the blocking character of non-sodiated electrode along with phase transformations at very low frequency regions (**Figure 5.7a**). Usually, the arc at LF is absent in traditional intercalation materials such as $LiCoO_2$ or graphite due to small energetic differences between two different phases.

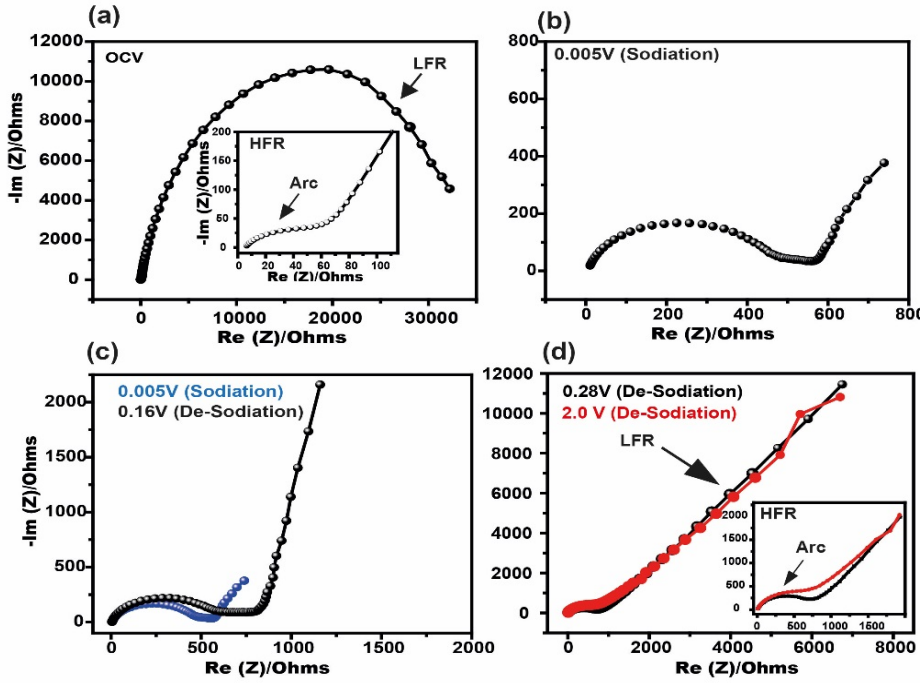

Figure 5.7: Impedance spectra (Nyquist plots) obtained a different stage of sodiation a) at OCV b) fully sodiated at 0.005V and de-sodiation c) at 0.16V d) 0.28 and 2.0V.

However, large variations in physical and chemical properties of Sn and $NaSn_x$ phases cause two different time constants for sodium ion transference allowing a new arc to appear at LF region.[35] Furthermore, the Nyquist plot obtained at full sodiated state (0.005V) shows a depressed semicircle and a reduced straight line (**Figure 5.7b**). It is quite interesting that the LF arc observed at OCV transforms into one straight line as the electrode potential reaches 0.005 V. This observation suggests that the high diffusive resistance associated to solid Sn is reduced significantly due to the porous structure of electrode making the straight line to appear at lower values of resistance. Moreover, the high surface area enhances the migration predisposition of the active material, resulting in a minimized polarization.

Benefiting from the impedance data obtained at the LF region, the diffusion coefficient of sodium inside the electrode was calculated at 0.005 V using a model proposed by Ho et al.,[36] according to the following equation:

$$D_{Na} = \frac{1}{2}\left[\left(\frac{V_m}{zFA\partial}\right)\left(\frac{dE}{dx}\right)\right]^2$$

where V_m is the molar volume of Sn (16.340 cm^3/mol), z is the charge of sodium ions, F is the Faraday constant (96,485 C mol^{-1}), A is the surface area of the Sn electrode (1.76 cm^2) , ∂ is the slope of the plot obtained from the imaginary part of impedance (Z_{im}) *vs* inverse square root of the angular frequency ($\omega^{-1/2}$) and dE/dx is the slope obtained from galvanostatic charge/discharge capacity plot. The approximate diffusion coefficient for sodium ions inside our porous Sn electrode at 0.005V was found to be 3.9×10^{-14} cm^2 s^{-1}. This diffusion coefficient of Na ions in Sn is tempted to be the first experimental value obtained, which is much lower than the theoretical

values that have been already reported in the literature[37,38] and also lower than the experimental values for Li ion diffusion in Sn[39,40] due to the larger radius of Na ion than Li ion.

The Nyquist plot obtained during the de-sodiation process (0.16 V) clearly shows a wider depressed semi-circle than EIS at 0.005 V sodiation, suggesting the existence of multiple phases of $Na_{15}Sn_4$ and Na_9Sn_4 with higher charge transfer resistance (**Figure 5.7c**). It also indicates the possible presence of structural damage, such as cracks, which lead to the non-ideal behaviour of the electrode surface. Once the electrode potential reaches 0.28 V (**Figure 5.7d**), a small arc at HF region reappears followed by an enhanced straight line. The enhancement of the straight line indicates the blocking characteristic of de-sodiated Sn phases which appears after the turning of the film Sn electrode into small islands, therefore determining a direct contact between the copper substrate and sodium ions. Similar results are described also by the Nyquist plot at 2.0 V when the Sn film starts to peel off.

5.6 Conclusions

We have explored the mode of damage mechanism of binder and carbon free thin film Sn electrode during sodiation/de-sodiation process. Ex-situ SEM was used to study the morphological features of the Sn electrode at different stages of sodiation and de-sodiation. Our results show considerable swelling of Sn film electrode at the end of the sodiation process, however no cracks were observed on the Sn films, a novel result with respect to previous reports.[25] Cracks start instead appearing during the de-sodiation process at potential of 0.28 V where the Sn electrode forms islands

of active material. Upon further de-sodiation these aggregated islands crumbled to form even small islands. Finally, all these observations were correlated with impedance spectroscopy which was also used to calculate the diffusion coefficient of Na inside Sn electrode.

5.7 References

(1) Larcher, D.; Tarascon, J.-M. Nat. Chem. 2014, 7 (1), 19–29.

(2) Komaba, S.; Murata, W.; Ishikawa, T.; Yabuuchi, N.; Ozeki, T.; Nakayama, T.; Ogata, A.; Gotoh, K.; Fujiwara, K. Adv. Funct. Mater. 2011, 21 (20), 3859–3867.

(3) Tran, T.T.; Obrovac, M.N. J. Electrochem. Soc. 2011, 158 (12), A1411–A1416.

(4) Li, Z.; Ding, J.; Mitlin, D. Acc. Chem. Res. 2015, 48 (6), 1657–1665.

(5) Ong, S.P.; Chevrier, V.L.; Hautier, G.; Jain, A.; Moore, C.; Kim, S.; Ma, X.; Ceder, G. Energy Environ. Sci. 2011, 4 (9), 3680–3688.

(6) Nam, D.-H.; Kim, T.-H.; Hong, K.-S.; Kwon, H.-S. ACS Nano 2014, 8 (11), 11824–11835.

(7) Cheng, Y.; Huang, J.; Li, R.; Xu, Z.; Cao, L.; Ouyang, H.; Li, J.; Qi, H.; Wang, C. Electrochim. Acta 2015, 180, 227–233.

(8) Li, S.; Wang, Z.; Liu, J.; Yang, L.; Guo, Y.; Cheng, L.; Lei, M.; Wang, W. ACS Appl. Mater. Interfaces 2016, 8 (30), 19438–19445.

(9) Luo, L.; Qiao, H.; Xu, W.; Li, D.; Zhu, J.; Chen, C.; Lu, Y.; Zhu, P.; Zhang, X.; Wei, Q. J. Solid State Electr. 2017, 21 (5), 1385–1395.

(10) Ying, H.; Zhang, S.; Meng, Z.; Sun, Z.; Han, W.Q. J. Mater. Chem. A 2017, 5 (18), 8334–8342.

(11) Liu, Y.; Xu, Y.; Zhu, Y.; Culver, J.N.; Lundgren, C.A.; Xu, K.; Wang, C. ACS Nano 2013, 7 (4), 3627–3634.

(12) Datta, M.K.; Epur, R.; Saha, P.; Kadakia, K.; Park, S.K.; Kumta, P.N. J. Power Sources 2013, 225, 316–322.

(13) Luo, B.; Qiu, T.; Ye, D.; Wang, L.; Zhi, L. Nano Energy 2016, 22, 232–240.

(14) Liu, Y.; Zhang, N.; Jiao, L.; Chen, J. Adv. Mater. 2015, 27 (42), 6702–6707.

(15) Liu, Y.; Zhang, N.; Jiao, L.; Tao, Z.; Chen, J. Adv. Funct. Mater. 2015, 25 (2), 214–220.

(16) Xu, Y.; Zhu, Y.; Liu, Y.; Wang, C. Adv. Energy Mater. 2013, 3 (1), 128–133.

(17) Zhu, H.; Jia, Z.; Chen, Y.; Weadock, N.; Wan, J.; Vaaland, O.; Han, X.; Li, T.; Hu, L. Nano Lett. 2013, 13 (7), 3093–3100.

(18) Chevrier, V. L.; Ceder, G. J. Electrochem. Soc. 2011, 158 (9), A1011–A1014.

(19) Ellis, L.D.; Hatchard, T.D.; Obrovac, M.N. J. Electrochem. Soc. 2012, 159 (11), A1801–A1805.

(20) Baggetto, L.; Ganesh, P.; Meisner, R.P.; Unocic, R.R.; Jumas, J.C.; Bridges, C.A.; Veith, G.M. J. Power Sources 2013, 234, 48–59.

(21) Mortazavi, M.; Deng, J.; Shenoy, V.B.; Medhekar, N.V. J. Power Sources 2013, 225, 207–214.

(22) Baggetto, L.; Bridges, C.A.; Jumas, J.C.; Mullins, D.R.; Carroll, K.J.; Meisner, R.A.; Crumlin, E.J.; Liu, X.; Yang, W.; Veith, G.M. J. Mater. Chem. A 2014, 2 (44), 18959–18973.

(23) Stratford, J.M.; Mayo, M.; Allan, P.K.; Pecher, O.; Borkiewicz, O.J.; Wiaderek, K.M.; Chapman, K.W.; Pickard, C.J.; Morris, A.J.; Grey, C.P. J. Am. Chem. Soc. 2017, 139, 7273–7286.

(24) Wang, J.W.; Liu, X.H.; Mao, S.X.; Huang, J.Y. Nano Lett. 2012, 12 (11), 5897–5902.

(25) Wang, J.; Eng, C.; Chen-Wiegart, Y.K.; Wang, J. Nat. Commun. 2015, 6, 7496–7505.

(26) Hiroaki, O.; Mark E, S.; Erik M, M. ASM Handbook Vol. 3: Alloy Phase diagrams; ASM International: Materials Park, OH, 1992.

(27) Datta, M.K.; Epur, R.; Saha, P.; Kadakia, K.; Park, S.K.; Kumta, P.N. J. Power Sources 2013, 225, 316–322.

(28) Kennedy, T.; Mullane, E.; Geaney, H.; Osiak, M.; O'Dwyer, C.; Ryan, K.M. Nano Lett. 2014, 14 (2), 716–723.

(29) Mullane, E.; Kennedy, T.; Geaney, H.; Ryan, K.M. ACS Appl. Mater. Interfaces 2014, 6 (21), 18800–18807.

(30) Nam, D.-H.; Hong, K.-S.; Lim, S.-J.; Kim, T.-H.; Kwon, H.-S. J. Phys. Chem. C 2014, 118 (35), 20086–20093.

(31) Chao, S.C.; Yen, Y.C.; Song, Y.F.; Chen, Y.M.; Wu, H.C.; Wu, N.L. Electrochem. Commun. 2010, 12 (2), 234–237.

(32) Choi, J.W.; McDonough, J.; Jeong, S.; Yoo, J.S.; Chan, C.K.; Cui, Y. Nano Lett. 2010, 10 (4), 1409–1413.

(33) Lu, X.; Bogart, T.D.; Gu, M.; Wang, C.; Korgel, B.A. J. Phys. Chem. C 2015, 119 (38), 21889–21895.

(34) Cesiulis, H.; Tsyntsaru, N.; Ramanavicius, A.; Ragoisha, G. Nanostructures and Thin Films for Multifunctional Applications; Tiginyanu, I., Topala, P., Ursaki, V., Eds.; NanoScience and Technology; Springer International Publishing: Cham, 2016.

(35) Fan, X.-Y.; Zhuang, Q.-C.; Wei, G.-Z.; Huang, L.; Dong, Q.-F.; Sun, S.-G. J. Appl. Electrochem. 2009, 39 (8), 1323–1330.

(36) Ho, C. J. Electrochem. Soc. 1980, 127 (2), 343–350.

(37) Chou, C.Y.; Lee, M.; Hwang, G.S. J. Phys. Chem. C 2015, 119 (27), 14843–14850.

(38) Jung, S.C.; Kim, H.J.; Kang, Y.J.; Han, Y.K. J. Alloy. Compd. 2016, 688, 158–163.

(39) Fok, E.C.W.; Madden, J.D. ECS Trans. 2013, 53 (30), 131–142.

(40) Zhang, T.; Fu, L.J.; Gao, J.; Wu, Y.P.; Holze, R.; Wu, H.Q. J. Power Sources 2007, 174 (2), 770–773.

6 Prospects of N-Doped Single Walled Carbon Nanohorns As Energy Storage Material

Single Walled Carbon nanohorns are unique and interesting carbon material which is somehow neglected in the course of last 20 years due to its limited scale of production. Nevertheless, they share a bright future with other carbon materials due to the fact that they can be mass- produced, now in industrial quantities by Advanced Technology Partner S.rl. Moreover, they offer a genuine and advantageous alternative to carbon nanotubes, and possibly graphene, in a wide range of applications. Below we are going to highlight some important factors which should be considered before the realization of SWCNHs as an energy storage material/additive.

Electrical conductivity is an important parameter in the field of energy storage. Unfortunately, SWCNHs suffer from low electrical conductivity compare to carbon nanotubes and graphene. In my opinion, the low conductivity of SWCNHs originate from countless individual contact resistances between each aggregate and between individual tubules consequently increasing the impedance of the cell and the loss of useful energy. One way of solving the problem is to induce a doping element (nitrogen in our case), however, the amount of doping element should be optimized for achieving better conductivities and electrochemical performances.

Porous conductive materials with high micro-pore volumes are suggested to be useful for limiting polysulfides dissolution in lithium sulfur batteries. Besides, they provide micro-cavities for storing active materials. The surface area of N-SWCNHs,

observed in our studies, is comparatively low (211 m^2/g with micro-pore volume of 0.025 cm^3/g) with respect to other carbon materials reported in the literature. Therefore, the surface area of N-SWCNHs should be improved with higher pore volumes before realizing its commercial application as a conductive host for lithium sulfur batteries. Moreover, the three different types of SWCNHs, namely, dahlia type, bud type and seed type have shown different electrochemical properties. Therefore, separating each type is important to understand the contribution of individual SWCNHs. However, the technology for separating different types of SWCNHs is not fully developed and require further research.

SWCNHs have shown disaggregation when treated with a strong reducing agent of potassium naphthalenide. I believe that similar reducing environment is present inside an electrochemical cell where lithium intercalate/penetrate to the aggregating structure of SWCNHs at potentials below 0.05V**(Figure 6.1)**. Once lithium penetrate inside the structure, it disaggregates the tubules creating extra void for the decomposition of electrolyte. I believe that this phenomena is responsible for continuous increase in capacity with low columbic efficiencies In this regard, in-situ transmission electron microscopy could be helpful in proving this hypothesis. Nevertheless, detailed understanding of the lithiation process inside SWCNHs is important to utilizing this cheap material of advance batteries.

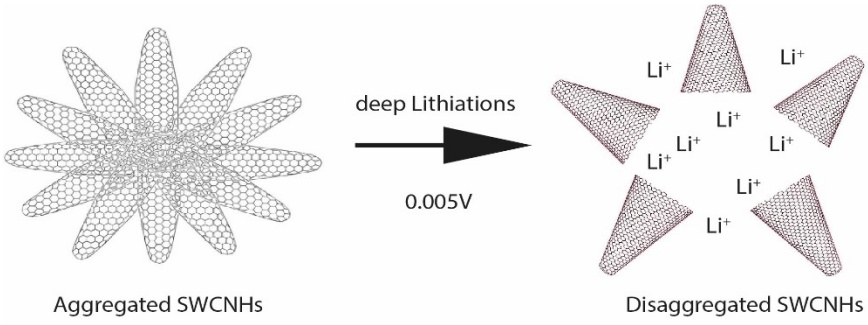

Figure 6.1: Disaggregation of SWCNHs after the process of lithiation exposing more surface area for electrolyte decomposition

Finally, understanding the unique specific conical morphology of nanohorns structure as well as their synthesis and topology is of fundamental importance for advancing their research and development. Manipulation and handling of nanohorns can be enhanced in wet media, and integration of active moieties toward nanohorns-based functional hybrid materials opens wide avenues for a plethora of practical applications.